# DEGRADATION OF POLYMERIC ADHESIVES IN ADVERSE ENVIRONMENTAL CONDITIONS

Ву

Yang Chen

#### A DISSERTATION

Submitted to
Michigan State University
in partial fulfillment of the requirements
for the degree of

Civil Engineering—Doctor of Philosophy

2025

#### **ABSTRACT**

Cross-linked elastomers, known for their exceptional flexibility, toughness, formability, and versatility, play a vital role in a wide array of engineering applications across aerospace, construction, transportation, marine, aeronautics, and automotive sectors. These materials are expected to maintain high performance throughout their service life, even when exposed to aggressive environmental conditions such as water infusion, temperature fluctuations, and ultraviolet (UV) radiation. These environmental factors pose significant challenges, as they can gradually deteriorate the material's properties and reduce its overall durability.

Among the most critical forms of environmental degradation are thermal aging under oxygen-deficient conditions and oxidative aging caused by elevated oxygen concentrations. The former typically results in uniform thermal degradation of the material, while the latter, known as diffusion-limited oxidation (DLO), induces spatially heterogeneous damage, primarily at the surfaces of the polymer where oxygen diffusion is more pronounced. Together, these two forms of aging represent fundamentally inverse degradation conditions—one being inert and volumetric, and the other being oxidative and surface-driven. Accurate prediction of the long-term behavior of elastomers under both these conditions is essential for designing reliable rubber components that resist early failure in service.

To address this need, high-fidelity constitutive models are essential for simulating the effects of aging on the mechanical, thermal, and failure characteristics of cross-linked polymers. Historically, most aging models have employed hyperelastic constitutive laws coupled with single-kinetic degradation equations to model the evolution of material properties over time. While these approaches have been useful in capturing basic degradation trends, they often fall short in representing the complex interactions between microstructural evolution and macroscale mechanical behavior under realistic service conditions.

This dissertation presents a comprehensive multi-physics modeling framework to capture the distinct and coupled degradation behaviors of cross-linked polymers under both diffusion-limited oxidation and inert thermal aging. These models incorporate the effects of oxygen diffusion, re-

action kinetics, and thermally activated chain scission and cross-linking processes to simulate the evolution of polymer microstructure over time. By resolving the spatial and temporal development of aging parameters, the framework successfully reproduces both uniform and spatially heterogeneous degradation phenomena, providing critical insight into how these opposing environmental factors influence long-term material performance.

The modeling approach is grounded in continuum mechanics and integrates finite strain theory with micro-mechanically motivated degradation mechanisms. Rubber elasticity is described across three scales: statistical mechanics at the microscale to account for molecular chain behavior, network-based phenomenological modeling at the mesoscale, and continuum theory at the macroscale. This multi-scale approach enables the representation of polymer network reconfiguration during aging, which is essential for predicting stiffness loss, permanent deformation, and eventual failure.

While the core of this dissertation focuses on physics-based modeling of aging mechanisms, recent advancements in machine learning (ML), particularly physics-informed neural networks (PINNs), offer promising opportunities to enhance traditional modeling techniques. Although early generations of data-driven black-box models were limited by their need for large datasets and lack of physical constraints, hybrid approaches—where experimental macroscopic data are used to infer underlying microstructural behavior within physics-informed frameworks—have begun to bridge this gap. In this work, such techniques are explored in a supporting capacity to augment the predictive capabilities of the proposed aging models, without compromising the underlying physical consistency.

By coupling the two degradation models and incorporating both mechanistic understanding and data-driven insights, this dissertation delivers a unified computational framework capable of simulating the long-term behavior of elastomeric materials under varied environmental exposures. The results not only enhance our understanding of how oxidative and inert aging conditions uniquely and jointly affect polymer durability, but also provide a practical foundation for the design of next-generation elastomers with improved resistance to environmental degradation.

Copyright by YANG CHEN 2025

This dissertation is dedicat To my respectful parents, And to my caring an	Wuyun Chen and V	Veiwei Zhang, for	always believing in me	

#### **ACKNOWLEDGMENTS**

I would like to express my heartfelt gratitude to my advisor, Dr. Roozbeh Dargazany, for his unwavering support. His insightful guidance, invaluable advice, and endless assistance have been crucial in making this journey possible.

Next, I extend my deepest appreciation to my committee members, Dr. Nizar Lajnef, Dr. Sara Roccabianca, and Dr. Venkatesh K. R. Kodur. It has been a privilege to benefit from their vast experiences over the years. The honor of attending their classes and drawing from their expertise has profoundly influenced my intellectual development as a graduate student.

I am also grateful for the assistance and camaraderie of my dear peers and friends in the High-Performance Materials (HPM) group. Special thanks to Vahid Morovati, Hamid Mohammadi, Amir Bahrololoumi, Aref Ghaderi, Sharif Alazhary, and Mamoon Shaafaey for sharing ideas and providing invaluable help throughout the experimental procedures.

## TABLE OF CONTENTS

CHAPTER 1: INTRODUCTION
CHAPTER 2: CONTINUUM MECHANICS
CHAPTER 3: CONSTITUTIVE RELATIONS
CHAPTER 4: MACHINE-LEARNED CONSTITUTIVE MODE FOR SINGE
CHAPTER 5: FINITE ELEMENT ANALYSIS
CHAPTER 6: INERT THERMAL AGING
CHAPTER 7: CONSTITUTIVE MODELING OF DIFFUSION-LIMITED OXIDATION (DLO) COUPLED WITH A LARGE DEFORMATION THEORY FOR POLYMER DEGRADATION
CHAPTER 8: GRAPHIC USER INTERFACE
BIBLIOGRAPHY
APPENDIX

# **CHAPTER 1: INTRODUCTION**

## 1.1: Motivation, Challenges and Objectives

Challenges: Despite the widespread use of polymer adhesives, accurately predicting their long-term performance remains a significant challenge, especially under harsh environmental conditions. One critical factor is thermal aging, which can drastically alter the mechanical and chemical integrity of the polymer network. This aging is typically accompanied by competing processes such as chain scission and additional cross-linking, both of which influence the stiffness, strength, and durability of the material.

Characterizing and modeling these phenomena is complicated by the nonlinear, time-dependent behavior of polymers and the interplay between physical and chemical degradation mechanisms. Moreover, the multiscale nature of the material response — from molecular changes at the chain level to macroscopic deformation behavior — necessitates a modeling approach that captures both microstructural evolution and continuum-scale performance.

Traditional constitutive models often fail to account for such micro-mechanical transformations, limiting their predictive capabilities. In addition, implementing these models within a finite element framework poses numerical challenges, particularly when large deformations and nonlinear elasticity are involved.

**Objectives:** The primary objective of this research is to develop a mechanistically informed, micromechanical model that captures the constitutive behavior of cross-linked polymer adhesives under inert thermal aging. Specifically, the model aims to:

- Capture the competitive and time-dependent effects of chain scission and cross-linking during thermal exposure;
- Relate molecular-scale damage mechanisms to macroscopic mechanical response;
- Implement the model within a finite element framework under plane stress conditions, incorporating consistent tangent stiffness for large deformation analysis;
- Validate the model using experimental data and numerical simulations, including compar-

isons with custom UMAT subroutines and continuum solvers;

 Provide insights to guide the design and life prediction of adhesive joints exposed to elevated temperatures in oxygen-limited environments.

By addressing these objectives, this work seeks to bridge the gap between chemical degradation processes and mechanical modeling, enabling a more accurate prediction of adhesive behavior over the service life of engineered systems.

## 1.2: Fundamentals of Cross-linked Polymers

#### 1.2.1: Fundamentals of Polymer Physics

The mechanical behavior of polymers is highly sensitive to temperature and the time scale of deformation. Polymers are inherently viscoelastic, exhibiting characteristics of both viscous fluids and elastic solids. At low temperatures or high loading rates, polymers behave in a glassy manner, often fracturing or deforming irreversibly under modest strains. At elevated temperatures or low strain rates, however, they can adopt a rubber-like response, sustaining large deformations (stretch ratios exceeding 2) without permanent set. Further increases in temperature result in behavior akin to viscous liquids, where deformation becomes irreversible and time-dependent.

Phenomenological models typically describe material response at a macroscopic level without incorporating explicit microstructural details. These models are often derived by: (i) proposing plausible strain energy functions, or (ii) extending small-strain elasticity theory to accommodate large strain regimes.

For hyperelastic rubber-like materials, two key assumptions are commonly made: (i) The material is isotropic in its undeformed state, exhibiting identical behavior in all directions, and (ii) The material is nearly incompressible, with negligible volume change upon deformation. Accordingly, modeling efforts frequently focus on homogeneous pure strains under these assumptions.

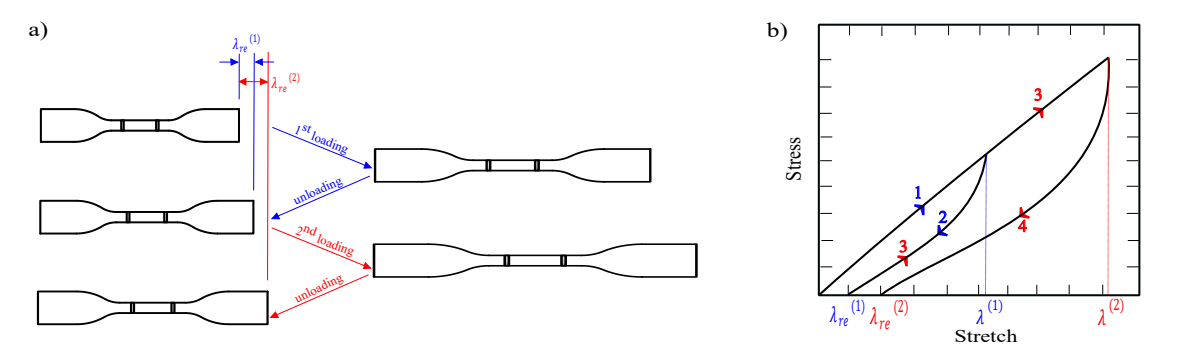


Figure 1.1: The Mullins effect with permanent set: (a) Two uniaxial tensile loading cycles; (b) Corresponding stress-stretch curves.

Cross-linked polymers generally exhibit pronounced nonlinear elasticity coupled with inelastic effects such as stress-softening (Mullins effect). Amorphous elastomers in particular demonstrate rate-dependent elastic-plastic responses due to their complex microstructure, as illustrated in Fig. 1.2. These behaviors arise from molecular mechanisms such as chain rearrangement, kink unfolding, and segment reorientation during loading.

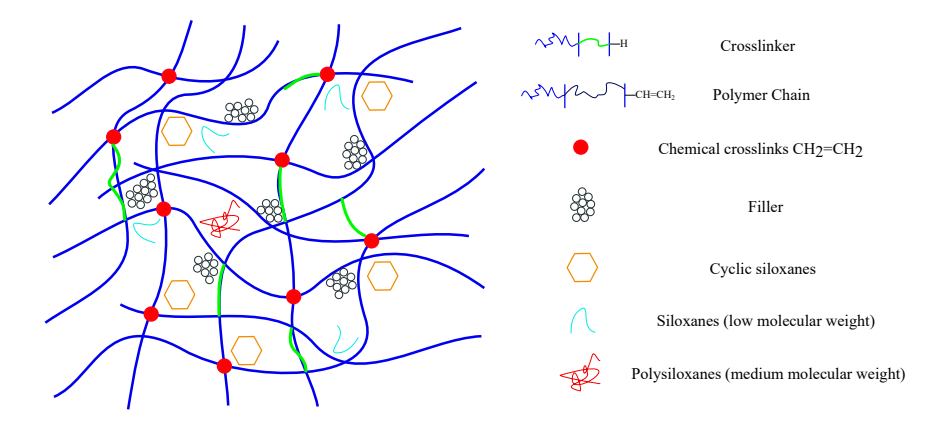


Figure 1.2: Schematic representation of the microstructure in filled elastomers.

#### Micro-stretch $\lambda^d$ :

In micromechanical network models, polymer chains oriented in direction d experience directional stretching governed by the deformation gradient F. The chain-level (micro) stretch is defined as:

$$\lambda^{\mathbf{d}} = 1 + \frac{\Delta L^{\mathbf{d}}}{L^{\mathbf{d}}},$$

where  $\Delta L^d$  is the elongation, and  $L^d$  is the initial chain length. The maximum sustainable micro-

stretch for a chain is limited by its geometry:

$$\lambda_{\text{limit}}^{d} = \frac{L_c}{\nu R_0}.$$

Here,  $L_c$  is the contour length,  $R_0$  is the end-to-end distance, and  $\nu > 1$  is the threshold for mechanical rupture [31]. Shorter chains are more susceptible to breakage due to higher stretch ratios.

#### Mechanisms of Breakage:

Chain failure can occur in various forms, including polymer-polymer detachment, cross-link rupture, desorption from filler surfaces, and chain slippage (see Fig.1.3). These microstructural mechanisms play a central role in damage evolution and are essential for understanding the Mullins effect and stress-softening behavior.

### History Dependence via Maximum Micro-stretch $\lambda_{\max}^d$ :

During cyclic loading, polymer chains progressively debond from aggregates, starting with the shortest chains. Once debonded, chains do not reattach, making the history of deformation critical. The maximum micro-stretch in a given direction d over the material's loading history is defined as:

$$\lambda_{\max}^{\mathbf{d}} = \max_{\tau \in (-\infty, t]} \lambda^{\mathbf{d}}(\tau).$$

This parameter serves as a key internal variable for modeling direction-dependent damage.

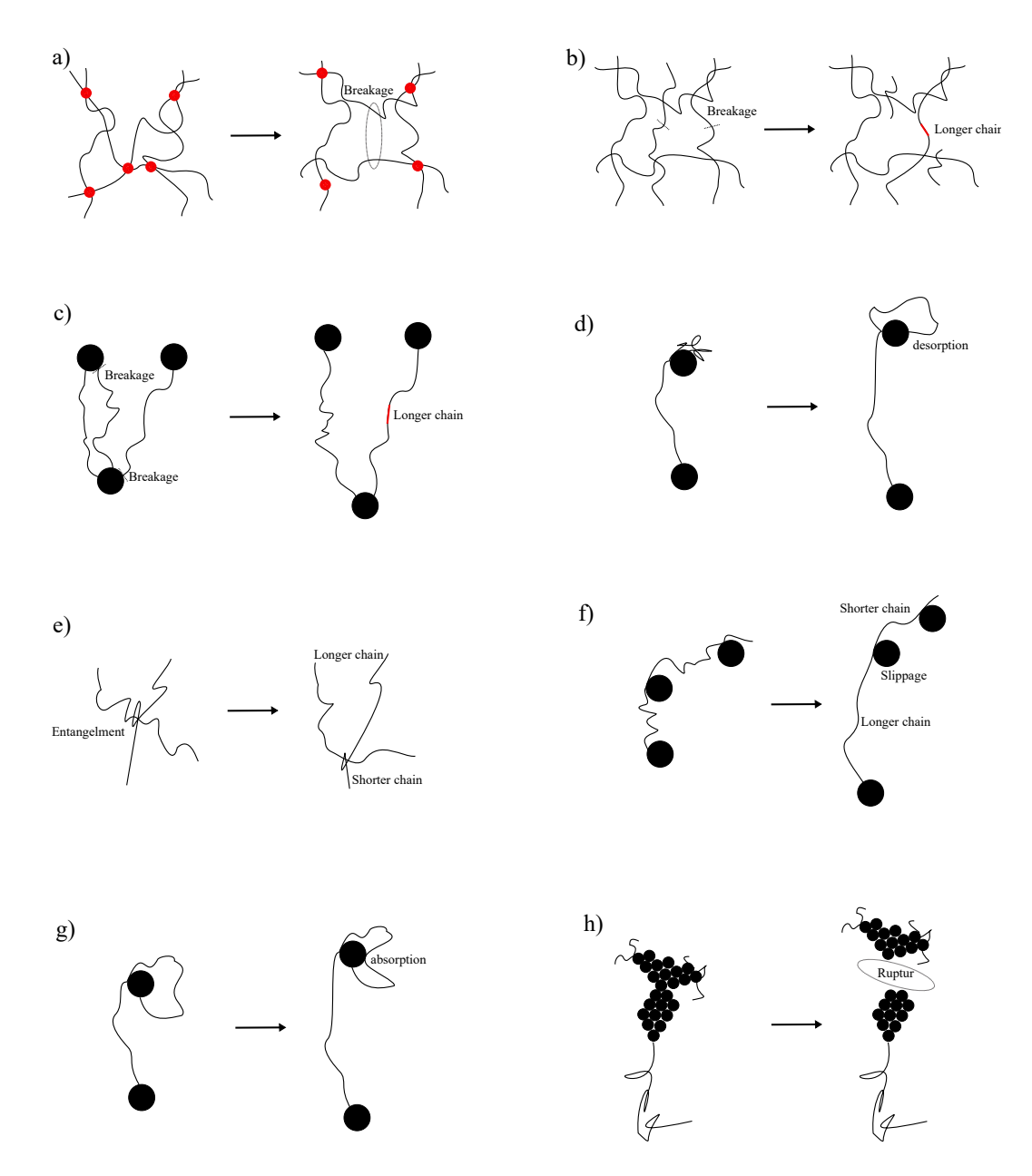


Figure 1.3: Mechanisms of chain damage in cross-linked polymers: (a) Cross-link breakage; (b) Chain scission; (c) Rupture of rubber–filler bonds; (d) Desorption from filler surface; (e) Chain slippage at entanglement sites; (f) Slippage over particle surfaces; (g) Re-adsorption onto particle surfaces; (h) Filler rupture.

## 1.3: Non-linear Features in Cross-Linked Polymers

Cross-linked polymers are commonly modeled as hyperelastic materials, characterized by their ability to undergo large, reversible deformations. However, their mechanical behavior also includes

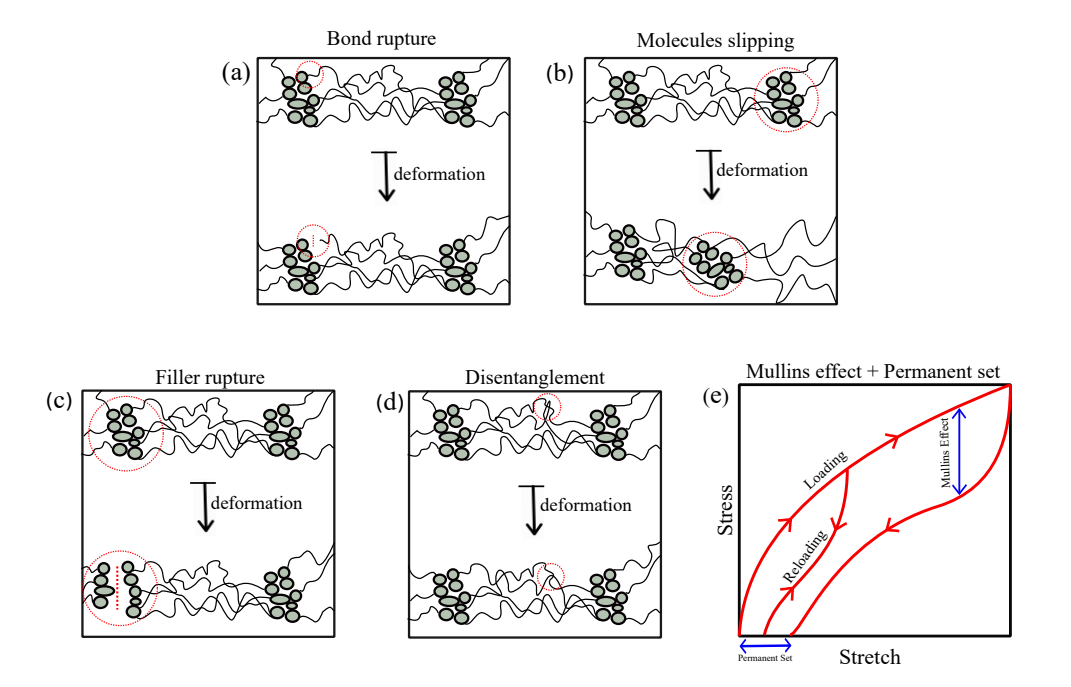


Figure 1.4: Schematic illustration of deformation-induced damage mechanisms in cross-linked polymers.

prominent inelastic features, particularly under cyclic or large-strain loading. One notable inelastic phenomenon is the *Mullins effect*, which refers to the stress-softening observed after the initial loading cycle [10, 85]. This effect is observed in both filled and unfilled cross-linked polymers.

To better understand the microstructural origins of such inelastic effects, Fig. 1.4 illustrates several deformation-induced damage mechanisms in amorphous polymer networks. These include:

- Chain scission [13]
- Chain disentanglement [53]
- Molecular slippage at junctions [62]
- Filler–matrix debonding and rupture of filler clusters [72]

These mechanisms collectively lead to permanent changes in the microstructure of the polymer network. As a result, materials often exhibit a residual strain upon unloading—referred to as the *permanent set*. While the permanent set is minimal in unfilled elastomers, it becomes significant in filled systems due to interfacial debonding and filler rupture, as depicted in Fig.1.4.

Traditional modeling of such nonlinear and inelastic behaviors has relied on two main ap-

proaches:

- **Phenomenological models**, which offer computational efficiency but lack physical interpretability and generalizability outside calibration conditions.
- Physics-based models, which provide greater fidelity but are often too complex for real-time
  or large-scale simulations.

To bridge this gap, we propose a hybrid framework that couples physically informed micro-mechanical theory with a machine-learned agent framework. Specifically, we develop a knowledge-driven ML model where internal variables evolve based on known physical laws and history-dependent damage. The learning agents (L-agents) are designed with memory structures to reflect material behavior, particularly relevant in rubbery polymers where damage evolution depends on the *maximum* historical strain rather than the full deformation path.

A microsphere-based formulation is adopted to account for directional dependence in the polymer matrix, enabling accurate modeling of inelastic effects such as stress-softening, hysteresis, and permanent set. The architecture of the neural network—including activation functions, number of hidden layers, and neurons—is tailored to balance complexity and accuracy. These modeling strategies are detailed in the following section.

## 1.4: Frame Independency

Frame objectivity, during rigid body motion, requires strain energy of the material remains unchanged. Thus, the material response should not depend on the choice of the reference frame. The strain energy frame independency can be written as

$$\Psi_m(\mathbf{QF}) = \Psi_m(\mathbf{F}),\tag{1.1}$$

where  $\mathbf{Q}$  is the rotation tensor. So, a constitutive law is frame independent if energy is left rotationally invariant. The mentioned condition is satisfied when the strain energy is a function of the right Cauchy-Green deformation tensor  $\mathbf{C}$ , due to

$$\mathbf{C}^{+} = (\mathbf{F}^{+})^{T} \mathbf{F}^{+} = \mathbf{F}^{T} \mathbf{Q}^{T} \mathbf{Q} \mathbf{F} = \mathbf{F}^{T} \mathbf{F} = \mathbf{C}, \tag{1.2}$$

which  $\mathbf{F}^+ = \mathbf{FQ}$ . The proposed model is a function of right Cauchy-Green deformation tensor. So, the frame independency condition is satisfied automatically.

## 1.5: Thermodynamic Consistency

#### 1.5.1: Polyconvexity

Polyconvexity is one of the known conditions which ensure the thermodynamic consistency. In this section, we briefly describe sufficient but not necessary free energy function conditions which guarantee the existence of minimizers of some variational principles. In order to understand polyconvexity, we start with some properties of convexity. Consider that  $\Psi_m(\mathbf{F})$  is the strain energy function on set of K. We can say  $\Psi_m(\mathbf{F})$  is convex on set of K if hessian matrix of  $\Psi_m(\mathbf{F})$  be positive in that set.

$$D^{2}\Psi_{m}\left(\mathbf{F}\right).\left(H,H\right)\geqslant0,\tag{1.3}$$

and for proof of polyconvexity we can mention that  $\mathbf{F} \to \Psi_m(\mathbf{F})$  is polyconvex if and only if there exist a function G such that

$$\Psi_m(\mathbf{F}) = G(\mathbf{F}, adj\mathbf{F}, \det\mathbf{F}), \tag{1.4}$$

and the function G is convex. Besides,  $\mathbf{F} = \frac{\mathbf{F}^{-1}}{\det \mathbf{F}}$  and the implication chain shows relations from convexity to ellipticity.

convexity  $\rightarrow$  polyconvexity  $\rightarrow$  quasiconvexity  $\rightarrow$  ellipticity.

The Hessian matrix of the strain energy is positive if

$$\frac{\partial \Psi_m^2}{\partial^2 \lambda_j^{d_i}} = \sum_{i=1}^{N_d} w_i \frac{\partial \psi_j^{d_i^2}}{\partial^2 \lambda_j^{d_i}} = \sum_{i=1}^{N_d} w_i \frac{\partial ANN_j(\mathbf{W_j}, \lambda_j^{\vec{d_i}}, \lambda_{j_{max}}^{\vec{d_i}})}{\partial \lambda_j^{d_i}} > 0, \qquad for \ j = 1, 2, ..., N_s.$$

$$(1.5)$$

If weights which connect the input of  $\lambda_j$  to other neurons be positive, the proposed model holds the condition of polyconvexity.

#### 1.5.2: Second Law of Thermodynamic

Because all of the constitutive models should satisfy the second law of thermodynamic, the satisfaction of this law should be checked for the proposed model. On the other hand, checking Clausius-Duhem inequality would be enough for this. Because  $\lambda_{j_{max}}$  is internal variables in the strain energy function of Cross-linked polymers, we can reduce the second law of thermodynamics to Clausius-Duhem inequality that shows thermodynamic consistency of the model in direction  $d_i$ . This inequality can be written as

$$\frac{\partial \Psi_m}{\partial \lambda_{jmax}} d_i \le 0 \qquad \forall d \qquad for j = 1, 2, ..., N_s.$$
 (1.6)

If we consider the energy of matrix as

$$\Psi_m = \sum_{i=1}^{N_d} \sum_{j=1}^{N_s} (\psi_j^{d_i}) w_i, \tag{1.7}$$

which

$$\psi_j^d = ANN_j(\mathbf{W_j}, \lambda_j^{\vec{d_i}}, \lambda_{j_{max}}^{\vec{d_i}}), \tag{1.8}$$

thus, Clausius-Duhem can be written as

$$\frac{\partial \Psi_{m}}{\partial \lambda_{j_{max}}^{d_{i}}} = \sum_{i=1}^{N_{d}} w_{i} \frac{\partial \psi_{j}^{d_{i}}}{\partial \lambda_{j_{max}}^{d_{i}}} = \sum_{i=1}^{N_{d}} w_{i} \frac{\partial ANN_{j}(\mathbf{W_{j}}, \lambda_{j}^{\vec{d_{i}}}, \lambda_{j_{max}}^{\vec{d_{i}}})}{\partial \lambda_{j_{max}}^{d_{i}}} \leq 0, \qquad for \ j = 1, 2, ..., N_{s}.$$

$$(1.9)$$

If weights that connect the input of  $\lambda_{j_{max}}$  to other neurons be negative, the proposed model holds the condition of thermodynamic consistency.

# **CHAPTER 2: CONTINUUM MECHANICS**

#### 2.1: Introduction

Continuum mechanics serves as a foundational framework for nonlinear finite element analysis, focusing on modeling solids and fluids with properties and responses characterized by smooth functions of spatial variables. This approach overlooks inhomogeneities such as molecular, grain, or crystal structures.

Consider a body in its initial state at time t=0; the domain of the body in this initial state is denoted as  $\Omega_0$  and referred to as the *initial configuration*. When describing the motion and deformation of the body, a configuration is essential as a reference for various equations; this is termed the *reference configuration*.

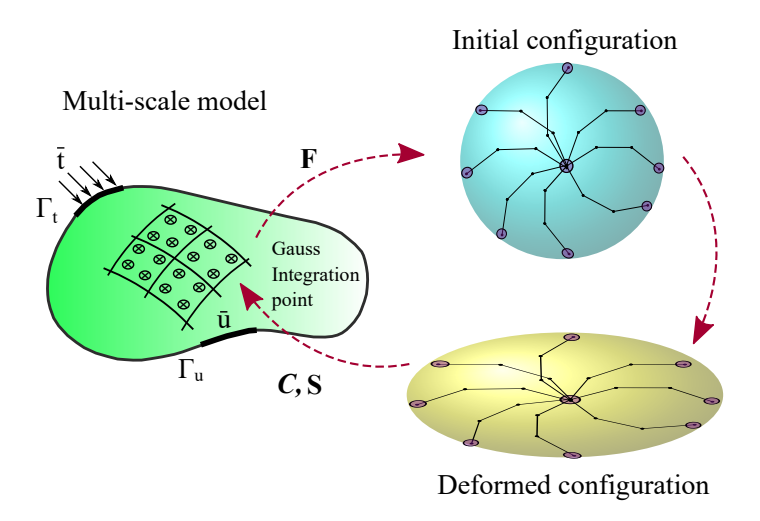


Figure 2.1: A schematic figure of the hierarchical micro-macro multi-scale approach.

In various instances, it becomes necessary to define a configuration known as the *undeformed* configuration, occupying  $\Omega_0$ . This undeformed configuration is synonymous with the initial condition. The domain of the body's current configuration is denoted as  $\Omega$  and is often referred to as the deformed configuration.

## 2.2: Eulerian and Lagrangian Coordinates

The position vector of a material point in the initial configuration is denoted as X, where

$$X = X_i \boldsymbol{e}_i = \sum_{i=1}^{n_{SD}} X_i \boldsymbol{e}_i, \tag{2.1}$$

where  $n_{SD}$  stands for the number of space dimensions,  $X_i$  represents the components of the position vector in the initial configuration, and  $\mathbf{e}_i$  are the unit base vectors of a rectangular Cartesian coordinate system. The vector variable  $\mathbf{X}$  for a specific material point remains constant over time; these variables  $\mathbf{X}$  are termed material coordinates or Lagrangian coordinates. The position of a point in the current configuration is expressed as

$$\mathbf{x} = x_i \mathbf{e}_i = \sum_{i=1}^{n_{SD}} x_i \mathbf{e}_i, \tag{2.2}$$

where  $x_i$  are the components of the position vector in the current configuration.

## 2.2.1: Eulerian and Lagrangian Description

Two methods are employed to depict the deformation and response of a continuum. In the first method, the material coordinates  $X_i$  and time t serve as the independent variables, represented as  $\mathbf{x} = \Box(\mathbf{X}, t)$ ; this method is known as the *material description* or *Lagrangian description*. In the second method, the independent variables are the spatial coordinates  $\mathbf{x}$  and time t. This is referred to as the *spatial* or *Eulerian description*. Distinct symbols are used to differentiate between independent variables.

#### 2.2.2: Deformation

Consider a continuum body B existing in three-dimensional Euclidean space at a given time  $t_0$ , as shown in Fig.2.2. Using the notation  $X \in \mathbb{E}^3$ , any point  $P_0$  on body B can be uniquely specified relative to any basis. As the body B moves through three-dimensional Euclidean space from time  $t_0$  to time t, it occupies an alternate geometric configuration referred to as  $\beta$ 's configuration. Since

the mapping from body B to  $\beta$  is one-to-one, point  $P_0$  on body B corresponds to point P.

To simplify the understanding of the mapping process, we label the regions of body B and  $\beta$  as the reference and current configurations, respectively. The positions of points P and  $P_0$  can be expressed using coordinates in a system denoted by  $\theta^i$  (where i = 1, 2, 3).

$$\mathbf{x} = \hat{\mathbf{x}} (\theta^1, \theta^2, \theta^3, t), \quad \mathbf{X} = \hat{\mathbf{X}} (\theta^1, \theta^2, \theta^3) = \hat{\mathbf{x}} (\theta^1, \theta^2, \theta^3, t_0), \quad i = 1, 2, 3,$$
 (2.3)

respectively. As a result, the displacement of point P may be calculated by

$$\boldsymbol{u} = \hat{\boldsymbol{u}} \left( \theta^1, \theta^2, \theta^3, t \right) = \boldsymbol{x} - \boldsymbol{X}. \tag{2.4}$$

Here, u represents the displacement vector. When we introduce Euclidean space with a set of pairwise orthogonal unit vectors, denoted as  $e_i$ , we have

$$X = X^{i} \boldsymbol{e}_{i}, \quad X^{j} = X \cdot \boldsymbol{e}_{j}, \quad j = 1, 2, 3,$$

$$\boldsymbol{u} = u^{i} \boldsymbol{e}_{i}, \quad u^{j} = \boldsymbol{u} \cdot \boldsymbol{e}_{j}, \quad j = 1, 2, 3,$$

$$\boldsymbol{x} = x^{i} \boldsymbol{e}_{i}, \quad x^{j} = \boldsymbol{x} \cdot \boldsymbol{e}_{j} = X^{j} + u^{j}, \quad j = 1, 2, 3,$$

$$(2.5)$$

where the Einstein summation convention is used to repeated indices.

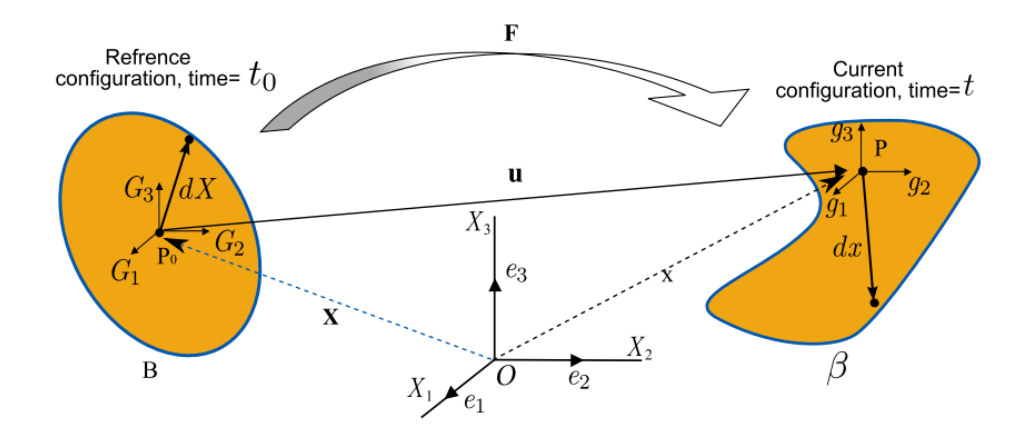


Figure 2.2: Description of body motion.

Body deformations can be easily described by vectors tangent to the coordinate lines in both the

reference and current configurations, particularly in the context of significant deformations. These tangent vectors are defined as follows

$$G_i = \frac{\partial X}{\partial \theta^i}, \quad g_i = \frac{\partial x}{\partial \theta^i}, \quad i = 1, 2, 3.$$
 (2.6)

Furthermore,  $G_i$  and  $g_i$  may be defined as the bases dual to  $G_i$  and  $g_i$ , implying that

$$\mathbf{G}_i \cdot \mathbf{G}^j = \delta_i^j$$
, and  $\mathbf{g}_i \cdot \mathbf{g}^j = \delta_i^j$ . (2.7)

Also, the deformation gradient tensor **F** can be represented by,

$$\mathbf{F} = Grad\mathbf{x},\tag{2.8}$$

where **F** can be written in a matrix format in two dimensions as

$$\mathbf{F} = \begin{bmatrix} \frac{\partial x_1}{\partial X_1} & \frac{\partial x_1}{\partial X_1} \\ \frac{\partial x_1}{\partial X_1} & \frac{\partial x_1}{\partial X_1} \end{bmatrix} = \begin{bmatrix} \frac{\partial \mathbf{x}}{\partial \mathbf{X}} & \frac{\partial \mathbf{x}}{\partial \mathbf{Y}} \\ \frac{\partial \mathbf{y}}{\partial \mathbf{X}} & \frac{\partial \mathbf{y}}{\partial \mathbf{Y}} \end{bmatrix}.$$
 (2.9)

In deformation kinematics, the deformation gradient tensor is a fundamental second-order tensor that describes the changes in material constituents during deformation. To this goal, consider dX and dx in reference and current configurations as infinitesimal material components, respectively. Then, one has

$$d\mathbf{x} = \mathbf{F}d\mathbf{X}, \quad d\mathbf{X} = \mathbf{F}^{-1}d\mathbf{x}. \tag{2.10}$$

Additionally, the changes in volume J may be derived by

$$J = \frac{dV}{dV_0} = \left| F_{\cdot j}^i \right| = \det \mathbf{F} > 0. \tag{2.11}$$

In the current setup, the lengths of the material components are provided by

$$||d\mathbf{x}||^2 = d\mathbf{x} \cdot d\mathbf{x} = d\mathbf{X} (\mathbf{F}^{\mathsf{T}} \mathbf{F}) d\mathbf{X} = d\mathbf{X} \mathbf{C} d\mathbf{X},$$

$$||d\mathbf{X}||^2 = d\mathbf{X} \cdot d\mathbf{X} = d\mathbf{x} (\mathbf{F}^{-\mathsf{T}} \mathbf{F}^{-1}) d\mathbf{x} = d\mathbf{x} \mathbf{b}^{-1} d\mathbf{x},$$
(2.12)

where

$$\mathbf{C} = \mathbf{F}^{\mathsf{T}} \mathbf{F} = g_{ij} \mathbf{G}^i \otimes \mathbf{G}^j, \quad \mathbf{b} = \mathbf{F}^{\mathsf{T}} = G^{ij} \mathbf{g}_i \otimes \mathbf{g}_j,$$
 (2.13)

are referred to as the right and left Cauchy-Green tensor, respectively. The principal invariant of C mentioned as

$$\mathbf{I}_{1}(\mathbf{C}) = tr(\mathbf{C}), \qquad \qquad \mathbf{I}_{2}(\mathbf{C}) = \frac{1}{2}((\mathbf{I}_{1}(\mathbf{C}))^{2} - tr(\mathbf{C}^{2})), \qquad \qquad \mathbf{I}_{3}(\mathbf{C}) = \det(\mathbf{C}). \quad (2.14)$$

To ascertain the stretch of a material element, divide the deformed length by the referenced length of the material element. To achieve this, the stretch in the direction of N is obtained by summing the unit vectors N and N along the material element dX and its counterpart dx.

$$\lambda(\mathbf{N}) = \frac{dx}{dX} = \sqrt{\frac{\|d\mathbf{x}\|^2}{\|d\mathbf{X}\|^2}} = \sqrt{\frac{dX\mathbf{NCN}dX}{dX^2}} = (\mathbf{NCN})^{\frac{1}{2}}.$$
 (2.15)

#### 2.3: Strain Measures

Unlike in linear elasticity, nonlinear continuum mechanics employs various measures of strain and strain rate. However, only two of these measures are taken into consideration here.

- 1. The Green (Green-Lagrange) strain, **E**.
- 2. The rate-of-deformation tensor, **D**.

A strain measure should exhibit zero values for any rigid body motion, particularly for rigid body rotation. If a strain measure does not satisfy this condition, it would result in predicting non-zero strains and consequently non-zero stresses during rigid body rotation. This fundamental reason underlies the abandonment of the conventional linear strain displacement equations in nonlinear theory.

#### 2.3.1: Green Strain Tensor

The Green strain tensor **E** is defined by

$$ds^2 - dS^2 = 2d\mathbf{X} \cdot \mathbf{E} \cdot d\mathbf{X}.$$
 (2.16)

The Green strain is defined as the disparity between the square of an infinitesimal segment in the current (deformed) configuration and its counterpart in the initial (undeformed) configuration. This concept becomes more evident when expressed in indicial notation.

$$d\mathbf{x} \cdot d\mathbf{x} = dx_i dx_i = F_{ij} dX_j F_{ik} dX_k = d\mathbf{X} \cdot (\mathbf{F}^T \cdot \mathbf{F}) \cdot d\mathbf{X}. \tag{2.17}$$

As  $d\mathbf{X} \cdot \mathbf{F}^T \cdot \mathbf{F} \cdot d\mathbf{X} - d\mathbf{X} \cdot \mathbf{I} \cdot d\mathbf{X} - d\mathbf{X} \cdot 2\mathbf{E} \cdot d\mathbf{X} = 0$ , it follows that

$$\mathbf{E} = \frac{1}{2} \left( \mathbf{F}^T \cdot \mathbf{F} - \mathbf{I} \right) \text{ or } E_{ij} = \frac{1}{2} \left( F_{ik}^T F_{kj} - \delta_{ij} \right). \tag{2.18}$$

#### 2.3.2: Rate-of-Deformation

The second kinematic measure to be discussed is the rate-of-deformation tensor **D**. Unlike the Green strain tensor, it serves as a rate measure of deformation. The velocity gradient is defined as:

$$\mathbf{L} = \frac{\partial \mathbf{v}}{\mathbf{x}} = (grad\mathbf{v})^T \text{ or } L_{ij} = \frac{\partial v_i}{\partial x_i}.$$
 (2.19)

The velocity gradient tensor can be decomposed into symmetric and skew-symmetric components through the following

$$\mathbf{L} = \frac{1}{2} (\mathbf{L} + \mathbf{L}^{T}) + \frac{1}{2} (\mathbf{L} - \mathbf{L}^{T}) \text{ or } L_{ij} = \frac{1}{2} (L_{ij} + L_{ji}) + \frac{1}{2} (L_{ij} - L_{ji}).$$
 (2.20)

The rate-of-deformation tensor  $\mathbf{D}$  is defined as the symmetric part of  $\mathbf{L}$ , while the spin tensor  $\mathbf{W}$  is the skew-symmetric part of  $\mathbf{L}$ . With these definitions, we can express

$$\mathbf{L} = \mathbf{D} + \mathbf{W} \text{ or } L_{ij} = v_{i,j} = D_{ij} + W_{ij}$$

$$\mathbf{D} = \frac{1}{2} \left( \mathbf{L} + \mathbf{L}^T \right) \text{ or } D_{ij} = \frac{1}{2} \left( \frac{\partial v_i}{\partial x_j} + \frac{\partial v_j}{\partial x_i} \right)$$

$$\mathbf{W} = \frac{1}{2} \left( \mathbf{L} - \mathbf{L}^T \right) \text{ or } W_{ij} = \frac{1}{2} \left( \frac{\partial v_i}{\partial x_j} - \frac{\partial v_j}{\partial x_i} \right). \quad (2.21)$$

For deriving a unified expression connecting these two measures of strain rate, we have

$$\mathbf{D} = \frac{1}{2} \left( \mathbf{L} + \mathbf{L}^T \right) = \frac{1}{2} \left( \dot{\mathbf{F}} \cdot \mathbf{F}^{-1} + \mathbf{F}^{-T} \cdot \dot{\mathbf{F}}^T \right). \tag{2.22}$$

Taking time derivative of the Green strain, we got

$$\dot{\mathbf{E}} = \frac{1}{2} \frac{D}{Dt} \left( \mathbf{F}^T \cdot \mathbf{F} - \mathbf{I} \right) = \frac{1}{2} \left( tens F \cdot \dot{\mathbf{F}} + \dot{\mathbf{F}}^T \cdot \mathbf{F} \right). \tag{2.23}$$

The above can easily yield

$$\mathbf{D} = \mathbf{F}^{-T} \cdot \dot{\mathbf{E}} \cdot \mathbf{F}^{-1} \text{ or } D_{ij} = F_{ij}^{-T} \dot{E}_{kl} F_{lj}^{-1}. \tag{2.24}$$

The time integral of the Green strain rate is path-independent, whereas the time integral of the rate-of-deformation is not path-independent.

#### 2.4: Stress Measures

In nonlinear problems, different stress measures can be defined. Three stress measures are under consideration.

- 1. The Cauchy stress,  $\sigma$
- 2. The nominal stress tensor, P, closely related to the first Piola-Kirchhoff stress
- 3. The second-Piola Kirchhoff stress tensor, S.

The stress are defined by Cauchy's law

$$\mathbf{n} \cdot \boldsymbol{\sigma} d\Gamma = \mathbf{t} d\Gamma, \tag{2.25}$$

where *t* is the traction. In the initial configuation the counterpart is

$$\mathbf{n}_0 \cdot \mathbf{P} d\Gamma_0 = \mathbf{t}_0 d\Gamma. \tag{2.26}$$

Please note that the normal is consistently oriented to the left. The definition of the second-Piola Kirchhoff stress is given by

$$\mathbf{n}_0 \cdot \mathbf{S} d\Gamma_0 = \mathbf{F}^{-1} \cdot \mathbf{t}_0 d\Gamma_0. \tag{2.27}$$

Cauchy stress $\sigma$	Nominal stress P	2nd Piola-Kirchhoff stress S
$\sigma$	$\mathbf{J}^{-1}\mathbf{F}\cdot\mathbf{P}$	$\mathbf{J}^{-1}\mathbf{F}\cdot\mathbf{S}\cdot\mathbf{F}$
$\mathbf{P} = \mathbf{J}\mathbf{F}^{-1}\cdot\boldsymbol{\sigma}$	-	$\mathbf{S}\cdot\mathbf{F}^{T}$
$\mathbf{S} = \mathbf{J}\mathbf{F}^{-1}\cdot\boldsymbol{\sigma}\cdot\mathbf{F}^{-T}$	$\mathbf{P}\cdot\mathbf{F}^{-T}$	-
$ au = \mathbf{J} oldsymbol{\sigma}$	$\mathbf{F}\cdot\mathbf{P}$	$\mathbf{F}\cdot\mathbf{S}\cdot\mathbf{F}^{T}$

## 2.5: Conservation Laws

After formulating the kinematics to represent potential deformed states of a continuous medium, it's crucial to note that these fields alone are insufficient for predicting the specific configuration a body will assume under a given applied load. Achieving such predictions requires an extension of the principles of mechanics to encompass a continuum medium, coupled with the application of thermodynamic laws. In this context, we are considering four conservation laws relevant to thermomechanical systems.

**Gauss's Theorem:** In the derivation of conservation equations, Gauss's theorem is a frequently employed tool. This theorem establishes a connection between integrals over a domain and an integral over the boundary of that domain. Specifically, Gauss's theorem states that when  $f(\mathbf{x})$  is

piecewise continuously differentiable—a  $C^0$  function then

$$\int_{\Omega} \frac{\partial f(\mathbf{x})}{\partial x_i} d\Omega = \int_{\Gamma} \mathbf{n}_i f(\mathbf{x}) d\Gamma.$$
 (2.28)

The theorem remains applicable to any domain, including the reference domain, where for a  $C^0$  function  $f(\mathbf{X})$ , we have

$$\int_{\Omega_0} \frac{\partial f(\mathbf{X})}{\partial x_i} d\Omega_0 = \int_{\Gamma_0} \mathbf{n}_i^0 f(\mathbf{X}) d\Gamma_0.$$
 (2.29)

**Reynolds' Transport Theorem:** The material time derivative of an integral signifies how fast the integral changes over a material domain. This domain moves with the material, ensuring that points on its boundary remain fixed on the boundary, with no mass flux across the boundaries. The various formulations for material time derivatives of integrals are referred to as Reynolds' transport theorem. The definition of the material time derivative of an integral is

$$\frac{D}{Dt} \int_{\Omega} f d\Omega = \lim_{\Delta t \to 0} \frac{1}{\Delta t} \left( \int_{\Omega_{\tau + \Delta t}} f(\mathbf{x}, \tau + \Delta t) d\Omega - \int_{\Omega_{\tau}} f(\mathbf{x}, \tau) d\Omega \right), \tag{2.30}$$

here,  $\Omega_{\tau}$  represents the spatial domain at time  $\tau$ , and  $\Omega_{\tau+\Delta t}$  denotes the spatial domain occupied by the same material points at time  $\tau+\Delta t$ . The derivation of Reynolds' transport theorem is achieved through the definition of the material time derivative, yielding

$$\frac{D}{Dt} \int_{\Omega} f d\Omega = \int_{\Omega} \left( \frac{\partial f}{\partial t} + v_i \frac{\partial f}{\partial x_i} + \frac{\partial v_i}{\partial x_i f} \right) d\Omega = \int_{\Omega} \left( \frac{\partial f}{\partial t} + \frac{\partial (v_i f)}{\partial x_i} \right), \tag{2.31}$$

which can be written in tensor form as

$$\frac{D}{Dt} \int_{\Omega} f d\Omega = \int_{\Omega} \left( \frac{\partial f}{\partial t} + div(\mathbf{v}f) \right) d\Omega. \tag{2.32}$$

**Mass conservation:** A fundamental principle in classical mechanics asserts that mass is an invariant quantity, immune to creation or annihilation; instead, it can only experience deformation in

response to applied loads. The mass  $m(\Omega)$  of a material domain  $\Omega$  is determined by

$$m(\Omega) = \int_{\Omega} \rho(\mathbf{x}, t) d\Omega, \qquad (2.33)$$

here,  $\rho(\mathbf{x},t)$  represents the density. Mass conservation dictates that the mass of any material domain remains constant, as no material flows through the boundaries of a material domain, and there is no consideration for mass-to-energy conversion. Following the principle of mass conservation, the material time derivative of  $m(\Omega)$  is zero, indicating

$$\frac{Dm}{Dt} = \frac{D}{Dt} \int_{\Omega} \rho d\Omega = 0.$$
 (2.34)

Applying Reynolds's theorem, Eqn. 2.34 yields

$$\int_{\Omega} = \left(\frac{D\rho}{Dt} + \rho div(\mathbf{v})\right) d\Omega = 0.$$
 (2.35)

Since this holds for any subdomain  $\Omega$ , it follows that

$$\frac{D\rho}{Dt} + \rho div(\mathbf{v}) = 0; \text{ or } \frac{D\rho}{Dt} + \rho v_{i,i} = 0 \text{ or } \dot{\rho} + \rho v_{i,i} = 0.$$
(2.36)

The aforementioned equation is the expression of mass conservation, commonly referred to as the *continuity equation*. It stands as a first-order partial differential equation.

Conservation of Linear Momentum: The equation derived from the principle of linear momentum conservation holds significance in nonlinear finite element procedures. Linear momentum conservation aligns with Newton's second law of motion, linking the forces acting on a body to its acceleration. We consider an arbitrary domain  $\Omega$  with a boundary  $\Gamma$ , subjected to body forces  $\rho b$  and surface reactions t (force per unit area). The total force is determined by

$$f(t) = \int_{\Omega} \rho \boldsymbol{b}(\mathbf{x}, t) d\Omega = \int_{\Gamma} \boldsymbol{t}(\mathbf{x}, t) d\Gamma.$$
 (2.37)

The linear momentum is given by

$$\mathbf{p}(t) = \int_{\Omega} \rho \mathbf{v}(\mathbf{x}, t) d\Omega, \tag{2.38}$$

where  $\rho v$  is the linear momentum per unit volume. Using the material time derivative of the linear momentum, this gives

$$\frac{D\mathbf{p}}{Dt} = \mathbf{f} \Rightarrow \frac{D}{Dt} \int_{\Omega} \rho \mathbf{v} d\Omega = \int_{\Omega} \rho \mathbf{b} d\Omega + \int_{\Gamma} \mathbf{t} d\Gamma. \tag{2.39}$$

Reynolds' transport theorem applied to LHS integral gives

$$\frac{D}{Dt} \int_{\Omega} \rho \mathbf{v} d\Omega = \int_{\Omega} \left( \frac{D}{Dt} (\rho \mathbf{v}) + div(\mathbf{v}) \rho \mathbf{v} \right) = \int_{\Omega} \left[ \rho \frac{D\mathbf{v}}{Dt} + \mathbf{v} \left( \frac{D\rho}{Dt} + \rho div(\mathbf{v}) \right) \right] d\Omega, \quad (2.40)$$

where the second equality is obtained by using the product rule of derivatives for the first term of the integrand and rearranging terms. To convert it into a domain integral, we invoke Cauchy's relation and Gauss's theorem in sequence, giving

$$\int_{\Gamma} \mathbf{t} d\Gamma = \int_{\Gamma} \mathbf{n} \cdot \sigma d\Gamma = \int_{\Omega} \nabla \cdot \boldsymbol{\sigma} d\Omega \text{ or } \int_{\Gamma} t_j d\Gamma = \int_{\Gamma} n_i \sigma_{ij} d\Gamma = \int_{\Omega} \frac{\partial \sigma_{ij}}{\partial x_i} d\Omega.$$
 (2.41)

In nonlinear continuum mechanics, unlike in linear continuum mechanics, it is crucial to develop the habit of placing the divergence operator appropriately. This is because certain stress tensors, like the nominal stress, lack symmetry. In cases where the stress is asymmetric, the left and right divergence operators yield distinct results. This distinction is illustrated by

$$\int_{\Omega} \left( \rho \frac{D \mathbf{v}}{D t} - \rho \mathbf{b} - \nabla \cdot \boldsymbol{\sigma} \right) d\Omega. \tag{2.42}$$

Therefore, if the integrand  $C^{-1}$ , since upper equation holds for an arbitrary domain, it yields

$$\rho \frac{D\mathbf{v}}{Dt} = \nabla \cdot \boldsymbol{\sigma} + \rho \mathbf{b} \equiv \operatorname{div} \boldsymbol{\sigma} + \rho \mathbf{b} \text{ or } \rho \frac{Dv_i}{Dt} = \frac{\partial \sigma_{ij}}{\partial x_j} + \rho b_i. \tag{2.43}$$

This is referred to as the momentum equation, also known as the balance of linear momentum.

**Equilibrium Equation:** In numerous scenarios, loads are applied gradually, and interfacial forces are negligible. Under such circumstances, the acceleration in the momentum equation diminishes, leading to

$$\nabla \cdot \boldsymbol{\sigma} + \rho \mathbf{b} = 0; \ or \ \frac{\partial \sigma_{ij}}{\partial x_j} + \rho b_j = 0.$$
 (2.44)

This equation is termed the equilibrium equation. Situations to which the equilibrium equation applies are commonly referred to as static problems.

**Conservation of Energy:** The principle of conservation of energy, also known as the energy balance principle, asserts that the rate of change of total energy is equal to the work done by the body forces and surface reactions, in addition to the heat energy supplied to the body by the heat flux and other sources of heat.

The rate of change of total energy in the body is expressed as

$$\mathbf{P}^{tot} = \mathbf{P}^{int} + \mathbf{P}^{kin}, \mathbf{P}^{int} = \frac{D}{Dt} \int \Omega \rho \dot{w}^{int} d\Omega, \ \mathbf{P}^{kin} = \frac{D}{Dt} \int_{\Omega} \frac{1}{2} \rho \mathbf{v} \cdot \mathbf{v} d\Omega, \tag{2.45}$$

here,  $\mathbf{P}^{int}$  represents the rate of change of internal energy, and  $\mathbf{P}^{kin}$  represents the rate of change of kinetic energy. The rate of work performed by the body forces in the domain and the reactions on the surface is given by

$$\mathbf{P}^{ext} = \int_{\Omega} \mathbf{v} \cdot \rho \mathbf{b} d\Omega + \int_{\Gamma} \mathbf{v} \cdot \mathbf{t} d\Gamma = \int_{\Omega} v_i \rho b_i d\Omega + \int_{\Gamma} v_i t_i d\Gamma. \tag{2.46}$$

The power supplied by heat sources s and the heat flux q is

$$\mathbf{P}^{heat} = \int_{\Omega} \rho s d\Omega - \int \mathbf{n} \cdot \mathbf{q} d\Gamma = \int_{\Omega} \rho s d\Omega - \int_{\Gamma} n_i q_i d\Gamma, \tag{2.47}$$

In the heat flux term, the negative sign signifies that positive heat flow is directed outward from

Eulerian description	Tensor form	Indicial Form
Mass conservation	$\frac{D\rho}{Dt} + \rho div(\mathbf{v}) = 0$	$\dot{\rho} + \rho v_{i,i}$
Linear momentum conservation	$ ho rac{\ddot{D} oldsymbol{v}}{Dt} =  abla \cdot \sigma +  ho oldsymbol{b}$	$\rho \frac{Dv_i}{Dt} = \frac{\partial \sigma_{ij}}{\partial x_j} + \rho b_i$
Energy conservation	$\rho \frac{Dw^{int}}{Dt} = \mathbf{D} : \sigma - \nabla \cdot \boldsymbol{q} + \rho s$	·
Lagrangian description	Tensor form	Indicial Form
Mass conservation	$\rho(\mathbf{X}, t)\mathbf{J}(\mathbf{X}, t) = \rho_0(\mathbf{X})$	$\rho \mathbf{J} = \rho_0$
Linear momentum conservation	$ ho_0 rac{\partial oldsymbol{v}(\mathbf{X},t)}{\partial t} =  abla_0 \cdot \mathbf{P} +  ho_0 \mathbf{b}$	$\rho_0 \frac{\partial v_i(\mathbf{X},t)}{\partial t} = \frac{\partial P_{ij}}{\partial X_i} + \rho_0 b_i$
Energy conservation	$\rho_0 \dot{w}^{int} = \rho_0 \frac{\partial w^{int}(\mathbf{X},t)}{\partial t} = \dot{\mathbf{F}}^T : \mathbf{P} - \nabla_0 \cdot \hat{\boldsymbol{q}} + \rho_0 s$	·

Table 2.1: Conservation equations.

the body. The conservation of energy is expressed as

$$\mathbf{P}^{tot} = \mathbf{P}^{ext} + \mathbf{P}^{heat}. (2.48)$$

In other words, the first law of thermodynamics states that the rate of change of the total energy in the body, comprising internal and kinetic energies, is equivalent to the rate of work performed by external forces and the rate of work supplied by heat flux and energy sources.

The conservation equations are succinctly presented in the following Table 2.1, providing both tensor and indicial forms.

# **CHAPTER 3: CONSTITUTIVE**

# **RELATIONS**

## 3.1: Linear elasticity and Hooke's Law

Consider the stress strain curve  $\sigma=f(\epsilon)$  of a linear elastic material subjected to uni-axial stress loading conditions. For a given value of the strain  $\epsilon$ , the strain energy density per unit volume  $\psi=\hat{\psi}(\epsilon)$ , is defined as the area under the curve (see Fig.3.1), which can be expressed mathematically as

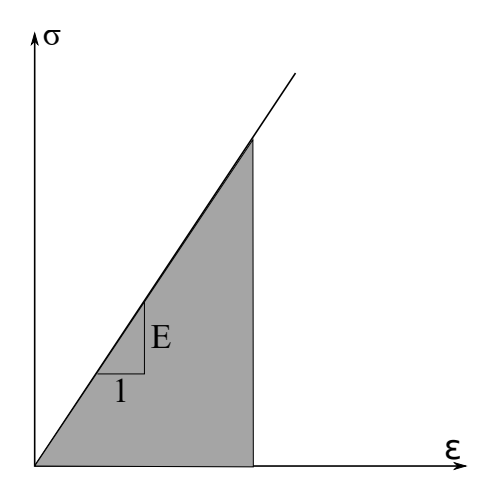


Figure 3.1: Stress-strain curve for a linear elastic material subject to uni-axial stress  $\sigma$ .

According to this definition,

$$\sigma = \frac{\partial \hat{\psi}}{\partial \epsilon} = E\epsilon. \tag{3.1}$$

In general, for possibly nonlinear elastic materials

$$\sigma_{ij} = \sigma_{ij}(\epsilon) = \frac{\partial \hat{\psi}}{\partial \epsilon_{ij}}.$$
(3.2)

It helps define Hooke's Law, the most general linear relation among all the components of the stress and strain tensor

$$\sigma_{ij} = C_{ijkl}\epsilon_{kl}. \tag{3.3}$$

In this expression,  $C_{ijkl}$  are the components of the fourth-order stiffness tensor of material properties of elastic moduli. The fourth-order tensor has 81 and 16 components for three-dimensional and two-dimensional problems, respectively. The strain energy density in this case is a quadratic function of the strain

$$\hat{\psi}(\epsilon) = \frac{1}{2} C_{ijkl} \epsilon_{ij} \epsilon_{kl}. \tag{3.4}$$

The stiffness tensor can be written in two different orthonormal basis as

$$\mathbf{C} = C_{ijkl} \mathbf{e}_i \otimes \mathbf{e}_j \otimes \mathbf{e}_k \otimes \mathbf{e}_l. \tag{3.5}$$

The stiffness tensor has the following minor symmetries which result from the symmetry of the stress and strain tensors

$$\sigma_{ij} = \sigma_{ji} \Rightarrow C_{ijkl} = C_{jikl}. \tag{3.6}$$

This symmetric characterization reduces the number of material constants from  $81 = 3 \times 3 \times 3 \times 3 \rightarrow 54 = 6 \times 3 \times 3$ . In a similar fashion we can make use of the symmetry of the strain tensor

$$\epsilon_{ij} = \epsilon_{ji} \Rightarrow C_{ijkl} \Longrightarrow C_{ijlk}.$$
 (3.7)

This further reduces the number of material constants to  $36 = 6 \times 6$ .

## 3.2: Isotropic linear elastic materials

The constitutive law for an isotropic, linear elastic and homogeneous material is given by the following equation

$$C_{ijkl} = \lambda \delta_{ij} \delta_{kl} + \mu \left( \delta_{ik} \delta_{jl} + \delta_{il} \delta_{jk} \right), \tag{3.8}$$

where  $\delta_{ij}$  is the Kronecker-delta, and  $\lambda, \mu$  are the Lame constants. Replacing in  $\sigma_{ij} = C_{ijjkl}\epsilon_{kl}$ , gives

$$\sigma_{ij} = \lambda \delta_{ij} \epsilon_{kk} + \mu \left( \epsilon_{ij} + \epsilon_{ji} \right). \tag{3.9}$$

The compliance form of Hooke's law can be written in indicial notation as

$$\epsilon_{ij} = \frac{1}{E} \left[ (1 + \nu) \,\sigma_{ij} - \nu \sigma_{kk} \delta_{kk} \right]. \tag{3.10}$$

It can be written in matrix form

$$\begin{bmatrix} \epsilon_{11} \\ \epsilon_{22} \\ \epsilon_{33} \\ 2\epsilon_{23} \\ 2\epsilon_{13} \\ 2\epsilon_{12} \end{bmatrix} = \frac{1}{E} \begin{bmatrix} 1 & -\nu & -\nu & 0 & 0 & 0 & 0 \\ & 1 & -\nu & 0 & 0 & 0 & 0 \\ & & 1 & 0 & 0 & 0 & 0 \\ & & & 2(1+\nu) & 0 & 0 & 0 \\ & & & & 2(1+\nu) & 0 & 0 \\ & & & & & 2(1+\nu) \end{bmatrix} \begin{bmatrix} \sigma_{11} \\ \sigma_{22} \\ \sigma_{33} \\ \sigma_{23} \\ \sigma_{13} \\ \sigma_{12} \end{bmatrix}.$$
(3.11)

Invert and compare with

$$\begin{bmatrix} \sigma_{11} \\ \sigma_{22} \\ \sigma_{33} \\ \sigma_{23} \\ \sigma_{13} \\ \sigma_{12} \end{bmatrix} = \frac{1}{E} \begin{bmatrix} \lambda + 2\mu & \lambda & \lambda & 0 & 0 & 0 \\ & \lambda + 2\nu & \lambda & 0 & 0 & 0 \\ & & \lambda + 2\mu & 0 & 0 & 0 \\ & & & \nu & 0 & 0 \\ & & & \nu & 0 & 0 \\ & & & \nu & 0 \\ & & & & \nu \end{bmatrix} \begin{bmatrix} \epsilon_{11} \\ \epsilon_{22} \\ \epsilon_{33} \\ 2\epsilon_{23} \\ 2\epsilon_{13} \\ 2\epsilon_{12} \end{bmatrix},$$
(3.12)

and concluded that

$$\lambda = \frac{E\nu}{(1+\nu)(1-2\nu)}; \ \mu = G = \frac{E}{2(1+\nu)}.$$
 (3.13)

## 3.3: 2D Formulations for Solid Mechanics

It is assumed that 2D means the xy plane, and that z is the out-of-plane direction. Plane-stress and Plane-strain are two terms commonly come across in finite element analysis. These are essentially two variations of 2D analysis, with difference in their assumptions.

#### 3.3.1: Hooke's Law for Plane Stress

For the simplification of **plane stress**, where the stresses in the z direction are considered to be negligible.  $\sigma_{33} = \sigma_{23} = \sigma_{13} = 0$ , the stress-strain compliance relationship for an isotropic material reduces to a simple  $3 \times 3$  matrix, the compliance matrix is written as

$$\begin{bmatrix} \epsilon_{11} \\ \epsilon_{22} \\ 2\epsilon_{12} \end{bmatrix} = \frac{1}{E} \begin{bmatrix} 1 & -\nu & 0 \\ -\nu & 1 & 0 \\ 0 & 0 & 2(1+\nu) \end{bmatrix} \begin{bmatrix} \sigma_{11} \\ \sigma_{22} \\ \sigma_{12} \end{bmatrix}.$$
(3.14)

The stiffness matrix for plane stress is found by inverting the plane stress compliance matrix, and is given by

$$\begin{bmatrix} \sigma_{11} \\ \sigma_{22} \\ \sigma_{12} \end{bmatrix} = \frac{E}{1 - \nu^2} \begin{bmatrix} 1 & \nu & 0 \\ \nu & 1 & 0 \\ 0 & 0 & \frac{1 - \nu}{2} \end{bmatrix} \begin{bmatrix} \epsilon_{11} \\ \epsilon_{22} \\ 2\epsilon_{12} \end{bmatrix}.$$
 (3.15)

#### 3.3.2: Hooke's Law for Plane Strain

In the case of **plane strain**, where the strains in the z direction are considered to be negligible,  $\epsilon_3 3 = \epsilon_{23} = \epsilon_{13} = 0$ , the stiffness matrix reduces to a simple 3 matrix

$$\begin{bmatrix} \epsilon_{11} \\ \epsilon_{22} \\ 2\epsilon_{11} \end{bmatrix} = \frac{1}{E} \begin{bmatrix} 1 - \nu^2 & -\nu(1+\nu) & 0 \\ -\nu(1+\nu) & 1 - \nu^2 & 0 \\ 0 & 0 & 2(1+\nu) \end{bmatrix} \begin{bmatrix} \sigma_{11} \\ \sigma_{22} \\ \sigma_{12} \end{bmatrix}.$$
(3.16)

Inverting stiffness matrix gives compliance matrix, which is written as

$$\begin{bmatrix} \sigma_{11} \\ \sigma_{22} \\ \sigma_{12} \end{bmatrix} = \frac{E}{(1+\nu)(1-2\nu)} \begin{bmatrix} 1-\nu & \nu & 0 \\ \nu & 1-\nu & 0 \\ 0 & 0 & \frac{1-2\nu}{2} \end{bmatrix} \begin{bmatrix} \epsilon_{11} \\ \epsilon_{22} \\ 2\epsilon_{12} \end{bmatrix}.$$
(3.17)

#### 3.3.3: Relations between Plane-stress and Plane-strain

#### Differences

- In plane-stress analysis, there can be strain in the thickness of the element. If the element is stretched, it wll get thinner, and if compressed, it will get thicker. Plane-stress is generally suitable for the analysis of an element with relatively limited depth in the out-of-plane direction. This analysis is typically offered only in structural or generic FE analysis software.
- In plane-strain analysis, the deformation in the out-of-plane (thickness) direction is fully fixed so no deformation could take place. Plane-strain is generally suitable for cross-sectional analysis of elements of almost infinite depth in the out-of-plane direction.

# CHAPTER 4: MACHINE-LEARNED CONSTITUTIVE MODE FOR SINGE

#### 4.1: Introduction

This chapter introduces a data-driven modeling framework that extends the environmental damage modeling presented in Chapter 2. The objective is to describe the coupled effects of mechanical and environmental damage on elastomeric matrices using a hybrid micro-mechanical and machine learning approach.

The elastomer matrix is modeled as a cooperative multi-agent system, where each agent is implemented as a conditionally activated neural network. These agents are rigorously constrained by the principles of thermodynamics and continuum mechanics. Compared to traditional physics-based methods, the integration of neural network agents within the micro-mechanical framework enables a new generation of hybrid models. These models retain the interpretability and simplicity of classical micro-mechanics while leveraging the adaptability and computational efficiency of machine learning.

It is important to note that the predictive accuracy of the proposed hybrid model depends heavily on the quality and diversity of the training data.

The formulation of this model adheres to several key design constraints:

- The model is defined in terms of strain energy to ensure physical consistency;
- A micro-sphere approach is used to reduce the dimensionality from 3D to 1D representations;
- A network decomposition strategy is adopted to isolate different inelastic mechanisms;
- Each one-dimensional subnetwork is represented by an independent learning agent.

These elements together constitute a cooperative multi-agent framework for simulating the complex response of elastomeric materials under coupled damage conditions.

# 4.2: Cooperative Multi-Agent System

Continuum Mechanics In the finite deformation regime, strain energy-based constitutive models offer significant advantages over classical stress-strain relations. These models inherently satisfy several key physical and mathematical conditions—such as normalization, growth behavior, isotropy, objectivity, and polyconvexity—ensuring uniqueness and stability of the solution. Moreover, strain energy-based formulations can be directly verified against the second law of thermodynamics, particularly through the Clausius—Duhem inequality. They are commonly constructed with respect to various work-conjugate stress-strain pairs, including:

```
Two-point tensors: (\mathbf{F}:\mathbf{P}) \to \mathbf{F}: deformation gradient, \mathbf{P}: first Piola-Kirchhoff stress;

Material tensors: (\mathbf{E}:\mathbf{S}) \to \mathbf{E}: Green-Lagrange strain, \mathbf{S}: second Piola-Kirchhoff stress;

Spatial tensors: (\mathbf{L}:\boldsymbol{\tau}) \to \mathbf{L}: Hencky strain, \boldsymbol{\tau}: Kirchhoff stress.
```

To address the challenge of incomplete data in modeling the finite deformation behavior of elastomers, we adopt a physics-informed order-reduction strategy. This includes the microsphere concept, network decomposition, continuum mechanics constraints, and polymer physics insights. The result is a micro-mechanical model where deep-learned agents, embedded as neural networks, represent 1D constitutive responses. These agents collectively capture the macroscopic behavior of the matrix based on learned local rules.

Building on our prior work [44], we reuse the knowledge integration framework developed for mechanically induced deformations, as illustrated in Fig. 4.1. The major innovation here is the replacement of the original network structure with a new class of machine learning models—conditional neural networks (CondNNs)—to define the learning agents (L-agents).

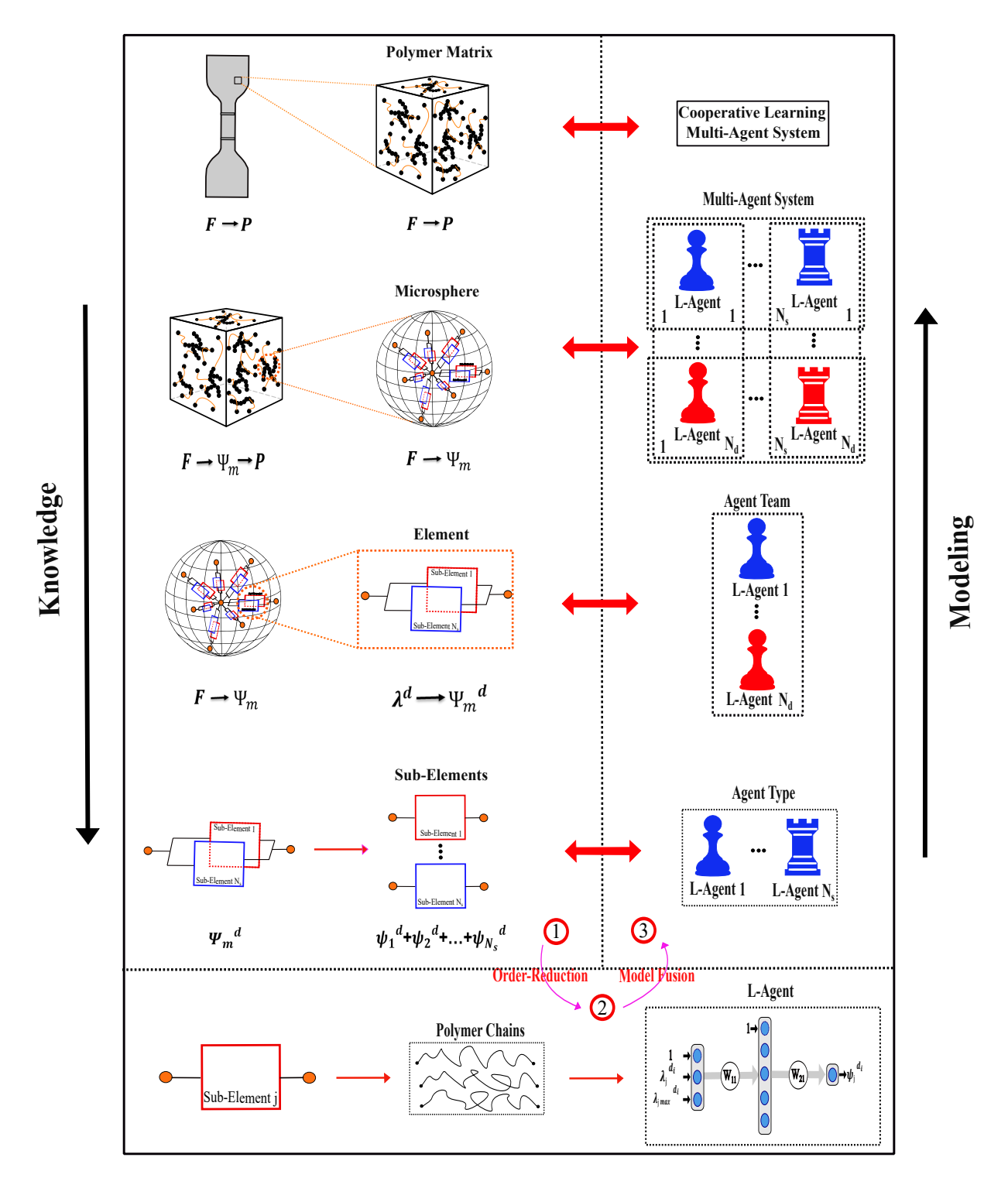


Figure 4.1: Schematic of the proposed model from order-reduction to model fusion.

**3D-to-1D Transition via Microsphere Concept** In an undeformed (virgin) matrix, polymer chains are assumed to be uniformly distributed in all spatial directions, reflecting initial isotropy.

Using the microsphere approach, we represent the 3D matrix as a superposition of many 1D elements distributed over a unit sphere. The total strain energy is computed by integrating the directional contributions over the surface of the sphere:

$$\Psi_m = \frac{1}{4\pi} \int_S \Psi_m^{\mathbf{d}} \, dS^{\mathbf{d}} \cong \sum_{i=1}^{N_d} w_i \Psi_m^{\mathbf{d}_i}, \quad \text{with} \quad \Psi_m^{\mathbf{d}_i} = \mathcal{B}^{\mathbf{d}_i}, \tag{4.1}$$

where  $N_d$  denotes the number of integration directions,  $w_i$  are the associated weights, and  $\mathcal{B}^{d_i}$  represents a team of L-agents modeling the energy in direction  $d_i$ . Each team comprises multiple sub-elements:

$$\mathcal{B}^{d_i} = \sum_{j=1}^{N_s} \mathcal{A}^i_j,\tag{4.2}$$

where  $N_s$  is the number of sub-elements per direction and  $\mathcal{A}_j^i$  is the L-agent representing a sub-element's contribution. In the virgin state, all directions are identical:  $\mathcal{B}^{d_i} = \mathcal{B}^{d_j}$ . As deformation progresses, directional differences emerge, enabling the model to naturally describe anisotropy, damage initiation, and failure propagation.

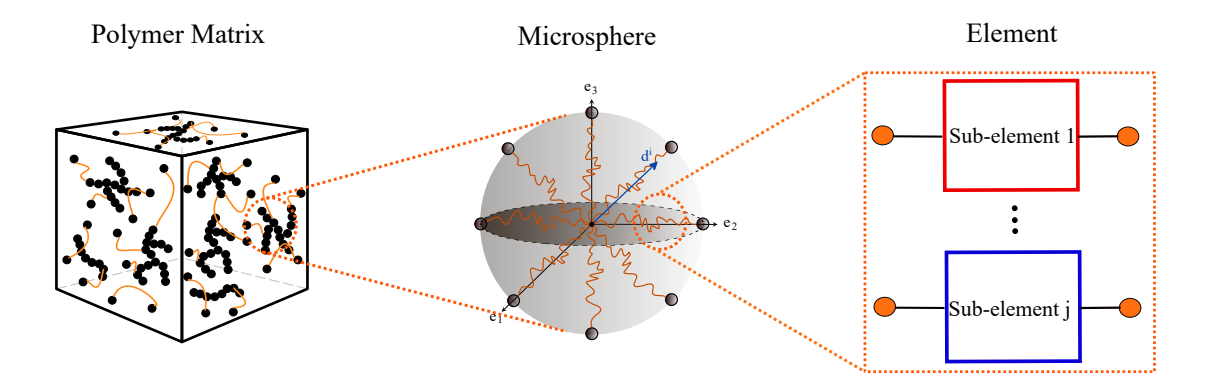


Figure 4.2: Microsphere-based 3D-to-1D transition model.

**Network Decomposition** To capture the complex behavior of each 1D element, we apply network decomposition, representing the total element response as the superposition of  $N_s$  simpler sub-element responses:

$$\Psi_m^{\boldsymbol{d}_i} = \sum_{j=1}^{N_s} \Psi_j^{\boldsymbol{d}_i}, \quad \text{where} \quad \mathcal{A}_j^i := \Psi_j^{\boldsymbol{d}_i}. \tag{4.3}$$

Combining with Eq. 4.1, the total matrix strain energy becomes:

$$\Psi_m \cong \sum_{i=1}^{N_d} \sum_{j=1}^{N_s} w_i \Psi_j^{\mathbf{d}_i} := \sum_{i=1}^{N_d} \sum_{j=1}^{N_s} w_i \mathcal{A}_j^i. \tag{4.4}$$

Each sub-element behaves as a scalar-to-scalar function and is implemented via a simplified feed-forward neural network. The resulting first Piola–Kirchhoff stress tensor is derived using the chain rule with respect to the deformation gradient:

$$\mathbf{P} = \frac{\partial \Psi_m}{\partial \mathbf{F}} - p\mathbf{F}^{-T} = \sum_{i=1}^{N_d} \sum_{j=1}^{N_s} w_i \frac{\partial \mathcal{A}_j^i}{\partial \mathbf{F}} - p\mathbf{F}^{-T},$$
(4.5)

where p is the Lagrange multiplier enforcing incompressibility.

## 4.3: Mechanical and Environmental Damages in Polymers

In general, elastomer degradation is caused by two types of stresses: mechanical, such as deformation, vibration, and relaxation, and environmental, such as thermal aging, hydrolysis, and photooxidation.

**Deformation-induced damage:** One good example of mechanical damages is the Mullins effect, where the matrix softens after the first stretch [34, 109, 120]. This phenomenon happens in filled rubber polymers, not all polymers. There are multiple sub-structural changes in the matrix that are formed due to mechanical damages, such as chain breakage in the filler interface, chain disentanglement, molecules slipping, and rupture in the cluster of fillers [13, 53], which are summarized in Fig. 4.3.

**Environmental damage** occurs mostly due to changes in the chemical micro-structure of the matrix, which occurs due to competition or collaboration of multiple sub-mechanisms. For example, thermal aging is widely considered as the competition between cross-link formation mechanism and chain scission mechanisms, where the former makes the matrix stiffer by inducing new bonds.

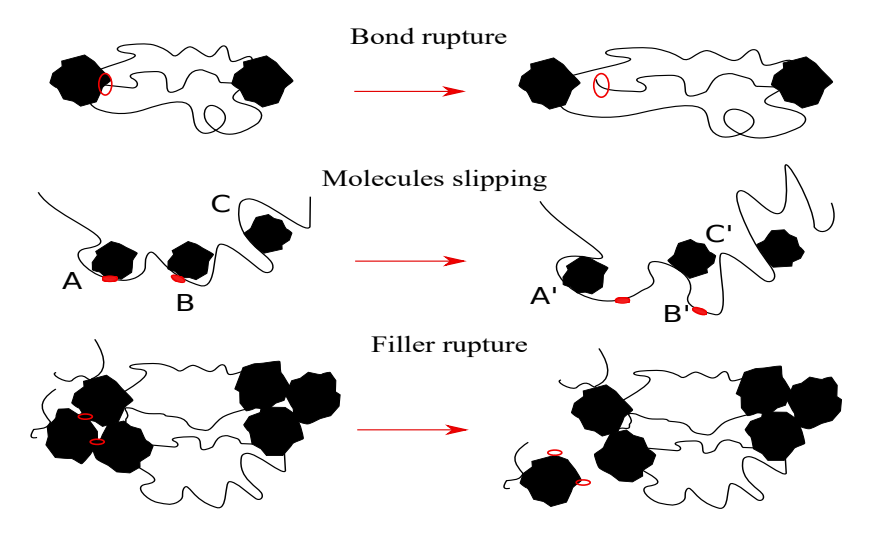


Figure 4.3: Schematic of polymer matrix change alongside with deformation-induced damage, which include breakages of chain crosslinks, chain scission, bond rupture, desorption of chains, slippage of chains, absorption of chains, and filler rupture.

In contrast, the latter makes it softer by debonding polymer chains from the system (Fig. 4.4). The rate of polymer chain scission and cross-links formation defines that the material should become brittle or ductile, although in both cases, the matrix experiences damage [86].

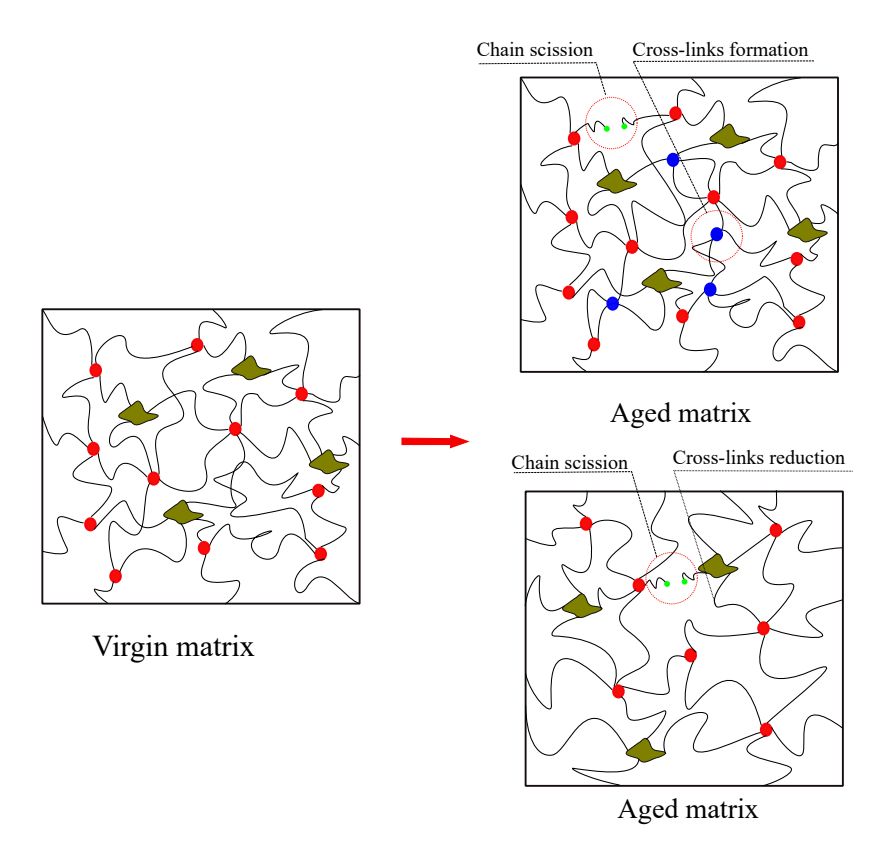


Figure 4.4: Schematic of polymer matrix change alongside with environmental-induced damage. Environmental-induced damages include chain scission, cross-links formation and reduction.

**Thermo-oxidative kinetics:** During thermo-oxidative aging, the rate of chemical oxidation can be characterized as

$$-\frac{d[P]}{dt} = k[P]^q, (4.6)$$

[P] is the chemical compound concentration of P, k is the reaction rate coefficient, and q is the reaction order. The chemical reaction governing a degradation process is commonly described using first-order kinetic equations (q=1). Furthermore, k is just a function of temperature in the presence of homogenous conditions, low stretches during aging, and no diffusion-limited oxidation. The major cause of alterations in the polymer matrix is chemical interactions between the polymer backbone and oxygen during thermal-induced aging [43,69,88].

**Networks and Subnetworks** Each network is considered to have a unique composition and describes a different energy-dissipating damage mechanism. Using the concept of micro-sphere, each

network is considered as a 3D composition of infinite 1D subnetworks that are distributed in all spatial directions. Subnetworks can only be subjected to uniaxial deformation and thus will experience different deformations based on their directions. To develop a model for the subnetwork in direction, only a simplified form of entropic energy is needed with respect to uniaxial deformation. Integrating a subnetwork in all directions, the consequent network is a representation of that concept in a 3D configuration. The similar concept will be used for training of the neural network.

As a result, network decomposition helps us describing the complex behaviour of a 1D element as the super-position of the simple behaviour of  $N_s$  sub-elements, where  $\Psi_m{}^{d_i} = \sum_{j=1}^{N_s} \Psi_j{}^{d_i}$ . Here, each sub-element is responsible for one or no inelastic behaviour. Assigning L-agent to each sub-element,  $\mathcal{A}^i_j := \Psi_j{}^{d_i}$ , an element behaviour is described by a team of cooperative L-agents  $\mathcal{B}^{d_i} = \sum_{j=1}^{N_s} \mathcal{A}^i_j$ . Consequently, by substituting Eq. 4.1, we can extract the energy of the matrix directly with regard to sub-elements and the L-agents as

$$\Psi_m = \frac{1}{4\pi} \int_S \Psi_m{}^{d} dS^{d} \cong \sum_{i=1}^{N_d} \sum_{j=1}^{N_s} w_i \psi_j{}^{d_i} := \sum_{i=1}^{N_d} \sum_{j=1}^{N_s} w_i \mathcal{A}_j^{i}. \tag{4.7}$$

Considering each sub-element is represented by an L-agent, the super-simplified scalar-to-scalar mapping behavior of a sub-element can be modeled by a simplified feed-forward neural network. Summarizing the implemented constraints, the first Piola—Kirchhoff stress tensor **P** can be derived on the basis of Eqn. 4.6 and Eqn.4.7, as

$$\mathbf{P} = \frac{\partial \Psi_m}{\partial \mathbf{F}} - p\mathbf{F}^{-T} := \sum_{i=1}^{N_d} \sum_{j=1}^{N_s} w_i \frac{\partial \mathcal{A}_j^i}{\partial \mathbf{F}} - p\mathbf{F}^{-T}, \tag{4.8}$$

where p signifies the Lagrange multiplier to ensure incompressibility of the material.

## 4.3.1: Conditional Neural Network (CondNN) L-Agent

There is a new family of hybrid machine learning algorithms known as conditional neural networks (CondNNs) for problems in which the outputs are not only dependent on past occurrences, e.g., deformation effects on the matrix, but also on external actions, e.g., temperature and time of aging

effects on the polymer matrix. This new algorithm has been derived by the combination of general neural network and decision tree concepts (see [63,110]). A routed behavior is a feature of decision trees; the data is sent to one or more children based on some learned routing function. This conditional computation means that we can infuse the knowledge in the model. Meanwhile, throughout many tasks, NNs achieve industry-leading precision for learning, but decision trees have the ability to infuse the knowledge into NNs. In other words, CondNNs are decision trees with the exception that instead of moving the data as is, each node applies a non-linear transformation to it. We can also forward the data to one or more of its children using routers.

In order to design an L-agent which can model mechanical and environmental damage in the polymer matrix, we use CondNNs as a new hybrid framework. The feed-forward L-agents consist of NNs followed by a fully connected layers, which the first branch represents the mechanical damage in the polymer matrix. The resulting features are then combined multiplicatively with the second branch of NN followed by fully connected layer that represents environmental damage in the matrix (see Fig. 4.6).

- Neural Network Architecture The architecture of the neural network (Fig. 4.6) is determined through the summary of the hyperparameters: (i) number of hidden layers,  $n_l$  (network depth), (ii) number of neurons per hidden layer,  $n_n$  (network width), (iii) activation function.

Activation function: The activation function of a node in artificial neural networks determines the output of that node given input or a set of inputs. This is similar to the linear perceptron's behavior in neural networks. However, only nonlinear activation functions allow such networks, using only a small number of nodes, to measure non-trivial problems, and such activation functions are called non-linearities. Choosing the activation function has a significant impact on the neural network's capacity and efficiency, and various activation functions can be used in different sections of the model. Based on the type of neural network architecture, the activation function used in hidden layers is usually chosen. If we are unsure which activation function to use for our network, we try and compare the results to find the best ones. We have done the same procedure in this study. Note that the choice of activation function in the hidden layer will control how well the network

model learns the training dataset. Also, the effect of choosing different activation functions has not a significant effect on training time [91].

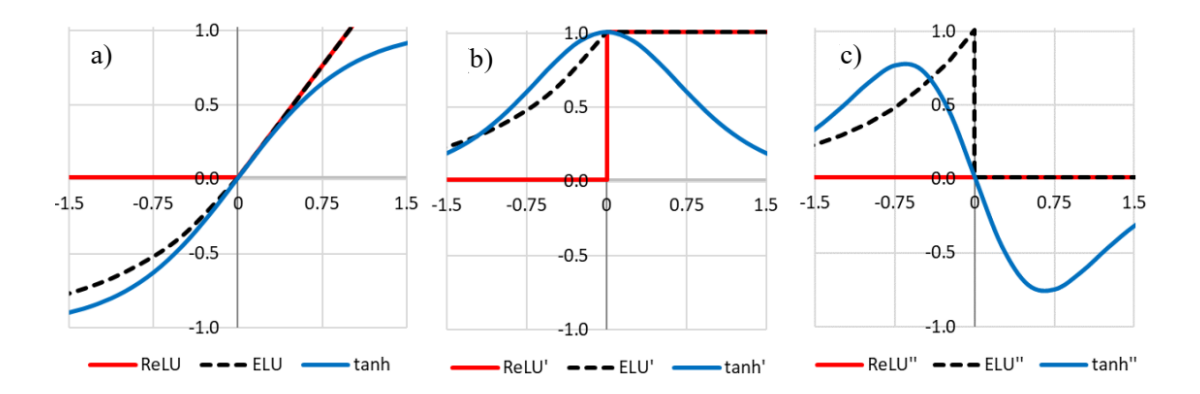


Figure 4.5: a) ReLU(Rectified Linear Unit), ELU(Exponential Linear Unit) and tanh activation functions, b) first derivatives of activation functions, and c) second derivatives of activation functions [61].

For training of the described problem, it is crucial to use activation functions tailored to the underlying physical output quantities. Using physics-based rationale, an activation function with a positive output parameter for tension and a negative output parameter for compression and non-zero derivative (which is important in physics-based neural networks) is an obvious choice. For all hidden layers, the hyperbolic tangent function is used, which is a preferable activation function due to its smoothness and non-zero derivative.

Note that Rectified Linear Unit activation function or ReLU for short is a piecewise linear function that will output the input directly if it is positive, otherwise, it will output zero. Also, The Exponential Linear Unit (ELU) is an activation function for neural networks. In contrast to ReLUs, ELUs have negative values which allows them to push mean unit activation closer to zero.

The L-agent response is computed using a feed -forward algorithm for a given set of hyperparameters  $(n_l, n_n)$ . Each L-agent can be represented by a CondNNs as

$$\mathcal{A}_{j}^{i} := \mathcal{D}^{d_{i}}(\mathbf{E}^{i})\psi_{j}^{d_{i}}(\mathbf{M}_{j}^{i}, \mathbf{S}_{j}^{i}) \qquad \mathcal{D}^{d_{i}} = CNN_{e}(\mathbf{W}_{e}, \mathbf{E}^{i}), \qquad \psi_{j}^{d_{i}} = CNN_{m}(\mathbf{W}_{m}^{j}, \mathbf{M}_{j}^{i}, \mathbf{S}_{j}^{i}), \tag{4.9}$$

where  $\psi_i^{d_i}$  represents the energy of deformation-induced damage part and  $\mathcal{D}^{d_i}$  is related to envi-

ronmental damage of one sub-element. Similarly, two weight matrices  $\mathbf{W}_{\mathbf{m}}^{j} = [W_{m_{1}}^{j}...W_{m_{n_{l}+1}}^{j}]$  and  $\mathbf{W}_{\mathbf{e}} = [W_{e_{1}}...W_{e_{n_{l+1}}}]$  are related to weight matrices of mechanical and environmental damage CondNNs, respectively. Here,  $\psi_{j}^{i}(M_{j}^{i}, S_{j}^{i})$  is trained on the basis of a non-kinematic input sets  $M_{j}^{i}$  and internal parameters  $S_{j}^{i}$  for the mechanical damage CondNN. Selection of internal parameters depend on (full or recent) material memory. Also, the input vector  $\mathbf{E}^{i}$  should represent the setting of the problem related to environmental damage such as temperature and time of degradation.

Normalization, conditions of growth, isotropy, objectivity, and poly-convexity are already satisfied in the proposed equation (Appendix).

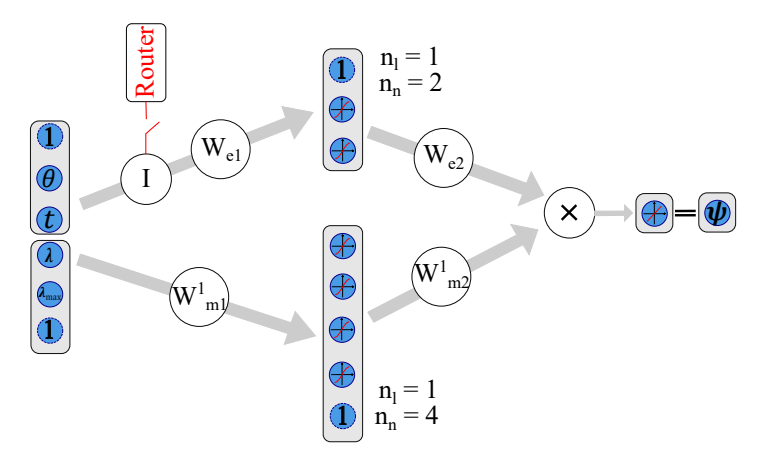


Figure 4.6: Schematic of a neural network with physics-informed engineered features to learn the effect of environmental aging on the mechanical Behaviour. This is referred to as CNN in this study.

- Model parameter identification The parameters of the CondNN model are identified using a Gradient descent algorithm. A data collection consisting of n data points is the basis for model recognition. Loss function was defined with respect to the difference between target values, AKA experimental data, and approximated value, AKA CondNN output. Here, we define the loss function  $\mathcal{L}$  Mean Squared Error (MSE) for a total of  $n_{tot}$  data points as

$$\mathcal{L}(\mathbf{W_m^1}, ...., \mathbf{W_m^j}, \mathbf{W_e}) = \frac{1}{2} \sum_{n=1}^{n_{tot}} \left[ \mathbf{g}_1 \left( \sum_{i=1}^{N_d} \sum_{j=1}^{N_s} w_i \frac{\partial \mathcal{A}_j^i}{\partial \mathbf{F}} - p \mathbf{F}^{-T} \right) \mathbf{g}_1 - P_n^{11} \right]^2, \tag{4.10}$$

where  $P_n^{11} := \mathbf{g}_1 \mathbf{P} \mathbf{g}_1$  is the first component of the experimental macro-scale stress tensor  $\mathbf{P}_n$  in loading direction  $\mathbf{g}_1$  for point n.

# 4.4: Validation: Environmental + Mechanical Damages in Rubber

Here, the proposed hybrid model is developed and validated for two different loading scenarios

- 1. Thermal-induced aging + Mechanical deformation (Mullins effect)
- 2. Hydrolysis (desalinated water) + Mechanical deformation (Mullins effect)

In both cases, the model was benchmarked against experimental data to predict the inelastic behavior of cross-linked elastomers for different states of deformation at different stages of aging. We also validated the model predictions for different coupling scenarios for mechanical and environmental damages, namely

- **Intermittent test** where the sample has been aged first with no stress, and then the mechanical behaviour is characterized
- **-Relaxation test** where the samples were loaded and aged at constant deformation and the drop in the stress has been recorded.

In both cases, the predictions were validated against four main variables the effect of (i) deformation, (ii) deformation history, (iii) aging time (t), and (iv) aging temperature ( $\theta$ ).

#### 4.4.1: Network Architecture

Wwe used identical engines; a relatively simple engine built by  $N_d=21$  teams, where each team had  $N_s=2$  agents [38]. Note that the number of teams and their related agents can be chosen based on the trade-off between accuracy and computational cost. In other words, we consider 21 teams because it is a small number for estimation of the integral with a summation. As a result, it guarantees that the proposed model error in prediction is excellent even in a small number of teams. To capture all deformation states, we used only two agents, each of which is representative of the first and second invariants of the Green-Cauchy deformation tensor. For the CondNNs structure of L-agents, we considered one input layer, one hidden layer with four neurons and three activation functions soft plus  $\psi(\bullet) = ln(1 + e^{\bullet})$ , sinusoid  $\psi(\bullet) = sin(\bullet)$  and hyperbolic tangent  $\psi(\bullet) = ln(1 + e^{\bullet})$ 

 $tanh(\bullet)$ .

The internal parameters of L-agents were built via  $\lambda_{j-max}$  parameters to capture the deformation of the rubbers with full memory. In order to allow teams to predict various deformation states, the first and second deformation invariants were supplied to each team [30, 74]. The condition was satisfied by providing input sets into the first and second L-agents as

$$\mathbf{M}_{1}^{d_{i}} = [\lambda^{d_{i}}], \quad \mathbf{S}_{1}^{d_{i}} = [\lambda^{d_{i}}_{max}], \quad \mathbf{E}^{d_{i}} = [t, \theta], \quad \mathbf{M}_{2}^{d_{i}} = [\nu^{d_{i}}], \quad \mathbf{S}_{2}^{d_{i}} = [\nu^{d_{i}}_{max}], \quad \mathbf{E}^{d_{i}} = [t, \theta], \quad (4.11)$$

while

$$\lambda^{d_i} = \sqrt{d_i C d_i}, \qquad \nu^{d_i} = \sqrt{d_i C^{-1} d_i}, \qquad C = \mathbf{F}^T \mathbf{F},$$
 (4.12)

where  $[\mathbf{d}_i]_{i=1...N_d}$  is integration directions in micro-sphere,  $\lambda^{\mathbf{d}_i}$  and  $\nu^{\mathbf{d}_i}$  are related to  $I_1$  and  $I_2$ , as the first and second invariants of  $\mathbb{C}$ , respectively.

In summary, the rubber matrix was represented by a cooperative game of 21 teams of 2 agents through  $\mathcal{A}_{j}^{i}$ ,  $i \in \{1,21\}$ ,  $j \in \{1,2\}$ . After agent fusion, the final cost function is given by

$$\mathcal{L}(\mathbf{W}_m^1, \mathbf{W}_m^2, \mathbf{W}_e) = \frac{1}{2} \sum_{n=1}^{\infty} [\mathbf{g}_1(\sum_{i=1}^{21} \sum_{j=1}^{2} w_i \frac{\partial \mathcal{A}_j^i}{\partial \lambda_j^{d_i}} \frac{\partial \lambda_j^{d_i}}{\partial \mathbf{F}} - p\mathbf{F}^{-T})\mathbf{g}_1 - P_n^{11}]^2, \tag{4.13}$$

subjected to weights related to  $\lambda_{max}$  and  $\nu_{max} \leq 0$ , and weights related to  $\lambda$  and  $\nu \geq 0$  to satisfy thermodynamic consistency and poly-convexity, respectively. Accordingly, the energy of each sub-element can be written with respect to the deformation gradient  $\mathbf{F}$  as follows

$$\sum_{i=1}^{21} w_i \frac{\partial \mathcal{A}_1^i}{\partial \lambda^{d_i}} \frac{\partial \lambda^{d_i}}{\partial \mathbf{F}} = \sum_{i=1}^{21} w_i \frac{\partial \mathcal{A}_1^i}{\partial \lambda^{d_i}} \frac{1}{\lambda^{d_i}} \mathbf{F} \left( \mathbf{d}_i \otimes \mathbf{d}_i \right), \tag{4.14}$$

$$\sum_{i=1}^{21} w_i \frac{\partial \mathcal{A}_2^i}{\partial \nu^{\mathbf{d}_i}} \frac{\partial \nu^{\mathbf{d}_i}}{\partial \mathbf{F}} = -\sum_{i=1}^{21} w_i \frac{\partial \mathcal{A}_2^i}{\partial \nu^{\mathbf{d}_i}} \frac{1}{\nu^{\mathbf{d}_i}} \mathbf{F}^{-1} \mathbf{F}^{-T} \mathbf{F}^{-1} (\mathbf{d}_i \otimes \mathbf{d}_i). \tag{4.15}$$

## 4.4.2: Step 1: CondNN Training in the absence of aging

To investigate the performance of the proposed model in the material in the absence of aging, we

benchmarked the inelastic features in the behavior of natural rubber, namely Mullins effect and permanent set. Figure 4.7 shows stress-stretch curves for this cross-linked polymer with experimental data of [80]. We used one set of bi-axial loading-unloading until  $\lambda=2.7$  for training and predicting inelastic effects in different states of deformation, e.g., uniaxial and pure shear at increasing stretch amplitudes which constitutes deformation histories.

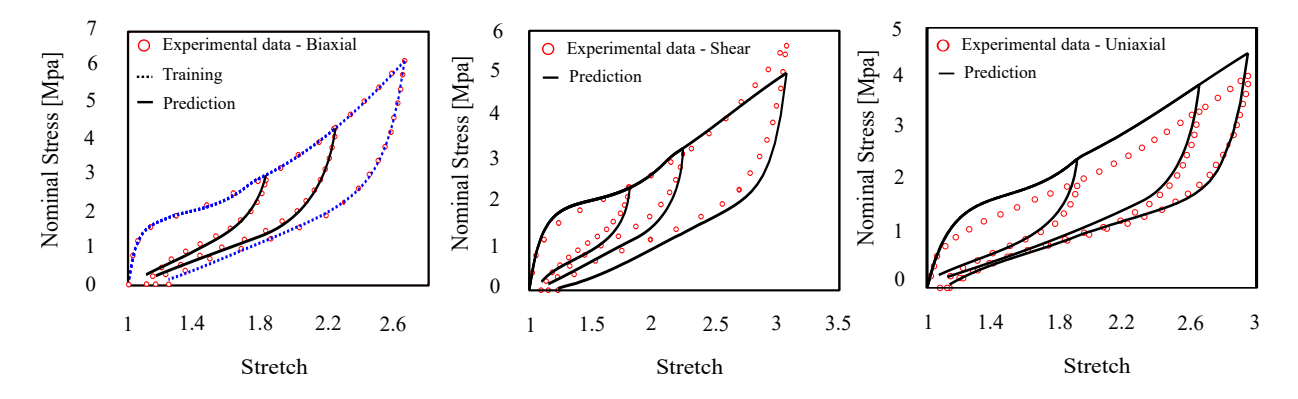


Figure 4.7: Model training and prediction of bi-axial, pure shear, and uni-axial(Urayama's dataset [80]). Dash lines stand for fitting and solid lines stand for prediction. The biaxial dataset which have been showed with the blue line used for training and of the model. The black lines in bi-axial, shear, and uni-axial datasets show the performance of the model in prediction after training.

#### 4.4.3: Case Study: Thermo-Oxidation + Mechanical Damage

**Polyurethane** A bone form punch was used to punch dumbbell samples in compliance with ASTM D412 standards. The reason that we are using dog-bone samples is that in this shape, when we put the extensometer in a specific location of that sample, we are sure that it gives us one component of the deformation matrix, for example, x-x direction. But in complex shapes, several components of stress tensor participate; so, it is not possible to see the effect of each component with an external extensometer. Three different temperatures,  $60^{\circ}C$ ,  $80^{\circ}C$ , and  $95^{\circ}C$ , in zero humidity level, were used to age the samples. The performance of the invented model was determined using the results of the uni-axial tensile failure tests. Fig. 4.8 depicts the evaluation's related findings.

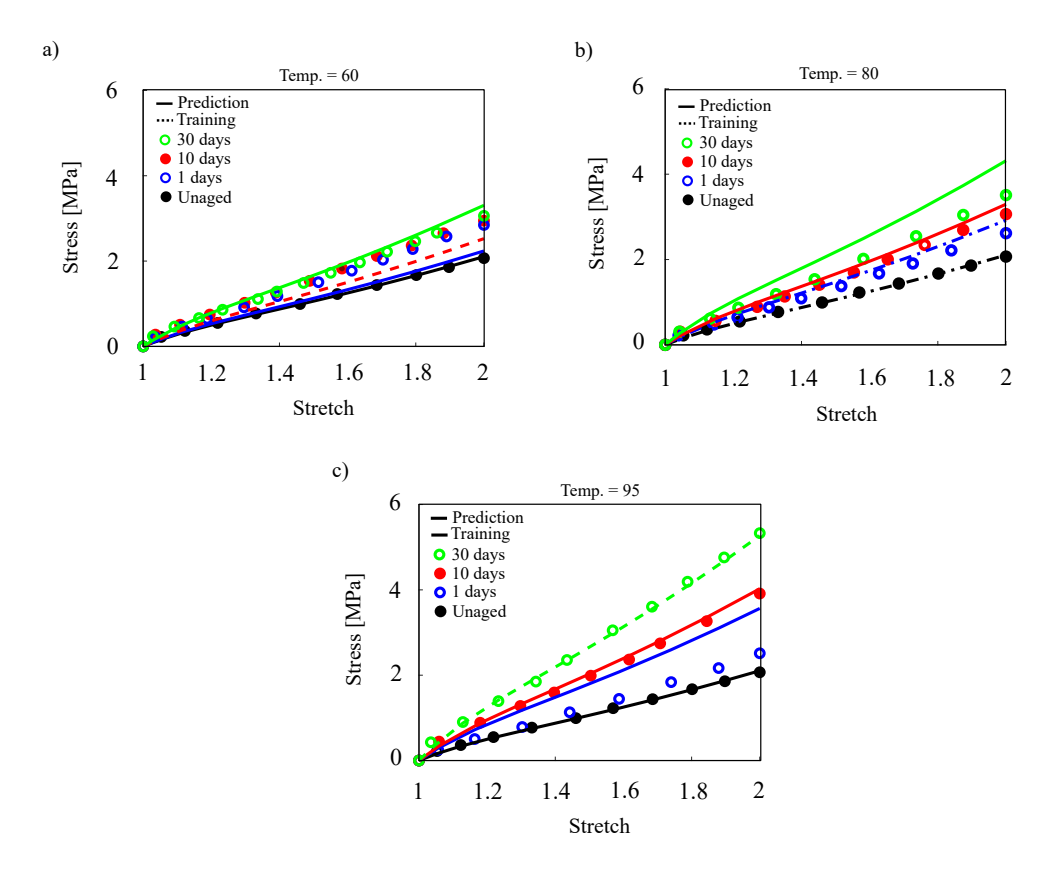


Figure 4.8: Training and model predictions for polyurethane against intermittent test; (a) at  $60^{\circ}C$ , (b) at  $80^{\circ}C$ , (c) at  $95^{\circ}C$ . Dash lines stand for fitting and solid lines stand for prediction. The black (unaged) and red points in the Fig. a), the black (unaged) and blue points in Fig. b), and the black (unaged) and green points in the Fig. c) have been used for training. The solid lines show the performance of model in prediction after the training.

**Silicon Adhesive** To assess the model's capabilities, we compared its predictions to our experimental results, which were specifically developed to demonstrate the effect of chemical aging on the constitutive response of silicone adhesive. In this case, samples were placed in ovens at temperatures  $60^{\circ}C$ ,  $80^{\circ}C$ , and  $100^{\circ}C$  with a relative humidity of zero (i.e. RH= 0%). All of the specimens were aged under constant pressure, and after a set amount of time, they were removed from the containers and dried with tissue paper. The predictions of the proposed model against the experimental data for different types of aging and different amount of aging times, temperatures, and deformations are plotted in figure 4.9.

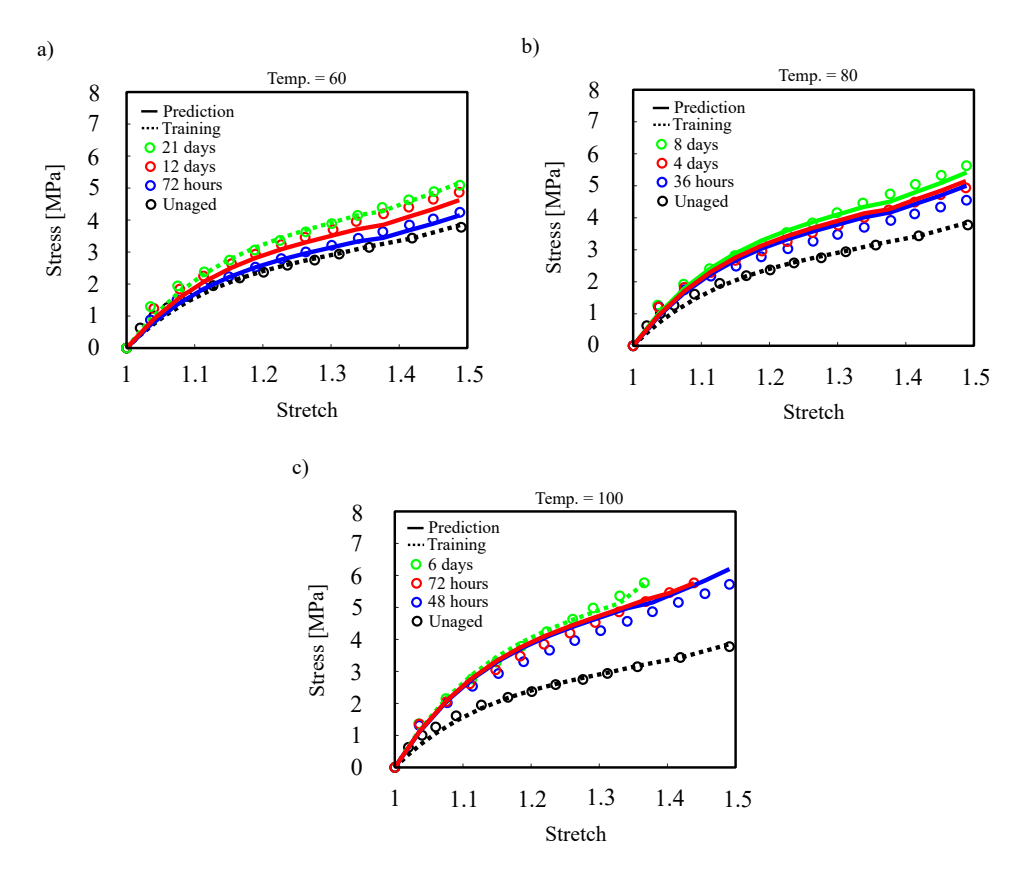


Figure 4.9: Training and model predictions for silicone adhesive against intermittent test; (a) at  $60^{\circ}C$ , (b) at  $80^{\circ}C$ , (c) at  $100^{\circ}C$ . Dash lines stand for fitting and solid lines stand for prediction. The black(unaged) and green points in the figure a), the black(unaged) points in figure b), and the black(unaged) and green points in the figure c) have been used for training. The solid lines show the performance of model in prediction after the training.

Note that the model is able to predict the behavior of elastomers even in the stretch greater than 4. Thermo-oxidative aging makes the samples brittle. As a result, the failure point for samples happens on the less stretch. So, because the focus of the proposed model is on the behavior of aged materials we showed the performance of the model till stretch less than 4. In addition, the kernel of model is the same even for higher stretches. So, the model works for higher stretch as well.

## 4.5: Conclusion

The aim of this chapter was to propose a novel physics-informed hybrid framework to capture the relation between elastomeric network mechanics and environmental damage. The proposed model is used to describe the effect of single-mechanism aging, such as thermal-induced or hydrolytic

aging, on the behavior of the material in this hybrid system. Huge chain scission, cross-link reduction, chain formations, and changes in polymer morphology are all examples of environmental single-mechanism damages that alter the polymer matrix over time. In other words, this model is a predictive model and not a descriptive model. As a result, it can provide prediction in a fraction of time and cost to the end-users for the reliable design of components. Although, The model cannot be used to understand or explore kinetics. By extracting micro-structural activity from macroscopic experimental data, the data-driven approach aims to overcome the shortcomings of both phenomenological and micro-mechanical models.

The model arises from polymer physics and an order reduction strategy ending to the constrained L-agents training. The polymer matrix was described by a cooperative multi-agents system, in which each agent is represented by a simple deep-learned CondNN that is super-constrained by laws derived from physics, thermodynamics, and continuum mechanics. While satisfying the continuum mechanics and thermodynamics rules, the proposed hybrid model is quite simple for the most rubbery media in the extreme environment.

The excellent performance of the proposed method was proven by validating against different experimental data on different materials that are particularly selected to reveal the evolution of inelastic behaviour during single mechanism agings. The efficiency of the model was found satisfactory, and in some cases, excellent when compared with the experimental data. "In general, the error of our model in training and prediction is less than 10%." Accuracy and simplicity of the model make it a proper choice for commercial and industrial application because we do not need to know the exact behavior and interaction of micro-structures; however, in the future, the model can be extended to consider viscoelasticity and non-isotropic formation for better precision due to platform of the model. Besides, note that the proposed model focus is on the mechanical behavior of the material during degradation, not lifetime prediction. Also, the performance of the proposed model is completely dependent on the dataset that we choose for training. It is axiomatic that if we increase the available dataset for training, the predictionability of the model is more accurate.

# **CHAPTER 5: FINITE ELEMENT**

# **ANALYSIS**

#### 5.1: Introduction

The study of polymer mechanics focuses on the relationship between the mechanical response of polymers and externally applied forces. This field plays a crucial role in the design, optimization, and prediction of the mechanical performance of polymer-based components used in a broad range of engineering applications.

Historically, polymers were considered inexpensive materials with limited structural applications. However, advances in theoretical modeling and experimental techniques have repositioned polymers as high-performance, reliable, and tunable materials. These developments, coupled with a better understanding of polymer behavior under different loading and environmental conditions, have expanded their role in critical engineering systems.

Traditional mechanical analysis techniques such as closed-form solutions were largely limited to simple geometries and loading scenarios. With the advent of modern computational tools, the Finite Element Method (FEM) has become the predominant technique for simulating and analyzing the mechanical behavior of polymers. The widespread availability of commercial FEM software packages has made it possible to solve complex geometries with nonlinear material behavior. Nevertheless, the use of such tools demands careful modeling assumptions, validation, and physical insight to avoid erroneous results.

This chapter provides a comprehensive overview of finite element modeling strategies for polymeric materials, emphasizing nonlinear formulation, hyperelastic constitutive models, and consistent tangent stiffness derivation for robust computational implementation.

Analysis Method	Strengths	Limitations
Linear Elasticity	Computationally efficient; provides analytical insight into basic deformation	Inadequate for complex geometries, nonlinearities, or time-dependent behavior
FE with Basic Material Model	Captures nonlinear geometries; straightforward implementation	Poor predictive accuracy for large strain or rate-sensitive effects
FE with Advanced Material Model	Captures nonlinear geometry and material responses with higher accuracy	Requires extensive calibration and high computational cost

Table 5.1: Comparison of common analysis methods for polymer mechanics.

# 5.2: Nonlinear Equilibrium and Directional Derivatives

The governing equations in finite deformation mechanics typically take the form of a nonlinear boundary value problem. To solve these equations numerically, iterative approaches such as the Newton-Raphson method are used. Central to this approach is the concept of the directional derivative, which enables the linearization of nonlinear equations.

## **5.2.1:** Concept of Directional Derivative

Consider a two-spring system with total potential energy defined as

$$\Pi(\mathbf{x}) = \frac{1}{2}kx_1^2 + \frac{1}{2}k(x_2 - x_1)^2 - Fx_2,$$
(5.1)

where  $\mathbf{x} = [x_1 \ x_2]^T$  and F is the applied load. For a small displacement increment  $\mathbf{u} = [u_1 \ u_2]^T$ , the change in potential energy can be approximated by the directional derivative:

$$D\Pi(\mathbf{x})[\mathbf{u}] \approx \Pi(\mathbf{x} + \mathbf{u}) - \Pi(\mathbf{x}). \tag{5.2}$$

Using Taylor expansion, the directional derivative becomes:

$$D\Pi(\mathbf{x})[\mathbf{u}] = \frac{d}{d\epsilon} \Big|_{\epsilon=0} \Pi(\mathbf{x} + \epsilon \mathbf{u}) = \mathbf{u}^T (\mathbf{K}\mathbf{x} - \mathbf{F}),$$
 (5.3)

where the stiffness matrix is given by:

$$\mathbf{K} = \begin{bmatrix} 2k & -k \\ -k & k \end{bmatrix}. \tag{5.4}$$

Setting  $D\Pi = 0$  for all admissible **u** leads to the equilibrium condition:

$$\mathbf{K}\mathbf{x} = \mathbf{F}.\tag{5.5}$$

## 5.3: Newton-Raphson Linearization

To solve a general nonlinear system  $\mathbf{R}(\mathbf{x}) = 0$ , the Newton-Raphson method approximates the residual at each iteration using a first-order Taylor expansion:

$$\mathbf{R}(\mathbf{x}_{k+1}) \approx \mathbf{R}(\mathbf{x}_k) + \mathbf{K}(\mathbf{x}_k)\mathbf{u} = 0, \tag{5.6}$$

$$\Rightarrow \mathbf{K}(\mathbf{x}_k)\mathbf{u} = -\mathbf{R}(\mathbf{x}_k), \quad \mathbf{x}_{k+1} = \mathbf{x}_k + \mathbf{u}. \tag{5.7}$$

Here, **K** is the tangent stiffness matrix:

$$K_{ij} = \frac{\partial R_i}{\partial x_j}. (5.8)$$

# 5.4: Tangent Stiffness Matrix in Finite Element Analysis

For a typical finite element, the tangent stiffness matrix is assembled from element-level contributions:

$$\mathbf{K}^{(e)} = D\mathbf{T}^{(e)}(\mathbf{x})[\mathbf{u}] = \begin{bmatrix} \mathbf{K}_{aa} & \mathbf{K}_{ab} \\ \mathbf{K}_{ba} & \mathbf{K}_{bb} \end{bmatrix},$$
(5.9)

where  $T^{(e)}$  is the internal force vector, and u is the displacement increment.

# **5.5: Hyperelastic Constitutive Models**

In hyperelastic materials, stress is derived from a strain energy density function  $\Psi(\mathbf{F})$  that depends on the deformation gradient  $\mathbf{F}$ :

$$\mathbf{P} = \frac{\partial \Psi}{\partial \mathbf{F}}.\tag{5.10}$$

For incompressible materials, the constraint  $\det \mathbf{F} = 1$  introduces a Lagrange multiplier p, leading to:

$$\mathbf{P} = -p\mathbf{F}^{-T} + \frac{\partial \Psi}{\partial \mathbf{F}}.$$
 (5.11)

The second Piola-Kirchhoff stress S then becomes:

$$\mathbf{S} = -p\mathbf{C}^{-1} + 2\frac{\partial \Psi}{\partial \mathbf{C}}.\tag{5.12}$$

## 5.6: Elasticity Tensors

To linearize constitutive models in Newton-based solvers, one defines the elasticity tensor  $\mathbb{C}$ :

$$d\mathbf{S} = \mathbb{C} : d\mathbf{E}, \quad \mathbb{C} = 4 \frac{\partial^2 \Psi}{\partial \mathbf{C} \partial \mathbf{C}}.$$
 (5.13)

# 5.7: Isotropic Hyperelasticity

For isotropic materials, the strain energy depends only on the invariants of C:

$$\Psi = \Psi(I_{\mathbf{C}}, II_{\mathbf{C}}, III_{\mathbf{C}}), \tag{5.14}$$

$$\mathbf{S} = 2\Psi_I \mathbf{I} + 4\Psi_{II} \mathbf{C} + 2J^2 \Psi_{III} \mathbf{C}^{-1}, \tag{5.15}$$

where  $\Psi_I = \partial \Psi / \partial I_{\mathbf{C}}$ , and so on.

# 5.8: Spatial Form of Stress Tensor

The Cauchy stress tensor is recovered via:

$$\sigma = \frac{1}{J} \mathbf{F} \mathbf{S} \mathbf{F}^T. \tag{5.16}$$

Alternatively, using spatial derivatives of  $\Psi(\mathbf{b})$ , one may compute:

$$\sigma = 2J^{-1} \frac{\partial \Psi}{\partial \mathbf{b}} \mathbf{b}. \tag{5.17}$$

# 5.9: Incompressible Hyperelasticity

In incompressible cases, the strain energy formulation becomes:

$$\Psi = \Psi(\mathbf{F}) - p(J-1), \tag{5.18}$$

and the constitutive relation for **S** must satisfy the incompressibility condition. Using the consistency condition on allowable strain rates, the general form becomes:

$$\mathbf{S} = 2\frac{\partial \Psi}{\partial \mathbf{C}} + \gamma J \mathbf{C}^{-1},\tag{5.19}$$

where  $\gamma$  is related to hydrostatic pressure p by:

$$p = \gamma + \frac{2}{3}J^{-1}\frac{\partial\Psi}{\partial\mathbf{C}}:\mathbf{C}.$$
 (5.20)

# 5.10: Finite Element Implementation Using UMAT

The Finite Element Method (FEM) enables the integration of custom material models using userdefined subroutines. In Abaqus, the UMAT interface (User MATerial) allows users to implement constitutive laws written in Fortran, facilitating advanced material behavior beyond the built-in options.

#### 5.10.1: Role of UMAT in Nonlinear Finite Element Analysis

For finite deformation problems, accurate stress integration and consistent tangent stiffness are essential for the convergence of Newton-Raphson iterations. The UMAT must return two key outputs at each integration point:

- The second Piola-Kirchhoff stress tensor S.
- The algorithmic tangent modulus tensor  $\mathbb{C} = \frac{\partial \mathbf{S}}{\partial \mathbf{E}}$ .

The input and output quantities are typically defined in the material (Lagrangian) configuration, consistent with the total Lagrangian finite element formulation.

#### **5.10.2: Inputs and Outputs of UMAT**

The inputs passed to UMAT by the FEM solver include:

- Current deformation gradient F.
- Strain increment  $\Delta E$ .
- State variables (internal variables).
- Temperature, time increment  $\Delta t$ , and material constants.

The subroutine must compute:

- Updated stress tensor **S**.
- Updated internal state variables.
- Consistent tangent modulus  $\mathbb{C}$  for global system assembly.

#### **5.10.3:** Constitutive Consistency in UMAT

The stress update in hyperelasticity is typically defined as:

$$\mathbf{S} = -p\mathbf{C}^{-1} + 2\frac{\partial \Psi}{\partial \mathbf{C}},\tag{5.21}$$

where  $\mathbf{C} = \mathbf{F}^T \mathbf{F}$  is the right Cauchy-Green deformation tensor, and  $\Psi$  is the strain energy density function.

The consistent tangent modulus is computed as:

$$\mathbb{C} = 4 \frac{\partial^2 \Psi}{\partial \mathbf{C} \partial \mathbf{C}},\tag{5.22}$$

ensuring that the linearization of the residual vector  $\mathbf{R}(\mathbf{x})$  matches the expected directional derivative:

$$D\mathbf{R}(\mathbf{x})[\mathbf{u}] = \mathbb{C} : \delta \mathbf{E}. \tag{5.23}$$

This guarantees quadratic convergence in Newton-Raphson iterations.

#### **5.10.4: Benefits of Using UMAT**

Feature	Advantages	
Custom Constitutive Modeling	Implementation of rate-dependence, damage, aging, or experimental formulations	
Direct FEM Coupling	Allows stress updates and tangent moduli to be synchronized with global solvers	
Research Flexibility	Enables prototyping of novel theoretical models for polymers and composites	
Robustness	Improves convergence for complex nonlinear problems with large deformations	

Table 5.2: Advantages of implementing material models via UMAT.

## 5.10.5: Practical Considerations for UMAT Development

Developing a reliable UMAT routine requires:

- Rigorous derivation of the stress and tangent modulus consistent with the strain energy function.
- Verification against standard benchmarks: uniaxial, biaxial, and shear tests.
- Careful treatment of incompressibility, internal variables, and numerical stability.

Neglecting the consistent tangent modulus or implementing an inconsistent formulation can lead to poor convergence behavior, especially for nearly incompressible or large-strain materials.

# **5.11: Summary**

This chapter introduced the nonlinear finite element formulation for polymer mechanics, covering the derivation of the directional derivative, Newton-Raphson linearization, tangent stiffness matrices, and hyperelastic constitutive laws. The mathematical foundations established here are essential for implementing robust user-defined material models (UMATs) and for the accurate simulation of polymeric behavior under large deformations. The integration of user-defined constitutive models via the UMAT subroutine extends the versatility of finite element solvers, allowing for more accurate and physically motivated simulations, especially when dealing with complex phenomena such as environmental degradation, aging, and damage evolution in polymers. When combined with rigorous continuum theory and consistent linearization strategies, the UMAT interface serves as a powerful bridge between advanced material model and commercial software.

# **CHAPTER 6: INERT THERMAL AGING**

#### 6.1: Abstract

This study presents a micro-mechanical model developed to investigate the effects of thermal aging—excluding oxidative influences—on the constitutive behavior of cross-linked polymeric systems, with a focus on elastomers. The model accounts for the simultaneous and competing processes of chain scission and cross-linking that occur during aging. Although both mechanisms are active, one typically dominates, leading to distinct changes in material properties. The cross-link density may increase or decrease depending on the reaction kinetics, which are governed by temperature and exposure duration.

The goal of this modeling effort is to develop a mechanistic understanding of how thermal aging influences the mechanical response of cross-linked polymers and to integrate this understanding into a computational framework. By explicitly capturing the interplay between chain scission and cross-linking, the model enables accurate prediction of the evolution of material properties over time. To facilitate practical application, the constitutive model is linearized for implementation within a finite element method (FEM) framework. This includes derivation of the consistent tangent modulus to ensure numerical stability and convergence during nonlinear simulations. The resulting model has been implemented in a FEM environment, allowing for simulation of thermally aged polymer behavior in complex geometries and loading conditions relevant to engineering applications.

By isolating inert thermal aging from oxidative effects, this work sheds light on fundamental aging mechanisms specific to elastomers. The insights gained have practical implications for material development and can inform improved design practices in applications where elastomeric durability is critical.

## **6.2: Introduction**

The space environment poses a complex set of challenges for material systems, characterized by extreme vacuum, temperature fluctuations, radiation, plasma, and microgravity. Polymers exposed to such conditions inevitably undergo aging and degradation, leading to progressive deterioration of their mechanical, physical, and chemical properties. Over time, these changes compromise material functionality, making durability and environmental resistance essential for polymeric components in space applications.

This chapter introduces the harsh conditions encountered in space and their implications for the long-term performance of polymeric materials, with a focus on adhesives and elastomers. Key degradation mechanisms—such as thermal cycling, mechanical stress, electromagnetic radiation, and ionizing particles—are reviewed in the context of their influence on the structural and functional integrity of polymers. This background provides a foundation for material selection, performance prediction, and reliability assessment in space systems.

Materials used in space must withstand unique stressors including thermal cycling, high vacuum, atomic oxygen, radiation, micrometeoroids, and debris impacts ([18]). Elastomeric materials, in particular, are susceptible to aging from various environmental influences such as heat, humidity, radiation, and chemical exposure ([114]; [23]). Among these, thermal aging—caused by prolonged exposure to elevated temperatures—is recognized as one of the most significant contributors to long-term degradation.

Extensive prior research has examined thermal aging in rubbers and cross-linked polymers. The resulting changes in network structure are influenced by factors such as monomer composition, initial curing systems ([22]), and aging conditions ([93]). Moreover, the mechanical loading state during aging has been shown to significantly affect material response ([84]; [97]). Additional investigations have addressed aging-induced cross-linking, chain scission, and accelerated degradation mechanisms ([105]; [76]; [12]).

A series of works ([45]; [46]; [66]; [65]; [64]) have modeled the thermo-oxidative behavior

of polymers by incorporating diffusion-reaction processes and mechanical coupling into thermodynamically consistent frameworks. These models account for the evolution of internal variables, such as the formation or degradation of cross-links and chain scission events, highlighting the complex interplay between chemical and mechanical factors in aging ([68]; [87]).

An alternative approach to understanding aging mechanisms is through monitoring molecular weight changes and distributions throughout degradation ([73]). Under inert thermal conditions, degradation can involve cross-reactions between macromolecules and low-molecular-weight species, potentially enhancing or diminishing thermal stability depending on the reactivity of intermediates.

Thermal aging induces microstructural transformations in polymers. For instance, high temperatures can cause chain scission, leading to the coexistence of soft and hard phases within the polymer matrix ([1]; [104]). These changes manifest as modifications in chemical composition, chain conformation, molecular weight, cross-link density, and the behavior of functional groups. The following aspects are particularly affected:

- Chemical Composition: New species may form, altering the polymer's chemistry.
- Chain Conformation: Spatial arrangements of polymer chains shift under heat.
- Molecular Weight and Distribution: Chain scission leads to shorter chains and broader distributions.
- Cross-Linking and Branching: Additional cross-links or branched structures may form.
- Functional Groups: Their reactivity and distribution may change with temperature.

Cross-linked polymers generally exhibit improved thermal stability due to the need for multiple bond breakages for degradation to occur ([98]).

The goal of this research is to develop a predictive micro-mechanical model capable of estimating the inelastic behavior of cross-linked polymers subjected to thermal aging. The model assumes homogeneous aging—an appropriate condition for ultra-thin samples aged in oxygen-free environments—allowing a focused investigation into the aging phenomena specific to inert thermal degradation.

# 6.3: Mechanical and Experimental Damages in Polymers

Cross-linked elastomers result from the extensive interconnection of polymer macromolecules within a limited volume. Typically, the deterioration of elastomers can be linked to two primary categories of forces: mechanical stresses like deformation, vibration, and relaxation, and deterioration stemming from diverse environmental factors, including elevated temperatures, immersion in water, and exposure to ultraviolet (UV) radiation.

#### **6.3.1: Deformation-Indeced Damage:**

Material deformation frequently arises as an outcome of various mechanical stresses. These stresses can induce several sub-structural alterations within the matrix, encompassing phenomena like chain breakage, molecular displacement, and filler ruptures. These effects can be consolidated as follows: Fig. 6.1.

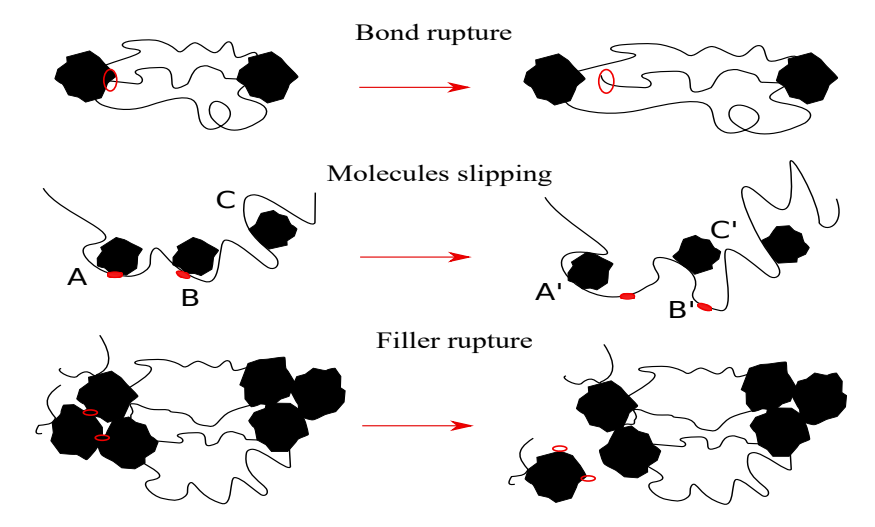


Figure 6.1: Schematic of polymer matrix change alongside with deformation-induced damage, which include breakages of chain crosslinks, chain scission, bond rupture, desorption of chains, slippage of chains, absorption of chains, and filler rupture.

## **6.3.2: Environmental Damage:**

This type of damage primarily stems from alterations in the chemical microstructure of the matrix. It can manifest as a result of the interplay between multiple sub-mechanisms, such as chain scission and cross-linking, either in competition or collaboration. (see Fig.6.2). The relationship between

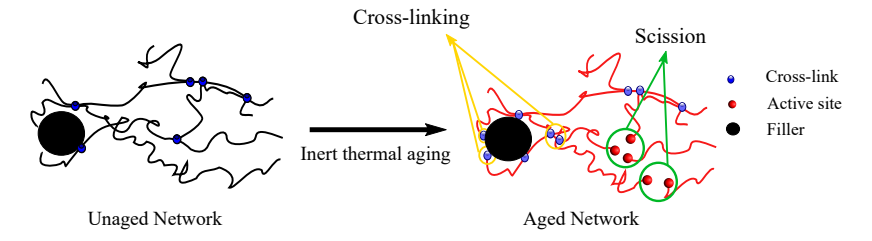


Figure 6.2: Schematic of chain scission and cross-linking processes.

tensile strength and crosslink density, before and after aging, is presented in Fig.6.3. The data reveal a distinct peak in the tensile strength of NBR samples as crosslink density increases. This trend can be attributed to two competing effects. Initially, increasing the crosslink density enhances the number of junction points within the rubber network, which improves the uniform distribution of applied stress and leads to higher tensile strength. However, beyond a certain threshold, further crosslinking reduces the average molecular weight between crosslink points, resulting in stiffer chain segments and the development of localized stress concentrations. This structural rigidity ultimately diminishes the material's ability to deform, causing a decline in tensile strength.

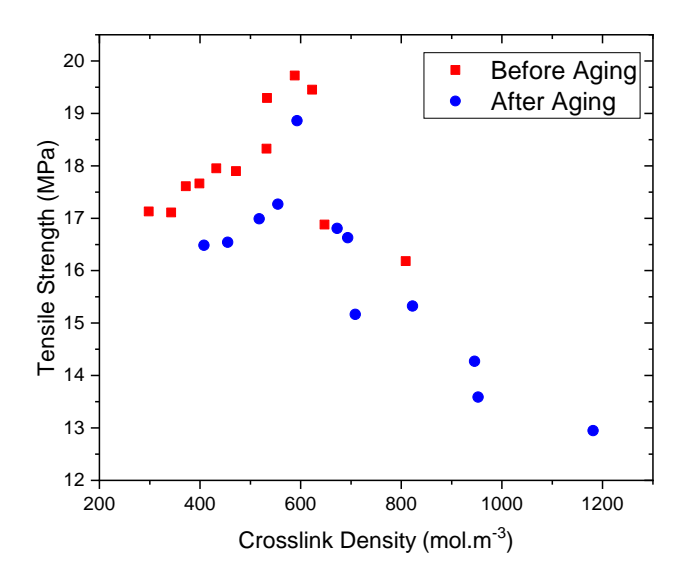


Figure 6.3: Tensile strength vs. Crosslink density of NBR vulcanizates before and after thermal aging [54].

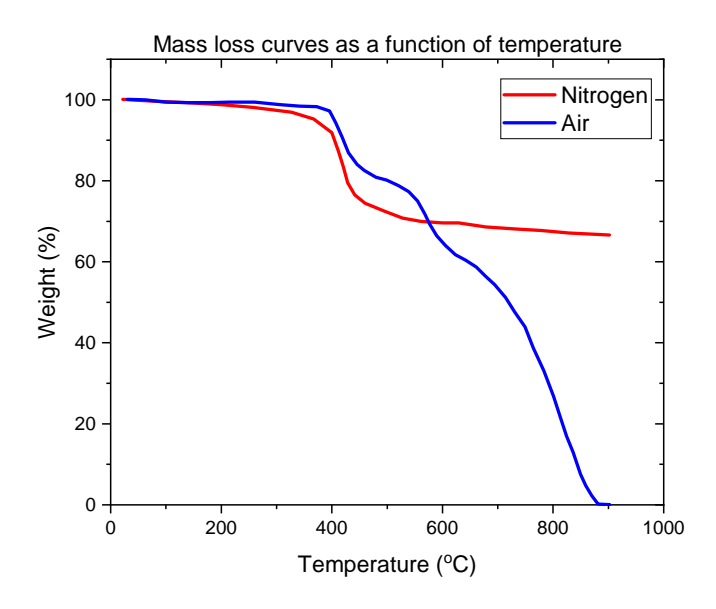


Figure 6.4: Mass loss curves as a function of temperature via TGA under inert and oxidative environment [70].

# 6.4: Thermal Aging Mechanisms and Experimental Observations

# 6.4.1: Competing Mechanisms: Chain Scission vs. Crosslinking

A marginal increase in material hardness during aging presents an interpretive challenge: it is often unclear whether this change stems from a subtle increase in crosslink density or from the simultaneous occurrence of both chain scission and crosslinking. In this study, we assume that both mechanisms act concurrently, though one may dominate depending on the aging conditions.

As highlighted by Zaghdoudi et al. [119], chain scission reactions tend to reduce crosslink density, leading to material softening and degradation of elastic properties. In contrast, crosslinking during aging typically results in increased stiffness and can lead to brittleness. Our model aims to capture the combined effects of these opposing processes to accurately characterize material evolution under thermal aging. By identifying the dominant mechanism, we seek to improve predictions of long-term mechanical performance in cross-linked polymer systems.

The theoretical basis for quantifying these effects can be traced to the work of P.J. Flory, who used statistical mechanics to relate the elastic modulus of a polymer in the rubber phase to the num-

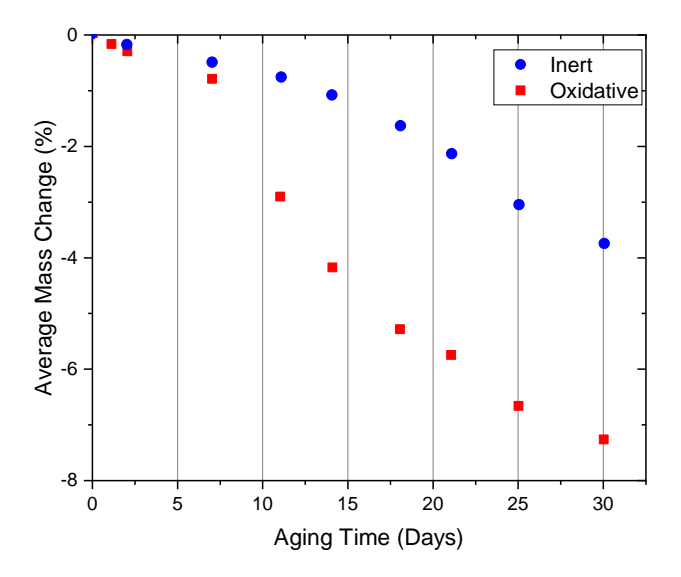


Figure 6.5: Evolution of the weight percentage loss as a function of the aging time (in days) for CFRP samples [70].

ber of elastically effective chains. This relationship establishes a direct link between macroscopic mechanical properties and underlying crosslink density.

## 6.4.2: Case Study: Thermal Vacuum Aging of Adhesives

Experimental data from Chen et al. [17] provide insight into how thermal aging under vacuum conditions affects polymeric adhesives. In their study (see Fig.6.6), various commonly used curing adhesives were exposed to a high vacuum ( $< 10^{-3}$  Pa) at a temperature of  $90^{\circ}$ C for 48 hours. This procedure simulated the combined effects of thermal and vacuum environments encountered in aerospace applications.

Post-aging analyses revealed a marked reduction in tensile strength across all adhesives tested. This degradation is attributed to the outward diffusion of small molecules, which led to microvoid formation near the surface and weakened the adhesive's resistance to tensile failure. The degree of mass loss was found to correlate strongly with reductions in mechanical performance, indicating a direct link between molecular migration and structural integrity.

Interestingly, the elastic modulus increased following aging, particularly in condensation-type

silicone rubber and epoxy-based adhesives. This increase is attributed to additional crosslinking reactions involving residual hydroxyl groups in the polymer network. Under thermal vacuum conditions, these groups reacted with trace water molecules, promoting further intermolecular crosslinking, increasing molecular weight, and resulting in a stiffer material.

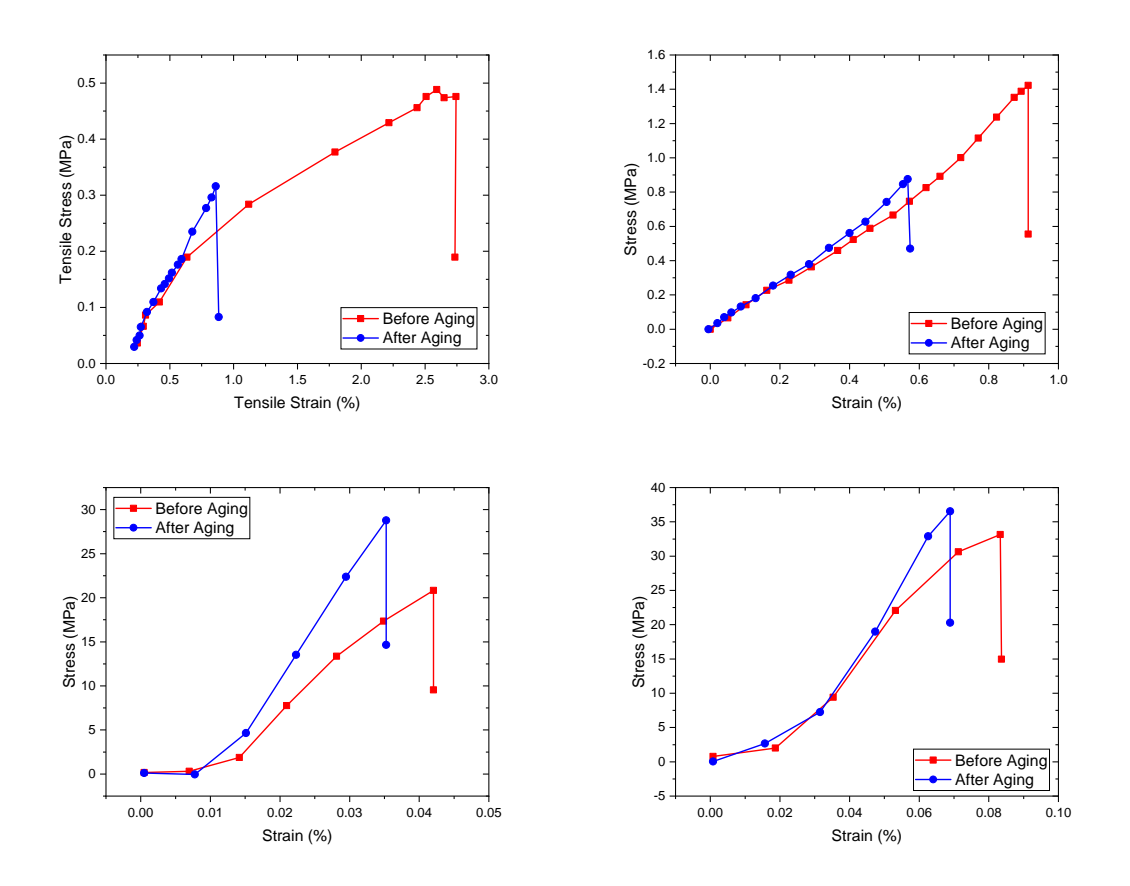


Figure 6.6: Tensile stress and strain before and after thermal vacuum aging; (a) condensation-type silicone rubber, (b) addition-type silicone rubber, (c) epoxy resin adhesive, (d) acrylic resin adhesive [17].

The polymer utilized in the research conducted by Tcharkhtchi and colleagues [104] was a polyurethane supplied by the RAIGI Company, located in Rouvray-Saint-Denis, France. To initiate the aging process, the samples were placed within autoclaves that had been purged with argon for a few minutes to establish an inert atmosphere. Subsequently, they were subjected to constant temperatures of both 85°C and 120°C. To ensure temperature stability, the autoclaves' temperatures were closely monitored and recorded throughout the study.

Tensile tests were performed using an Instron machine equipped with 10 KN load cells, and the

strain rate was set at 50mm/min. The dimensions of the test samples were as follows: 115 mm in length, 10 mm in width, and 4 mm in thickness. Figure 6.7 illustrates the impact of aging on stress-strain curves obtained from these tensile tests. The variation in tensile stress levels can be observed at different stages during the polymer aging process:

- During the initial phase, there was a notable increase in Young's modulus and stress at the
  breaking point after the post-cross-linking process. This observation indicates that the polymer was not fully cross-linked prior to the aging process.
- In the subsequent phase, both Young's modulus and stress at the breaking point exhibited a decrease, ultimately returning to their initial values and stabilizing. This phenomenon can be attributed to the rise in critical molecular weight and the reduction in cross-link density, primarily as a consequence of chain scission within the polymer network.

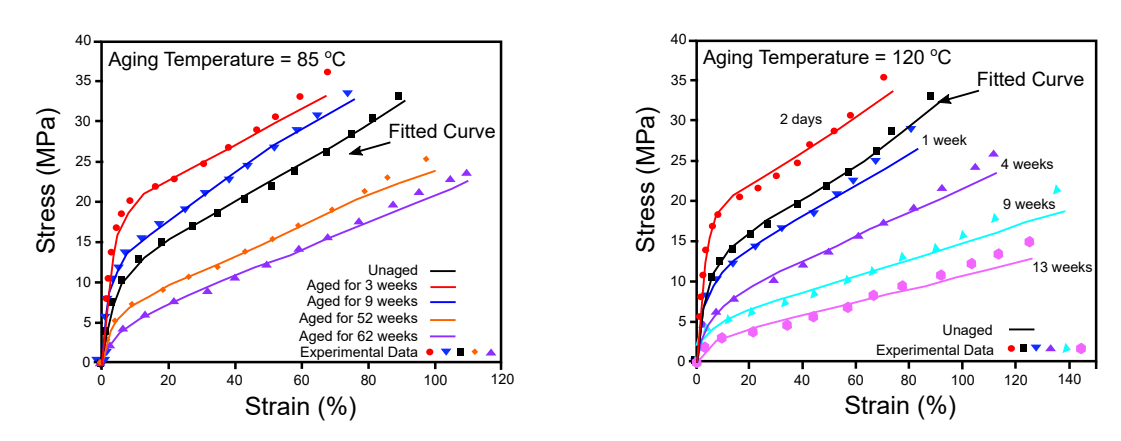


Figure 6.7: Stress-strain curves of the polyurethane at different stages of aging; (a) at  $85^{\circ}C$ , (b) at  $120^{\circ}C$  [104].

The test procedures outlined by Ozmen and detailed in their study ( [90]) were carried out on PMR-15 neat resin, with no pre-existing thermal aging. The experimental investigations encompassed strain-controlled tests focused on tension-to-failure behavior, involving monotonic loading with varying strain rates. Specifically, the influence of strain rate was examined in tension-to-failure tests conducted at consistent strain rates of  $10^6$ ,  $s^{-1}$ ,  $10^5$ ,  $s^{-1}$ ,  $10^4$ ,  $s^{-1}$ , and  $10^3$ ,  $s^{-1}$ .

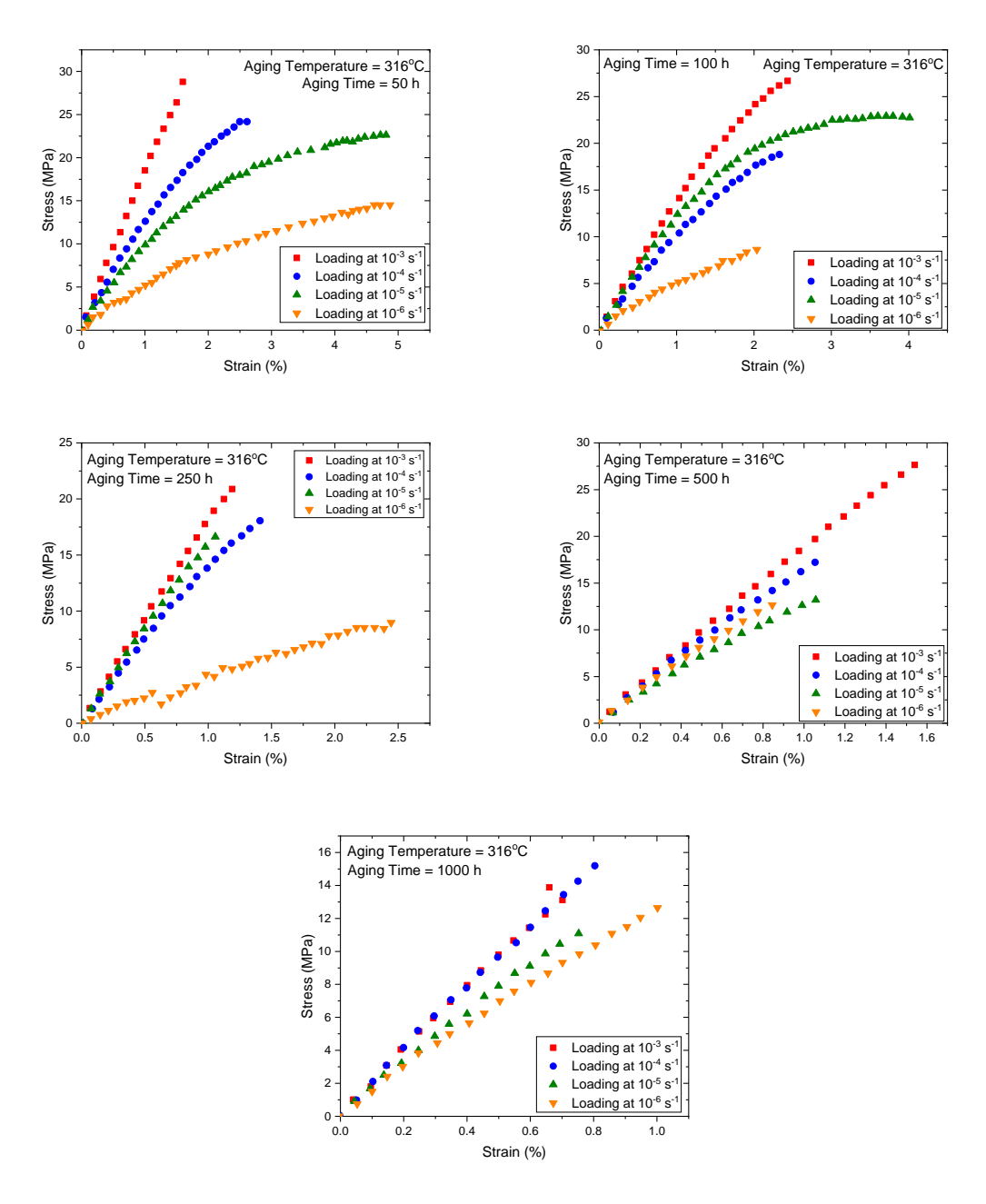


Figure 6.8: Stress-strain curves for PMR-15 Specimens aged at  $316^{\circ}C$  in Argon Obtained in Tensile Tests to Failure for aging time: (a) 50 hours, (b) 100 hours, (c) 250 hours, (d) 500 hours, (e) 1000 hours [90].

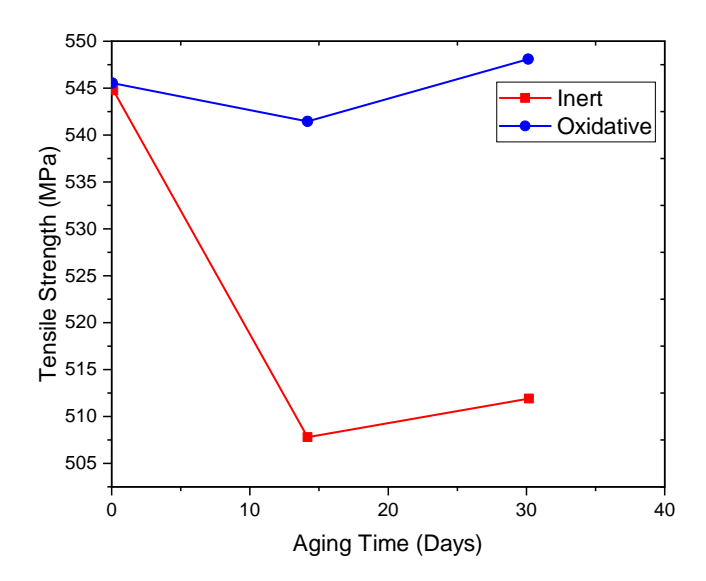


Figure 6.9: Evolution of tensile strength as a function of thermal aging time (in days) of CFRP samples [70].

# 6.5: Reaction Kinetics and Modeling Assumptions

To construct a predictive micromechanical model for the thermal aging of cross-linked polymers, it is essential to characterize the underlying reaction kinetics and molecular architecture evolution under inert (oxygen-free) conditions. Thermal degradation in such systems typically involves two concurrent and competing mechanisms: chain scission and crosslinking. Both processes exhibit strong temperature dependence and influence the material's mechanical performance.

## 6.5.1: Temperature-Dependent Reaction Rate Modeling

In a finite element framework, temperature-dependent kinetics can be incorporated by defining the reaction rate k(T) as a function of temperature. Many thermal aging processes exhibit a non-monotonic rate, increasing to a peak and then decreasing due to kinetic limitations or depletion of reactive species. This behavior can be captured by a Gaussian-exponential product:

$$k(T) = A \cdot \exp\left(-\frac{(T-\mu)^2}{2\sigma^2}\right) \cdot \exp\left(-\lambda(T-T_{\text{peak}})\right),\tag{6.1}$$

where:

- A is the amplitude (maximum rate),
- $\mu$  is the mean temperature (center of the Gaussian),
- $\sigma$  controls the spread (width of the Gaussian),
- $\lambda$  is the decay constant post-peak,
- $T_{\text{peak}}$  is the temperature at which the rate is maximized.

This formulation enables a flexible representation of reaction kinetics and can be integrated into constitutive models implemented within user-defined finite element subroutines.

#### 6.5.2: Polymer Chain Distribution and Crosslinking Behavior

To model the evolving molecular structure under thermal aging, we consider the polymer chain distribution using the Schulz-Zimm form, which generalizes the most probable distribution:

$$W(r) = \frac{\sigma^{\sigma}}{\mu\Gamma(\sigma)} \left(\frac{r}{u}\right)^{\sigma} \exp\left(-\frac{\sigma r}{u}\right),\tag{6.2}$$

where r is the chain length,  $\mu$  is the number-average chain length, and  $\sigma$  characterizes distribution breadth.

The evolution of the chain weight fraction distribution due to random crosslinking is given by Kimura's expression:

$$W(r,x) = \frac{r}{\mu^2} \cdot \left[ \frac{\sigma^{\sigma+1}}{\Gamma(\sigma+1)} \left( \frac{r}{u} \right)^{\sigma-1} + \sum_{k=2}^{\infty} \alpha_k \left( \frac{r}{u} \right)^{k\sigma+2k-3} \right] \cdot \exp\left( -(\sigma+2\mu x) \frac{r}{u} \right). \tag{6.3}$$

Crosslink density is defined as  $\rho=2x$ , accounting for two units per linkage. The normalized chain length distribution m(r,x) satisfies:

$$\int_0^\infty rm(r,x)\,dr = 1,\tag{6.4}$$

and relates to the weight and number fraction distributions as:

$$m(r,x) = \frac{W(r,x)}{r} = \frac{N(r,x)}{P_r},$$
 (6.5)

where  $P_n$  is the number-average chain length, and  $[P_r]$  is the concentration of chains of length r.

The evolution of m(r, x) with respect to crosslinking density is governed by Saito's integrodifferential equation:

$$\frac{\partial m(r,x)}{\partial x} = -2rm(r,x) + \int_0^r h \cdot (r-h) \cdot m(h,x) \cdot m(r-h,x) \, dh, \tag{6.6}$$

For an initial Schulz-Zimm distribution, the analytical solution becomes:

$$W(r,\rho) = \frac{1}{\mu} \cdot (r\mu)^{\sigma} \exp\left[-(\sigma + \rho\mu)\frac{r}{\mu}\right] \cdot \left(\sum_{k=0}^{\infty} \frac{\sigma^{(k+1)(\sigma+1)}(\rho\mu)^{k}}{(k+1)!\Gamma[(k+1)(\sigma+1)]} \left(\frac{r}{\mu}\right)^{k(\sigma+2)}\right).$$
(6.7)

# 6.5.3: Monte Carlo Simulation of Random Cross-Linking

To complement the analytical formulation, a Monte Carlo simulation is developed to stochastically model the crosslinking process. This method enables the inclusion of history-dependent interactions and spatial randomness not captured in deterministic models.

- 1. **Initialization:** Generate a chain population according to the Schulz-Zimm distribution.
- 2. **Crosslink Selection:** Randomly select chain ends for potential crosslinking based on predefined probabilities or spatial proximity.
- 3. **Update:** Modify molecular structures to include T- or H-shaped branching after each successful link.
- 4. **Iteration:** Repeat until a target crosslinking density  $\rho$  is reached.

This approach allows modeling of branching, gelation, and network connectivity, providing valuable validation and insights beyond analytical solutions.

## 6.5.4: Evolution of Chain Length Distribution with Crosslink Density

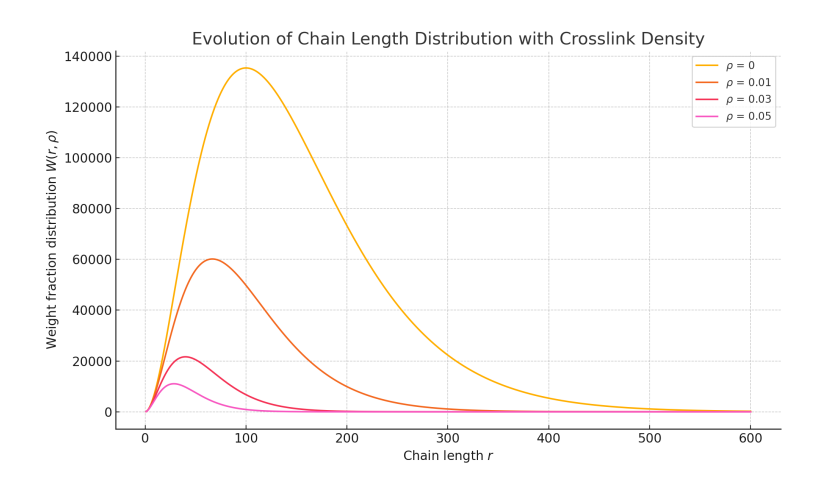


Figure 6.10: Evolution of the chain length distribution  $W(r, \rho)$  as a function of increasing crosslink density  $\rho$ , with parameters  $\mu = 100$ ,  $\sigma = 2$ . As  $\rho$  increases from 0 to 0.05, the peak of the distribution shifts toward shorter chain lengths and the curve broadens, indicating the progressive formation of branched and networked structures due to thermal aging.

Fig.6.10 illustrates how thermal aging influences the molecular architecture of a cross-linked polymer network. At low crosslink density, the system is dominated by long linear chains. As  $\rho$  increases, the average chain length decreases and the distribution broadens, indicating the emergence of branched and interconnected structures consistent with network formation.

# **6.6: Constitutive Model**

Constitutive models for rubber-like materials are typically classified as either phenomenological or micro-mechanical. The distinction lies in the construction of the strain energy function  $W(\mathbf{F})$ . Phenomenological models express W using strain invariants (e.g.,  $I_1$ ,  $I_2$ ), while micro-mechanical models derive constitutive behavior from polymer physics [42, 106].

This section presents a physically motivated constitutive model for cross-linked polymers that captures nonlinear inelastic behaviors, including an idealized Mullins effect, as well as chemically induced aging. The idealized Mullins effect (also called stabilized softening) is modeled independently of unloading/reloading paths.

## 6.6.1: Statistical Mechanics of Polymers

Experimental studies show that elastomers consist of long polymer chains oriented randomly in three dimensions [117, 118]. Each chain comprises multiple monomers and is constrained by two end linkages, often due to physical or chemical cross-linking (see Fig.6.11).

We assume the polymer network is a three-dimensional assembly of one-dimensional chains distributed in all orientations (Fig.6.12). The macroscopic strain energy  $W(\mathbf{F})$  is calculated as the directional average of the microscopic energies of these chains, integrated over the unit sphere.

A freely rotating chain (FRC) contains n Kuhn segments, each of length l, resulting in an end-to-end distance  $\sqrt{nl}$ . The sub-network stretch in a given direction d is defined as:

$$\lambda^{d} = \sqrt{d^{T} \mathbf{F}^{T} \mathbf{F} d}. \tag{6.8}$$

We use the following notation: scalars F, vectors  $\mathbf{F}$ , second-order tensors  $\mathbf{F}$ , and fourth-order tensors  $\mathbb{F}$ . A bar over a variable indicates normalization by Kuhn length l, e.g.,  $\bar{X} = \frac{X}{l}$ .

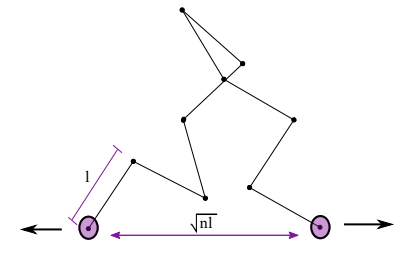


Figure 6.11: Schematic of a single polymer chain consisting of n segments of length l, total contour length nl.

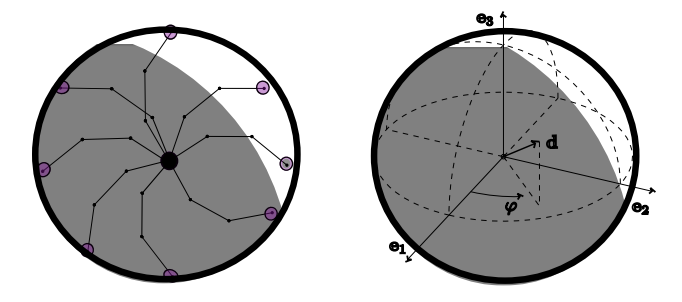


Figure 6.12: (a) A single polymer chain with n segments and contour length nl; (b) a micro-sphere structure with directional vector  $\mathbf{d}_i \in \mathbb{R}^3$ .

#### 3D Network Energy

The macroscopic strain energy function is computed via directional integration:

$$W(\mathbf{F}) = \frac{1}{4\pi} \int_{S} \rho_r^{\mathbf{d}} \psi^{\mathbf{d}} dA \approx \sum_{i=1}^{k} \rho_r^{\mathbf{d}_i} \omega_i \psi^{\mathbf{d}_i}.$$
 (6.9)

Here,  $\psi^d$  is the entropic energy of a single chain in direction d, and  $\omega_i$  are weights associated with collocation directions on the sphere.

#### **Single Chain Energy**

The entropic energy of a single freely rotating chain is:

$$\hat{\psi}_c(\bar{n}) = \bar{n}K_B T \int_0^\tau \hat{\beta} \, d\hat{\tau} + \psi_0, \quad \hat{\beta} = \left[1 - \frac{1 + \tau^2}{\bar{n}}\right] \beta, \tag{6.10}$$

with:

$$\tau = \frac{\lambda^d}{\sqrt{\bar{n}}}, \quad \beta = L^{-1}(\tau) \approx \frac{\tau}{1-\tau} + 2\tau - \frac{8}{9}\tau^2.$$
 (6.11)

#### **Damage Modeling**

We consider two damage mechanisms: mechanical and environmental. These are assumed to be superimposable. Thus, chain deterioration is modeled as a function of temperature T, time t, and deformation  $\mathbf{F}$ .

Under mechanical loading, short chains debond from cross-links or surfaces. Following Marckmann et al. [81], damage is modeled via evolution of active chain length  $\bar{n}^d$  and active chain density  $\rho_r^d$ :

$$\hat{n}^{\mathbf{d}} = n_0 \exp(\mu \lambda_m^{\mathbf{d}}), \quad \rho_r^{\mathbf{d}} = \rho_{r_0} \exp(-\mu \lambda_m^{\mathbf{d}}), \tag{6.12}$$

where  $\lambda_m^d$  is the maximum experienced stretch in direction d, and  $\mu$  is a damage sensitivity parameter.

For chemical aging (absent mechanical load), damage is modeled through changes in chain

density:

$$\rho_0 = \rho_{r_\infty} \exp(\mu \lambda_m) + \rho_{r_0} \cdot c \ln c \cdot \frac{c - \mu \lambda_m}{\mu_0 \exp(kt - \frac{E_a}{RT})},$$
(6.13)

where c is concentration,  $\mu_0$  and k are fitting parameters,  $E_a$  is activation energy, and R is the universal gas constant.

#### **Constitutive Formulation**

Assuming incompressibility:

$$\det(\mathbf{F}) = 1. \tag{6.14}$$

The first Piola-Kirchhoff stress tensor is:

$$\mathbf{P} = \frac{\partial W(\mathbf{F})}{\partial \mathbf{F}} - p\mathbf{F}^{-T},\tag{6.15}$$

where p enforces incompressibility.

The derivative of W is:

$$\frac{\partial W}{\partial \mathbf{F}} = \sum_{j=1}^{k} \omega_{j} \rho_{r}^{\mathbf{d}_{j}} \frac{\partial \psi_{t}^{\mathbf{d}_{j}}}{\partial \lambda^{\mathbf{d}_{j}}} \cdot \frac{1}{2\lambda^{\mathbf{d}_{j}}} \cdot \frac{\partial (\mathbf{d}_{j}^{T} \bar{\mathbf{C}} \mathbf{d}_{j})}{\partial \bar{\mathbf{F}}} : \frac{\partial \bar{\mathbf{F}}}{\partial \mathbf{F}}.$$
(6.16)

With simplification:

$$\frac{\partial \psi_c}{\partial \lambda^d} = \sqrt{\bar{n}} K_B T \hat{\beta}, \quad \frac{\partial (\mathbf{d}^T \bar{\mathbf{C}} \mathbf{d})}{\partial \bar{\mathbf{F}}} : \frac{\partial \bar{\mathbf{F}}}{\partial \mathbf{F}} = 2 \mathbf{J}^{-1/3} \bar{\mathbf{F}} (\mathbf{d} \otimes \mathbf{d}). \tag{6.17}$$

The final expression for the first Piola-Kirchhoff stress is:

$$\mathbf{P} = K_B T \sum_{i=1}^k \rho_r^{\mathbf{d}_i} \sqrt{\bar{n}^{\mathbf{d}_i}} L^{-1} \left( \frac{\lambda^{\mathbf{d}_i}}{\sqrt{\bar{n}^{\mathbf{d}_i}}} \right) \frac{\omega_i}{\lambda^{\mathbf{d}_i}} \mathbf{J}^{-1/3} \bar{\mathbf{F}} (\mathbf{d}_i \otimes \mathbf{d}_i) - p \mathbf{F}^{-T}.$$
(6.18)

## **6.7: Finite Element Linearization**

This section presents the algorithmic framework and variational formulation for implementing the proposed constitutive model in a finite element (FE) environment. Both the second Piola-Kirchhoff stress tensor and the consistent tangent modulus  $\mathbb{C}$  are derived within a total Lagrangian finite strain framework under the assumption of incompressibility and plane stress. The nonlinear system is solved using the Newton-Raphson method, which requires linearization of the internal force residual. The linearized stress-strain relation takes the form:

$$\delta \mathbf{S} = \mathbb{C} : \delta \mathbf{E},\tag{6.19}$$

where  $\delta \mathbf{S}$  and  $\delta \mathbf{E}$  are the increments of the second Piola-Kirchhoff stress and Green-Lagrange strain tensors, respectively.

#### 6.7.1: Stress Linearization

The second Piola-Kirchhoff stress is derived from the strain energy density function  $\mathcal{W}(\mathbf{F})$ , differentiated with respect to the Green-Lagrange strain  $\mathbf{E}=\frac{1}{2}(\mathbf{C}-\mathbf{I})$ . Under the incompressibility constraint, the stress tensor is expressed as:

$$\mathbf{S} = \frac{\partial \mathcal{W}(\mathbf{F})}{\partial \mathbf{E}} - pJ\mathbf{C}^{-1} = 2\frac{\partial \mathcal{W}(\mathbf{F})}{\partial \bar{\mathbf{C}}} : \frac{\partial \bar{\mathbf{C}}}{\partial \mathbf{C}} - pJ\mathbf{C}^{-1}, \tag{6.20}$$

where  $\bar{\mathbf{C}} = J^{-2/3}\mathbf{C}$  is the isochoric (deviatoric) part of the right Cauchy-Green tensor.

The projection tensor  $\frac{\partial \bar{C}}{\partial C}$  in the Lagrangian description is given by:

$$\frac{\partial \bar{\mathbf{C}}}{\partial \mathbf{C}} = J^{-2/3} \left( \mathbb{I} - \frac{1}{3} \mathbf{C} \otimes \mathbf{C}^{-1} \right), \tag{6.21}$$

where  $\mathbb{I}$  is the fourth-order identity tensor. Substituting Eq. (6.21) into Eq. (6.20) gives:

$$\mathbf{S} = 2J^{-2/3} \frac{\partial \mathcal{W}(\mathbf{F})}{\partial \bar{\mathbf{C}}} - \frac{2}{3}J^{-2/3} \left( \frac{\partial \mathcal{W}(\mathbf{F})}{\partial \bar{\mathbf{C}}} : (\mathbf{C} \otimes \mathbf{C}^{-1}) \right) - pJ\mathbf{C}^{-1}.$$
(6.22)

## 6.7.2: Out-of-Plane Stress Elimination

To enforce the plane stress condition, we set the out-of-plane Cauchy stress  $\sigma_{33}$  to zero. Solving for the Lagrange multiplier p, we define:

$$\mathbf{S}^n = 2\frac{\partial \mathcal{W}}{\partial \bar{\mathbf{C}}},\tag{6.23}$$

and obtain:

$$p = J^{-5/3} \mathbf{S}_{33}^n F_{33}^2 - \frac{1}{3} J^{-5/3} \mathbf{S}^n : \mathbf{C}.$$
 (6.24)

Substituting into the expression for **S**, the final form of the second Piola-Kirchhoff stress under plane stress becomes:

$$\mathbf{S} = J^{-2/3} \left( \mathbf{S}^n - \mathbf{S}_{33}^n F_{33}^2 \mathbf{C}^{-1} \right). \tag{6.25}$$

# **6.7.3: Tangent Modulus Derivation**

The derivation procedure for the tangent modulus is illustrated in Fig.6.13.

The consistent Lagrangian elasticity tensor is:

$$\mathbb{C} = \frac{\partial \mathbf{S}}{\partial \mathbf{E}} = 2 \frac{\partial \mathbf{S}}{\partial \mathbf{C}} = 2 \frac{\partial \mathbf{S}}{\partial \bar{\mathbf{C}}} : \frac{\partial \bar{\mathbf{C}}}{\partial \mathbf{C}}.$$
 (6.26)

Define:

$$\mathbb{C}^n = 4 \frac{\partial^2 \mathcal{W}}{\partial \bar{\mathbf{C}}^2}, \quad \mathbf{Z} = \begin{bmatrix} 0 & 0 & 0 \\ 0 & 0 & 0 \\ 0 & 0 & 2F_{33}^2 \end{bmatrix}, \quad \mathbf{Z}' = \begin{bmatrix} 0 & 0 & 0 \\ 0 & 0 & 0 \\ 0 & 0 & 2F_{33} \end{bmatrix}.$$

The full Lagrangian tangent stiffness is then expressed as:

$$\mathbb{C} = -\frac{2}{3}J^{-2/3} \left( \mathbf{S}^{n} - \mathbf{S}_{33}^{n} F_{33}^{2} \mathbf{C}^{-1} \right) \otimes \mathbf{C}^{-1} 
+ J^{-4/3} \left( \mathbb{C}^{n} - \frac{1}{3} \mathbb{C}^{n} : \mathbf{C} \otimes \mathbf{C}^{-1} - \mathbf{C}^{-1} \otimes \mathbb{C}^{n} : \mathbf{Z} + \frac{1}{3} (\mathbf{C} : \mathbb{C}^{n} : \mathbf{Z}) \mathbf{C}^{-1} \otimes \mathbf{C}^{-1} \right) 
- J^{-2/3} \left( 2\mathbf{S}^{n} : \mathbf{Z}' \mathbf{C}^{-1} \otimes \frac{\partial F_{33}}{\partial \mathbf{C}} - 2\mathbf{S}^{n} : \mathbf{Z} \mathbf{C}^{-1} \otimes \mathbf{C}^{-1} \right).$$
(6.27)

The required derivatives are:

$$\frac{\partial F_{33}}{\partial \mathbf{C}} = \frac{1}{2} \mathbf{F}^{-1} \mathbf{F}', \quad \mathbf{F}' = F_{33}^2 \begin{bmatrix} -F_{22} & F_{21} & 0 \\ F_{12} & -F_{11} & 0 \\ 0 & 0 & 0 \end{bmatrix}.$$

Figure 6.13: Tangent Modulus Derivation Procedure.

# **6.7.4: Plane Stress Simplification**

For the plane stress case, the simplified derivation procedure and resulting tensor are shown in Fig.6.14.

Under plane stress, the out-of-plane components of the stress tensor vanish:

$$\delta \mathbf{S}_{13} = \delta \mathbf{S}_{23} = \delta \mathbf{S}_{31} = \delta \mathbf{S}_{32} = 0.$$

Using Voigt-Mandel notation, the stress-strain relation becomes:

$$\begin{bmatrix} \delta \mathbf{S}_{11} \\ \delta \mathbf{S}_{22} \\ \delta \mathbf{S}_{12} \\ \delta \mathbf{S}_{33} \end{bmatrix} = \begin{bmatrix} \mathbb{C}_{1111} & \mathbb{C}_{1122} & \mathbb{C}_{1112} & \mathbb{C}_{1133} \\ \mathbb{C}_{2211} & \mathbb{C}_{2222} & \mathbb{C}_{2212} & \mathbb{C}_{2233} \\ \mathbb{C}_{1211} & \mathbb{C}_{1222} & \mathbb{C}_{1212} & \mathbb{C}_{1233} \\ \mathbb{C}_{3311} & \mathbb{C}_{3322} & \mathbb{C}_{3312} & \mathbb{C}_{3333} \end{bmatrix} \begin{bmatrix} \delta \mathbf{E}_{11} \\ \delta \mathbf{E}_{22} \\ 2\delta \mathbf{E}_{12} \\ \delta \mathbf{E}_{33} \end{bmatrix}.$$
(6.28)

To eliminate  $\delta \mathbf{E}_{33}$ , we use:

$$\mathbf{E}_{33} = \frac{1}{2}(\mathbf{C}_{33} - 1) - \frac{1}{2}(F_{33}^2 - 1).$$

Differentiating yields:

$$\delta \mathbf{E}_{33} = \frac{1}{2} F_{33} \mathbf{F}^{-1} \mathbf{F}' : \delta \mathbf{E}. \tag{6.29}$$

Define:

$$\mathbf{A} = \frac{1}{2} F_{33} \mathbf{F}^{-1} \mathbf{F}'.$$

The reduced plane stress elasticity matrix becomes:

$$C = \begin{bmatrix} \mathbb{C}_{1111} & \mathbb{C}_{1122} & \mathbb{C}_{1112} \\ \mathbb{C}_{2211} & \mathbb{C}_{2222} & \mathbb{C}_{2212} \\ \mathbb{C}_{1211} & \mathbb{C}_{1222} & \mathbb{C}_{1212} \end{bmatrix} + \begin{bmatrix} A_{11}\mathbb{C}_{1133} & A_{22}\mathbb{C}_{1133} & 2A_{33}\mathbb{C}_{1133} \\ A_{11}\mathbb{C}_{2233} & A_{22}\mathbb{C}_{2233} & 2A_{33}\mathbb{C}_{2233} \\ A_{11}\mathbb{C}_{1233} & A_{22}\mathbb{C}_{1233} & 2A_{33}\mathbb{C}_{1233} \end{bmatrix}.$$
(6.30)

The detailed derivations of  $S^n$  and  $\mathbb{C}^n$  are provided in the Appendix.

Figure 6.14: Plane Stress Simplification Procesure.

The detailed derivations of  $S^n$  and  $\mathbb{C}^n$  are provided in the Appendix.

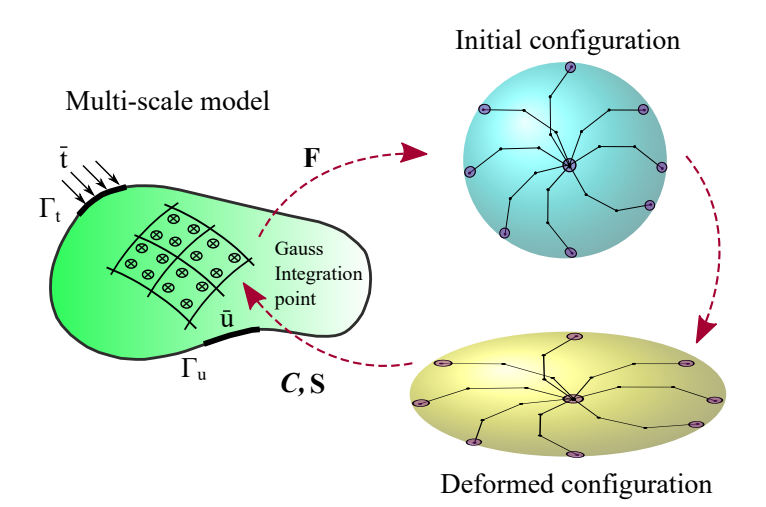


Figure 6.15: A schematic figure of the hierarchical micro-macro multi-scale approach.

#### Algorithm 1: Hierarchical Atomistic-Continuum Multi-Scale Method

#### 1. Initialization

- Discretize the domain with a finite element mesh; assign an atomistic RVE to each integration point.
- Loop over integration points:

  - $\begin{array}{l} \text{ Set initial deformation gradient } F = I. \\ \text{ Characterize each atomistic RVE; store initial atomic coordinates.} \\ \text{ Compute first Piola-Kirchhoff stress } P \text{ and tangent modulus } \mathbb{C}_{PF} \text{ from the RVE.} \\ \text{ Upscale } P \text{ and } \mathbb{C}_{PF} \text{ to the macroscopic integration point.} \\ \text{ Compute second Piola-Kirchhoff stress } S \text{ and tangent modulus } \mathbb{C}_{SE} \text{ via} \end{array}$ continuum mechanics.
- End loop over integration points.
- 2. For each increment  $(n \rightarrow n+1)$ :
  - Initialize variables from the last converged state.
  - Apply external loads or prescribed displacements.
- 3. For each iteration  $(i \rightarrow i + 1)$ :
  - Assemble global stiffness matrix **K**; solve for incremental displacement **u**.
  - Update nodal positions accordingly.
  - Loop over integration points:
    - Recalculate deformation gradient F in current and reference configurations. Apply F to RVE under periodic boundary conditions. Recompute P and  $\mathbb{C}_{PF}$  at the atomistic level. Upscale results to the continuum integration point. Update S and  $\mathbb{C}_{SE}$ .
  - End loop over integration points.
  - Compute internal force vector and residual; check for convergence.
- 4. Check for convergence:
  - If converged, proceed to the next increment.
  - Otherwise, repeat the next iteration.

# 6.8: Validation and Results

Fig. 6.16 presents the stress-strain curve from monotonic tension-to-failure tests conducted by [35]. These experiments were carried out at temperatures of  $288^{\circ}C$  and  $316^{\circ}C$  with four different aging durations: unaged (conducted at room temperature without aging), aged for 100, 250, and 1000 hours. The unaged experimental results were utilized to calibrate the parameters of the constitutive model developed. Fig. 6.16 shows the model predictions for the stress-strain curve of PMR-15 under these different aging conditions. Comparison of the predicted stress-strain curve with the experimental data demonstrated an error of less than 10%, validating the accuracy and effectiveness of the model.

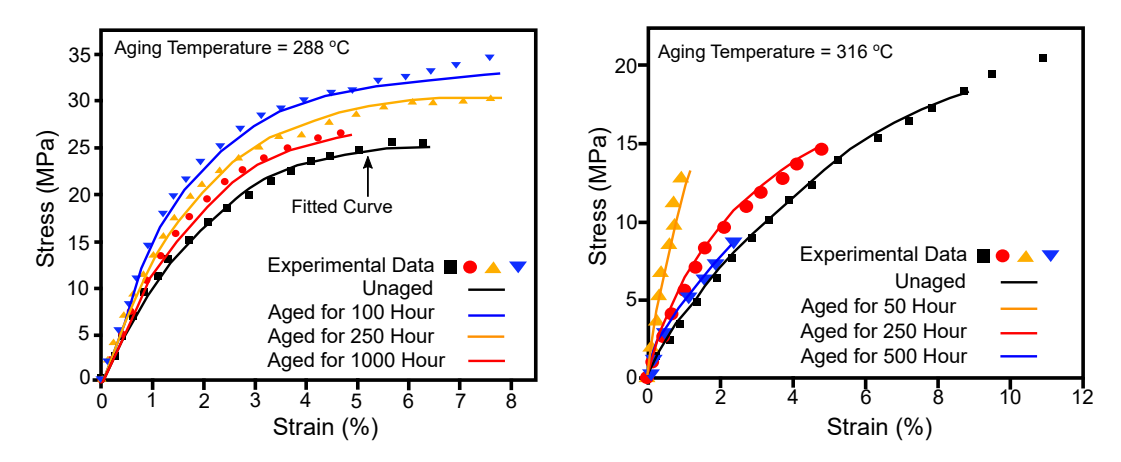


Figure 6.16: Stress-strain curve obtained in monotonic tension to failure tests for PMR-15 aged in Argon in (a) 288°C, and (b) 316°C [35].

Fig.6.17 compares deformation results obtained from two implementations developed in this work: (a) a custom Abaqus subroutine and (b) a MATLAB script. The MATLAB code was originally inspired by the framework presented in [9], which modeled hydrolysis and thermo-oxidative aging. However, the code was significantly adapted and extended to model inert aging conditions relevant to our study. The strong agreement between both implementations confirms the correctness and consistency of our computational models.

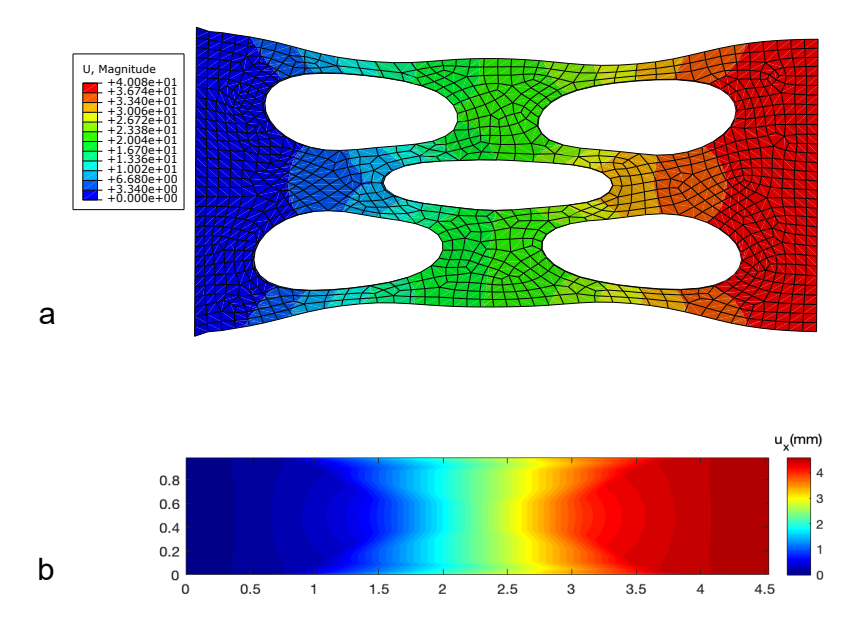


Figure 6.17: Deformation results comparison: (a) Abaqus subroutine implementation (UMAT) and (b) MATLAB simulation.

The UMAT subroutine (the UMAT code, written in Fortran, is provided in the Appendix) was derived using an open-source library called Tensor Toolbox, which was implemented in the Fortran programming language. This library provides essential tensor operations that are crucial for the derivation of the tangent modulus in the context of nonlinear material models. The Tensor Toolbox enables efficient and accurate handling of tensor calculations, which are integral to computing the material's stress-strain relationship and, consequently, the tangent modulus.

The tangent modulus is essential due to the nonlinear behavior of materials like rubber under large deformations. In nonlinear finite element analysis (FEA), iterative solvers, such as the Newton-Raphson method, rely on the tangent stiffness matrix to update the material's behavior at each iteration and ensure accurate convergence of the solution.

### 6.8.1: Numerical Simulation Results

Two sets of numerical results on different inert thermal aging temperature are presented here to demonstrate the finite element simulation of the mechanical response of cross-linked polymers. The objective of this simulation is to show the capability of the numerical model to accurately predict the response of the polymer material under different inert aging conditions. These two

examples are a classical dog-bone specimen under prescribed displacements along -x direction. Due to the thin film assumption, the plane stress assumption is adopted.

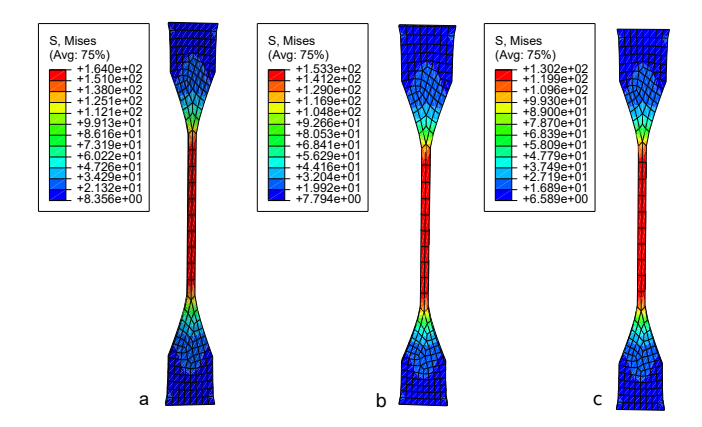


Figure 6.18: Evolution of Second Piola–Kirchhoff Stress in Epoxy Resin Under Inert Thermal Aging at 60°C and Mechanical Loading (UMAT Results).

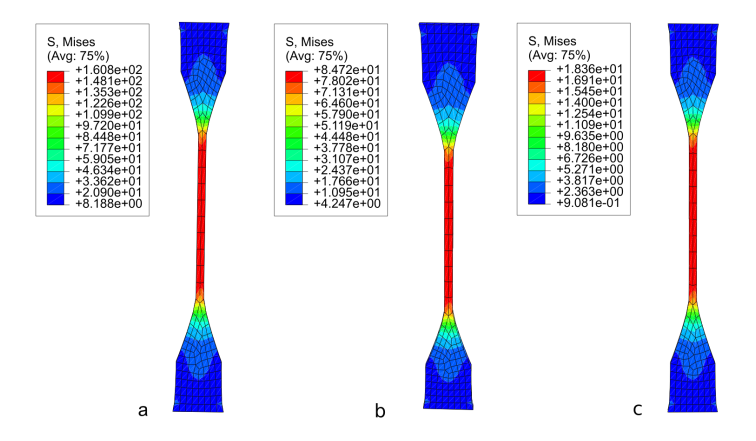


Figure 6.19: Evolution of Second Piola–Kirchhoff Stress in Epoxy Resin Under Inert Thermal Aging at 80°C and Mechanical Loading (UMAT Results).

# CHAPTER 7: CONSTITUTIVE MODELING OF DIFFUSION-LIMITED OXIDATION (DLO) COUPLED WITH A LARGE DEFORMATION THEORY FOR POLYMER DEGRADATION

## 7.1: Abstract

The impact of oxidation on polymer degradation is a crucial aging process, particularly when it's confined to the surface of the sample, often referred to as diffusion-limited oxidation (DLO). DLO entails a complex interplay between oxygen absorption, diffusional transport, and oxygen's reaction within elastomers. In this study, a novel kinetics-based model for oxygen absorption is developed and rigorously validated against a range of experimental datasets. Furthermore, the diffusion-reaction equation is extended into three dimensions and solved using the Alternating Direction Implicit (ADI) method. Various reaction rate functions are considered to account for chain scission and network reformation reactions, enabling the description of non-uniform degradation patterns.

The enhanced model is employed to simulate heterogeneous oxidation and to showcase how different contributing factors influence the oxidation behavior of nitrile rubber. Notably, the outcomes of our proposed model align closely with empirical data concerning the degree of oxidation in polymers. Additionally, a constitutive model is formulated to incorporate the intricate interplay between diffusion, chemical reactions, and large deformations in polymers. This model is seamlessly integrated into a finite element framework to illustrate its predictive capabilities concerning the effects of diffusion-limited oxidation (DLO) on the mechanical properties of cross-linked polymers. It allows for a comprehensive numerical analysis of the coupled diffusion-reaction and mechanical behaviors exhibited by polymers undergoing DLO.

# 7.2: Introduction

Polymers employed in engineering applications, including those used in aerospace and turbine engines, possess a finite lifespan primarily due to the effects of degradation. This degradation predominantly results from environmental factors that are present throughout the manufacturing and service life of these materials. The three primary factors responsible for the heterogeneous aging of polymers are ultraviolet (UV) radiation, ozonation, and oxidation [6, 60, 67]. To ensure the effective design of polymer materials for engineering applications in extreme conditions, it becomes crucial to accurately predict their long-term stiffness and strength, as well as to model the mechanisms leading to degradation and eventual failure. In many cases, polymers experience a substantial degradation in their performance and mechanical properties due to the effects of aging, which becomes particularly pronounced in highly specialized applications [116]. High-temperature oxidation or thermo-oxidative aging in polymers serves as a prominent illustration of aging mechanisms. In this scenario, oxygen permeates elastomeric materials and engages in chemical reactions with active polymer sites. Consequently, layers of oxides start to develop in proximity to the exposed surface, fostering conditions conducive to the initiation and spread of micro-cracks within the material. This phenomenon can exert a substantial influence on the mechanical characteristics and overall structural integrity of the polymer as time progresses. [27]. These micro-cracks not only propagate but also exacerbate the oxidation process within the material, ultimately culminating in the failure of the material [15, 16, 25]. Upon exposure to air, elastomers interact with oxygen at their surface boundary, a process governed by Henry's law. The adsorbed oxygen then proceeds to diffuse into the material, initiating polymer reactions that ultimately lead to polymer degradation. A substantial body of recent research has delved into examining the alterations in the polymer's network structure stemming from thermo-oxidation [26, 32, 103]. The aging of polymers under thermal oxidative conditions, especially under accelerated conditions, frequently encompasses complex and non-uniform degradation mechanisms associated with diffusion-limited oxidation (DLO) phenomena [29, 50]. The shape of DLO highly depends on the oxidation rate, oxygen diffusivity, thickness of the sample, and the presence of antioxidants [14, 48]. Heterogeneous oxidation in elastomers is driven by diffusion reaction, resulting in changes in the mechanical properties of elastomers [24, 78, 94, 95, 108]. Chain scission and cross-linking processes play pivotal roles in reshaping the polymer network, resulting in significant alterations in the material's behavior during oxidation. These changes induced by oxidation are extensively documented in recent literature and include phenomena such as an increase in modulus, a decrease in glass transition temperature, and reduced failure strain, among others [11, 39–41, 82]. The stress distribution in the elastomers can also be affected by oxidation. Hence, considering DLO would enable us to accurately predict the stiffness of polymers during aging. Therefore, the uncertainty in the performance prediction of the sample can be avoided [49,75]. Modeling heterogeneous oxidation in elastomers poses significant challenges due to the intricate interplay of physical, chemical, and thermo-mechanical mechanisms that evolve over time during the aging process. In the context of polymer oxidation, a comprehensive understanding involves a set of six elementary reactions. Extensive research has also been conducted to investigate the impact of chain reactions on polymer oxidation, resulting in the development of kinetic models that aim to describe these oxidative processes in polymers [7, 8, 28, 111]. For a thick elastomer specimen, the DLO model was introduced in [96], which described the depth and extent of DLO in various circumstances. The adsorption and diffusion of oxygen in the elastomer play a major role in heterogeneous thermo-oxidative aging [56, 64, 102]. The absorption processes and the subsequent diffusion of oxygen molecules into elastomers have been investigated experimentally [57]. In this study, the paper reports findings on the solubility of oxygen and the degree of oxidation throughout the thickness of Nitrile Rubber during the aging process. Additionally, a model has been developed to effectively represent the absorption of oxygen and the extent of oxidation in elastomers. This model takes into consideration variables such as temperature and aging time to provide insights into these critical aspects of polymer behavior during aging [58].

In order to predict how polymers respond to diffusion-limited oxidation, researchers have integrated the balance of momentum with the diffusion-reaction equation. This approach allows for an in-depth exploration of how non-uniformly oxidized polymers behave as they age. The concept

of coupling multiple physical phenomena in material constitutive modeling has been extensively studied in the field of mechanics. For instance, a coupled theory was developed to explain high-temperature oxidation in metallic alloys. This illustrates the interdisciplinary nature of materials science and mechanics in understanding complex phenomena [79]. The coupled stress-diffusion response in polymer gels has been extensively studied by [19–21,37,51]. The reaction-diffusion coupling in photo-responsive gels is also noteworthy work [113]. Several works have also been done on coupled photo-chemical reaction-large deformation theory as [33, 100, 112]. The non-uniform degree of oxidation leads to variations in mechanical properties and results in an inhomogeneous distribution of stress and strain within the oxidized polymer [83,89,92].

This study refines the oxygen absorption model and validates its ability to replicate experimental findings. We expand the diffusion-reaction equation into three dimensions and elaborate on the solution method using the ADI numerical approach. Novel reaction rate functions for chain scission and network reformation, accounting for oxygen concentration and oxidation levels, enhance predictive accuracy. Our DLO modeling, employing these reaction rate functions, exhibits improved correlation with experimental data. Additionally, we develop a constitutive model to explore oxidation progression under mechanical loads and its impact on polymer mechanical properties during aging. This model incorporates the interplay between diffusion, chemical reactions, and polymer deformation. We then implement the model within a finite element framework to analyze how polymers respond to DLO. Finally, we investigate the advancement of oxygen diffusion and the evolution of oxidation extent in cases of stress-coupled oxidation.

The paper is organized as follows. In section 7.3, the modified oxygen absorption model is presented. Section 7.4 explains the extended diffusion-reaction equation and ADI solution procedure. The results are analyzed in detail to explain the model's capability for the simulation of oxidation across the thickness of polymers. In section 7.5, the developed constitutive model for coupled stress-oxidation is introduced, and the model is further implemented in a FE setting by writing a user element subroutine (UEL). In the end, the concluding remarks are presented.

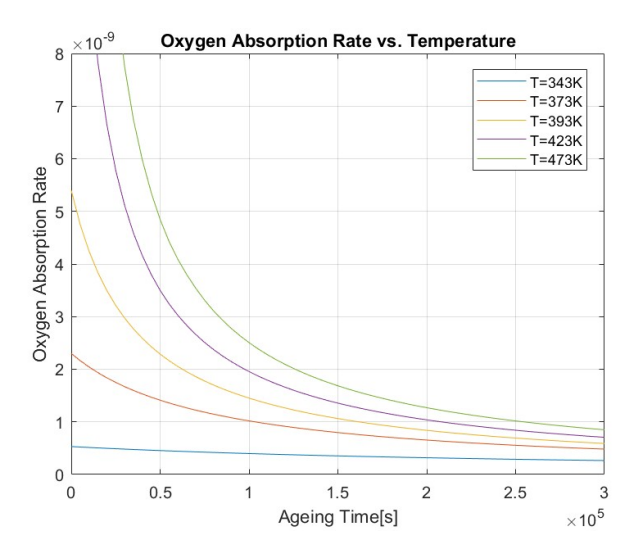


Figure 7.1: Oxygen Absorption Rate vs. Temperature.

# 7.3: Oxygen Absorption

Oxygen is soluble in polymers, and the permeation process can be split into solubility and diffusivity [107]. The solubility (also named oxygen uptake or absorption) describes the initial oxidation step and is provoked by the oxygen gradient between the polymer and the ambient environment as the driving force. Oxygen uptake is a function of temperature, ambient oxygen pressure, and the aging duration or rather the aging progress [101]. Fig.7.1 Illustrates the varying oxygen absorption rates of a polymer at different temperatures. This section uses the experimental data of oxygen absorption to verify the proposed oxygen uptake model. The experiment has been conducted on nitrile rubber, and provides the experimental results [59]. For details of the experiment procedure and the material used, see [59]. Oxygen uptake was measured by a respirometer and Differential Oxygen Analyzer. The samples were aged in sealed chambers at multiple elevated temperatures before the oxygen concentration of the contained air was measured. The difference in the amount of oxygen is measured before and after exposure, which is associated with elastomer absorption [55, 56]. The oxygen absorption model of oxidized material is developed to analyze the oxygen solubility in polymers. In aerobic aging, solubility is a significant factor mainly governed by the partial pressure of oxygen  $p_{ox}$ . The oxygen absorption rate,  $p_{ox}$ , at the exterior surface can be

calculated using Henry's law which describes it with respect to solubility rate coefficient S and the partial pressure  $p_{ox}$ , as given below:

$$\dot{m}_{O_2} = S \cdot p_{ox},\tag{7.1}$$

where S is a material parameter describing the solubility rate coefficient and is governed by chain scission and network reformation processes during exposure to air. The novelty of the proposed oxygen absorption model is that aging processes are divided into chain scission and network reformation parts to see how these processes affect the oxygen uptake in the superficial layer of the elastomer.

Another novelty of the proposed model is avoiding the complete stop of oxygen absorption. According to the work done by [58], oxygen diffusion is not prevented even for the totally oxidized part of the elastomer. So, even for the oxidized boundary, the oxygen is absorbed, diffusing into the elastomer in favor of the reaction. But, in the oxygen absorption model in [58], it was assumed that the fully aged superficial layer inhibits any uptake of oxygen molecules. Hence, in this work, the  $\beta$  parameter is defined, which is the model parameter and describes the maximum percentage of reduction of oxygen uptake by aging. Therefore, a complete oxygen uptake stop is avoided since it can only be reduced to a certain minimum of the initial value. Oxygen adsorbing at the elastomer's surface declines with aging and can be described by:

$$\dot{m}_{O_2} = p_{ox} \cdot S_0 \cdot \exp(\frac{-E_s}{RT}) \left( 1 - \beta \left( \frac{p^{sci} + p^{ref}}{2} \right) \right), \tag{7.2}$$

where  $S_0$  describes the initial solubility rate of the matrix,  $E_s$  the activation energy of solubility, R the universal molar gas constant, and T the absolute temperature. The aging parameters describe aging progress, whereas the value 0 describes virgin material, and 1 stands for a completely aged material. The accompanying evolution equation of chain scission and network reformation that describe the aging progress can be expressed as follows:

$$\dot{p}^{sci} = \nu_p^{sci} \cdot \exp\left(\frac{-E_p^{sci}}{RT}\right) \left(1 - p^{sci}\right)^2, \tag{7.3}$$

$$\dot{p}^{ref} = \nu_p^{ref} \cdot \exp(\frac{-E_p^{ref}}{RT}) \left(1 - p^{ref}\right)^2, \tag{7.4}$$

where  $\nu_p$  represents a proportionality factor and can be imagined as a temperature-independent velocity of the aging progress.  $E_p$  is the activation energy of the aging process. The oxygen uptake model introduced in [58] did not give any information about the effect of the size and geometry of the specimen on oxygen absorption. In this paper, the L parameter is defined, which is the surface-volume ratio of the sample. The basic solubility rate is considered a function of the surface-volume ratio in the model. An experiment was conducted on nitrile rubber, and the total mole of oxygen per gram of the sample weight was reported as a function of aging temperature and duration [59]. The bar-shaped samples (55x20x2mm) were aged at temperatures of 100,  $120^{\circ}C$  and for periods up to 72 h. The above model is used to describe the experimental results. The experimental data is converted to the total mole of oxygen per surface-volume ratio to investigate the capability of the developed model. Therefore, the evolution equation is solved by using ode45 MATLAB non-stiff differential equations solver and fitted to the experimental data.

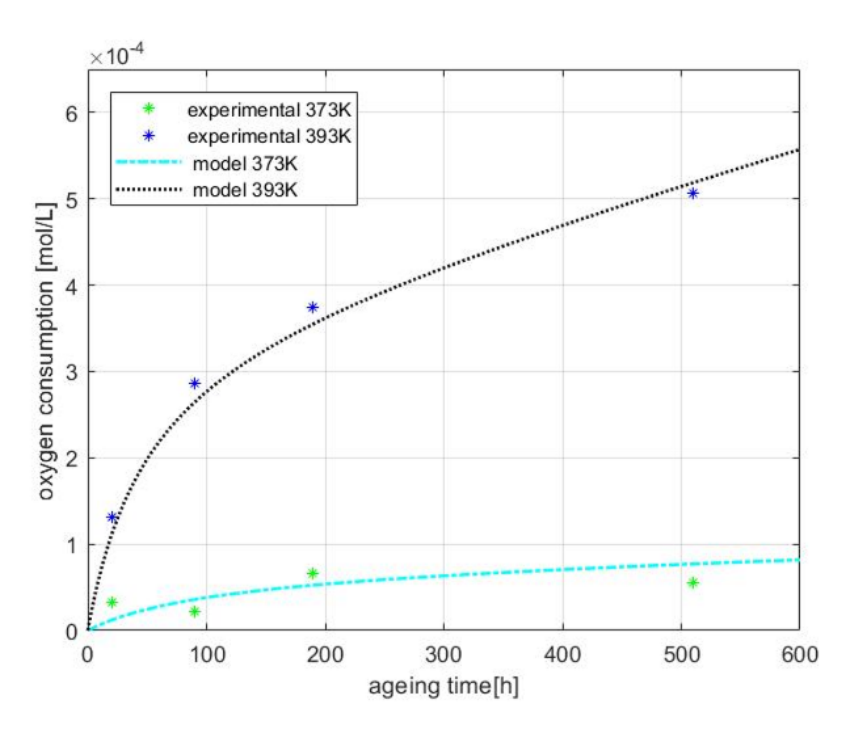


Figure 7.2: Oxygen consumption of the nitrile rubber as a function of aging temperature and duration.

Fig. 7.2 shows that the modeling approach can replicate the experimentally obtained oxygen absorption during aging. With ongoing exposure, the aging parameters increase according to the evolution equations, and the solubility of the sample is reduced. Hence, the oxygen absorption rate is decelerated during aging. The parameters used for the modeling shown in Fig. 7.2 are chosen as declared in Table 7.1.

$p_{ox}(Kpa)$	2	R[J/mol/K]	8.3145
$S_0$ [mol/L/s/Pa]	$1.8 \times e^{-6}$	$ u_p^{sci}$	10
$E_s$	$5.6 \times e^4$	$ u_p^{ref}$	10
$E_p^{sci}$	47000	$E_p^{ref}$	47000

Table 7.1: Parameters for modeling of oxygen absorption behavior.

Nevertheless, measuring the oxygen uptake provides no information about the distribution of oxidation in the elastomer. Thus, no conclusion can be drawn about any kind of heterogeneity of oxidation. Hence, besides solubility, diffusivity plays an important role when considering the process of oxidative aging. Therefore, the diffusion process itself should be considered more in detail.

# 7.4: Diffusion reaction equation

As stated in the previous section, the chemical aging of an elastomer by oxidation is generally defined as a process involving several steps, including absorption, diffusion, and chemical reactions. After oxygen molecules are adsorbed due to the affinity of the polymer's surface for  $O_2$  molecules, a concentration gradient occurs in the exterior layer before the oxygen molecules subsequently diffuse into the material's interior. The most common approach to describe this kind of diffusion process is given by Fick's second law as follows.

$$\frac{\partial C}{\partial t} = \nabla \cdot (D_{ox} \nabla C), \qquad (7.5)$$

where oxygen concentration C and diffusivity are formulated as a function of the location in the material and aging time. Oxygen molecules react chemically with elastomers while it is diffusing

into the sample. Hence, based on the set of reactions for oxidation [99] and the general mass balance law for oxygen concentration, we can write,

$$\frac{\partial C}{\partial t} = \nabla \cdot (D_{ox} \nabla C) - r_{ox}^{sci} + r_{ox}^{ref}. \tag{7.6}$$

Oxygen is consumed in the propagation reaction and produced in the termination reaction.  $r_{ox}^{sci}$  and  $r_{ox}^{ref}$  are the rate of consumption or production of oxygen in chain scission and network reformation reactions, respectively. The reaction rate functions are a function of aging temperature and oxygen concentration. Both chemical aging reactions prevent oxygen from further diffusion since they create a chemical compound with a network of elastomer molecules. Chain scission and network reformation are treated individually and are described by an Arrhenius approach. The reaction rate functions are a function of the elastomer's oxygen concentration, temperature, and extent of oxidation. If there is no oxygen, no oxidative reaction can occur. Consequently, the progression of aging can be described by the following reaction rate functions.

$$r_{ox}^{sci} = F(C)r_o^{sci} \exp\left(\frac{-E_r^{sci}}{RT}\right) (1 - p^{sci})^n, \tag{7.7}$$

$$r_{ox}^{ref} = F(C)r_o^{ref} \exp\left(\frac{-E_r^{ref}}{RT}\right) (1 - p^{ref})^n, \tag{7.8}$$

where  $r_o^{sci}$  and  $r_o^{ref}$  are constant factors influencing the velocity of the reactions. F(C) is a function to describe the reaction rate dependency on oxygen availability. The exponent n is a parameter used to adjust the effect of the extent of oxidation on reactivity. Thus, the reactivity reduces with the progressing aging process since the amount of convenient reaction partners decreases. The evolution equations that describe the progress of aging can be expressed as [58]:

$$\dot{p}^{sci} = \nu_p^{sci} \frac{r_{ox}^{sci}}{r_{ox_0}^{sci}},\tag{7.9}$$

$$\dot{p}^{ref} = \nu_p^{ref} \frac{r_{ox}^{ref}}{r_{ox_0}^{ref}}. (7.10)$$

Diffusivity is a function of temperature and is also affected by aging. Here, it is assumed that both types of oxidative reactions, chain scission, and network reformation, reduce the diffusivity of the elastomer in the same way. Thus, the diffusion coefficient  $D_{ox}$  is formulated as a function of the aging parameters chain scission  $p^{sci}$  and network reformation  $p^{ref}$ . The diffusion coefficient is written as:

$$D_{ox} = D_0 \cdot e^{-E_D/R\theta.\xi}, with \ \xi = \iota p^{sci} \cdot p^{ref}. \tag{7.11}$$

The model parameter  $\iota$  is used to adjust the influence of the aging parameters on the diffusion coefficient. In order to get a better understanding of heterogeneous aging, the diffusion-reaction equation is extended for three dimensions as the following equation:

$$\frac{\partial C}{\partial t} = D_{ox} \frac{\partial C^2}{\partial x^2} + \frac{\partial D_{ox}}{\partial x} \frac{\partial C}{\partial x} + D_{ox} \frac{\partial C^2}{\partial y^2} + \frac{\partial D_{ox}}{\partial y} \frac{\partial C}{\partial y} + D_{ox} \frac{\partial C^2}{\partial z^2} + \frac{\partial D_{ox}}{\partial z} \frac{\partial C}{\partial z} - r_{ox}^{sci} + r_{ox}^{ref}.$$
(7.12)

## 7.4.1: Numerical solution of the diffusion-reaction equation

The ADI method is used to solve the reaction-diffusion equation in three dimensions. In the ADI method, every time step is subdivided into three steps. This numerical procedure works so that a 3D problem is transformed into three 1D problems which can be solved with an implicit approach. The numerical solution can be simplified to three tridiagonal systems per time step. First, the concentration is calculated in the x-direction, second in the y-direction, and then in the z-direction [77]. The Douglas higher order ADI scheme is utilized for the accurate numerical solution to solve the 3D diffusion-reaction equation [36]. The second-order finite difference method is also used for discretizing the first derivative of oxygen concentration and diffusion with respect to directions. The first step provides the oxygen concentration C in the time step m+1/3. The following equations, i, j, and k, are used as variables to describe location dependency in the x, y, and z directions.

$$\frac{\left(C_{i,j,k}^{m+\frac{1}{3}} - C_{i,j,k}^{m}\right)}{\Delta t} = \frac{D}{h^{2}} \left[\frac{1}{2}\delta_{x}^{2}\left(C_{i,j,k}^{m+\frac{1}{3}} + C_{i,j,k}^{m}\right) + \delta_{y}^{2}\left(C_{i,j,k}^{m}\right) + \delta_{z}^{2}\left(C_{i,j,k}^{m}\right)\right] 
+ \frac{D_{i+1,j,k} - D_{i-1,j,k}}{2\Delta x} \frac{C_{i+1,j,k}^{m+\frac{1}{3}} - C_{i-1,j,k}^{m+\frac{1}{3}} + C_{i+1,j,k}^{m} - C_{i-1,j,k}^{m}}{4\Delta x} 
+ \frac{D_{i,j+1,k} - D_{i,j-1,k}}{2\Delta y} \frac{C_{i,j+1,k}^{m} - C_{i,j-1,k}^{m}}{2\Delta y} 
+ \frac{D_{i,j,k+1} - D_{i,j,k-1}}{2\Delta z} \frac{C_{i,j,k+1}^{m} - C_{i,j,k-1}^{m}}{2\Delta z} - r_{ox,i,j,k}^{sci,m} + r_{ox,i,j,k}^{ref,m}. \quad (7.13)$$

In the equation above,  $\delta^2$  is the second-order difference operator. The concentration  $C_{i,j,k}^{m+1/3}$  is the first step solution used by the ADI method and calculated at every grid point of the area with i, j, k = 1, ..., N. N stands for the number of grid points in the x, y, and z directions and h represents the constant distance between two points in the mesh grid. The Eqn. 7.13 can be written in the tridiagonal matrix and right-hand-side vector. Subsequently, an LU-factorization of the tridiagonal matrix is executed, which can be solved by the Thomas algorithm. The solution of Eqn. 7.13 contains a N tridiagonal equation system. A constant oxygen concentration  $C_0$  is assumed in the ambient environment. Hence, Dirichlet boundary conditions are used. After the first step, oxygen concentration  $C_{i,j,k}^{m+1/3}$  is obtained, the ADI method uses a second step to calculate the next step oxygen concentration  $C_{i,j,k}^{m+2/3}$ .

$$\frac{\left(C_{i,j,k}^{m+\frac{2}{3}} - C_{i,j,k}^{m}\right)}{\Delta t} = \frac{D}{h^{2}} \left[\frac{1}{2}\delta_{x}^{2}\left(C_{i,j,k}^{m+\frac{1}{3}} + C_{i,j,k}^{m}\right) + \delta_{y}^{2}\left(C_{i,j,k}^{m+\frac{2}{3}} + C_{i,j,k}^{m}\right) + \delta_{z}^{2}\left(C_{i,j,k}^{m}\right)\right] 
+ \frac{D_{i+1,j,k} - D_{i-1,j,k}}{2\Delta x} \frac{C_{i+1,j,k}^{m+\frac{1}{3}} - C_{i-1,j,k}^{m+\frac{1}{3}} + C_{i+1,j,k}^{m} - C_{i-1,j,k}^{m}}{4\Delta x} 
+ \frac{D_{i,j+1,k} - D_{i,j-1,k}}{2\Delta y} \frac{C_{i,j+1,k}^{m+\frac{2}{3}} - C_{i,j-1,k}^{m+\frac{2}{3}} + C_{i,j+1,k}^{m} - C_{i,j-1,k}^{m}}{4\Delta y} 
+ \frac{D_{i,j,k+1} - D_{i,j,k-1}}{2\Delta x} \frac{C_{i,j,k+1}^{m} - C_{i,j,k-1}^{m}}{2\Delta x} - r_{ox,i,j,k}^{sci,m+\frac{1}{3}} + r_{ox,i,j,k}^{ref,m+\frac{1}{3}}. \quad (7.14)$$

Analogously, the ADI method uses the final step to calculate the final oxygen concentration  $C^{m+1}$ .

$$\frac{\left(C_{i,j,k}^{m+1} - C_{i,j,k}^{m}\right)}{\Delta t} = \frac{D}{2h^{2}} \left[ \delta_{x}^{2} \left(C_{i,j,k}^{m+\frac{1}{3}} + C_{i,j,k}^{m}\right) + \delta_{y}^{2} \left(C_{i,j,k}^{m+\frac{2}{3}} + C_{i,j,k}^{m}\right) + \delta_{z}^{2} \left(C_{i,j,k}^{m+1} + C_{i,j,k}^{m}\right) \right] 
+ \frac{D_{i+1,j,k} - D_{i-1,j,k}}{2\Delta x} \frac{C_{i+1,j,k}^{m+\frac{1}{3}} - C_{i-1,j,k}^{m+\frac{1}{3}} + C_{i+1,j,k}^{m} - C_{i-1,j,k}^{m}}{4\Delta x} 
+ \frac{D_{i,j+1,k} - D_{i,j-1,k}}{2\Delta y} \frac{C_{i,j+1,k}^{m+\frac{2}{3}} - C_{i,j-1,k}^{m+\frac{2}{3}} + C_{i,j+1,k}^{m} - C_{i,j-1,k}^{m}}{4\Delta y} 
+ \frac{D_{i,j,k+1} - D_{i,j,k-1}}{2\Delta z} \frac{C_{i,j,k+1}^{m+1} - C_{i,j,k-1}^{m+1} + C_{i,j,k+1}^{m} - C_{i,j,k-1}^{m}}{4\Delta z} - r_{ox,i,j,k}^{sci,m+\frac{2}{3}} + r_{ox,i,j,k}^{ref,m+\frac{2}{3}}. \quad (7.15)$$

After finishing the calculation of a time step, the oxygen concentration  $C_{i,j,k}$  with  $i, j, k = 1, \dots, N$  is obtained, which is used to update the aging parameters  $p^{sci}$  and  $p^{ref}$ , and subsequently the diffusion coefficient  $D_{ox}$  at every grid point. The aging parameters are updated according to the evolution equations. The ADI method is unconditionally stable, and its accuracy is of second order with respect to time and space [36]. The evolution equations are solved numerically by means of the implicit finite difference method, which reads for the chain scission as follows. The numerical solution for the network reformation is implemented similarly and is therefore not shown here.

$$\frac{p_{i,j,k}^{sci,m+1} - p_{i,j,k}^{sci,m}}{\Delta t} = \nu_p^{sci} \frac{r_{ox}^{sci}}{r_{ox_0}^{sci}}.$$
(7.16)

The mentioned numerical method for solving the 3D diffusion reaction equation is used to visualize a cross-section in the sample during aging. Three-dimensional plotting gives a comprehensive visual impression of thermo-oxidative aging of a bar-shaped sample's cross-section and DLO. Model parameters are chosen as two-dimensional equations published in [58]. For illustration, a cube is considered and is aged up to 1000 seconds at 393 Kelvin. This aging time cannot be compared to the real aging behavior of elastomers. It is just a fictitious value and is used only to show the basic functionality of the model. Fig. 7.3 gives an example of the spatial development of the aging parameter  $p^{sci}$  for various depths of the cube.

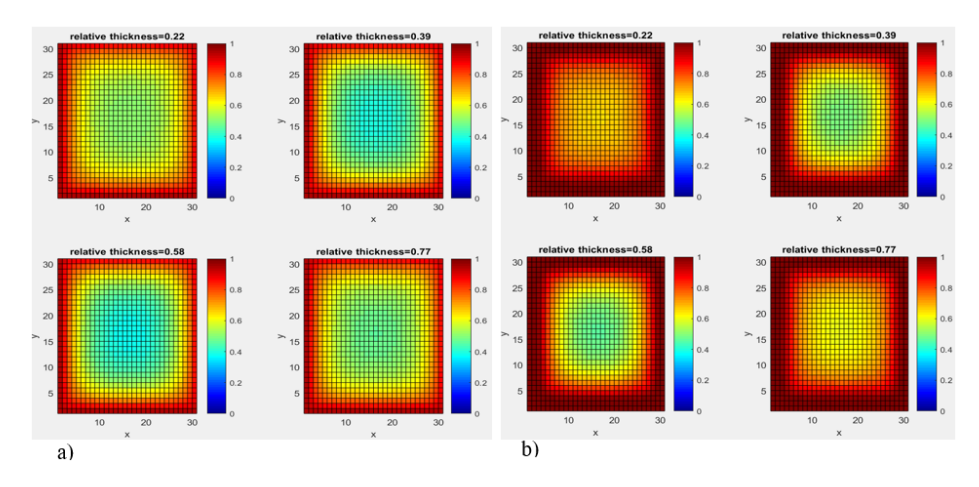


Figure 7.3: 3D Plot of the Aging Parameter  $\psi_{ci}$  Computed Using the Developed MATLAB Code for Varying Thicknesses and Aging Durations — (a) After 200 s, (b) After 1000 s.

In the ongoing process, oxidative reactions consume oxygen, decreasing the diffusivity. After a while, the surface layer is fully aged, and hence diffusivity is almost diminished. The diffusion coefficient decreases so that diffusion is reduced to a minimum by the progress of aging. For such high temperatures, DLO inhibits oxygen from reaching the core region of the sample. Therefore, heterogeneous oxidation occurs over the thickness of the sample.

#### 7.4.2: Reaction rate function schemes

The model introduced is applied to simulate the heterogeneous aging of peroxide-cured NBR in an oxygen-containing environment. An experiment has been conducted on nitrile rubber, and the carbonyl-to-nitrile ratio was reported during aging. To describe the degree of oxidation from both the theoretical and experimental side, it was assumed that the carbonyl nitrile ratio is equalized with the aging parameter  $p^{sci}$  [57]. The modeling approach tries to consider the experimental findings. Therefore, the reaction terms are modified to adjust the influence of aging on reactivity. Here, for better correlation with experimental data, some reaction rate functions for chain scission and network reformation processes are proposed, and their capability is investigated. The reaction-diffusion equation with reaction terms for chain-scission and network reformation is used, and the model is adjusted and fitted to the data obtained by FTIR investigation in [57]. The reaction rate functions consider the non-linear contribution of the aging parameters  $p^{sci}$  and  $p^{ref}$  and oxygen

concentration. The aim of investigating the proposed reaction rate functions is to find the best reaction functions that can accurately describe the extent of oxidation in elastomers. Here are three schemes for reaction rate functions for chain scission reactions based on an Arrhenius approach.

$$r_{ox}^{sci} = \frac{C}{C_0} r_0^{sci} \exp\left(\frac{-E_r^{sci}}{RT}\right) (1 - p^{sci})^2, \tag{7.17}$$

$$r_{ox}^{sci} = \frac{\alpha C}{1 + \beta C} r_0^{sci} \exp\left(\frac{-E_r^{sci}}{RT}\right) (1 - p^{sci}), \tag{7.18}$$

$$r_{ox}^{sci} = \left[ \frac{2\alpha C}{1 + \beta C} \right] \left[ 1 - \frac{\beta C}{2(1 + \beta C)} \right] r_0^{sci} \exp\left( \frac{-E_r^{sci}}{RT} \right) (1 - p^{sci})^{1/2}.$$
 (7.19)

The reaction terms for network reformation  $r_{ox}^{ref}$  are formulated analogously. The  $\alpha$  and  $\beta$  are the parameters to consider the effect of oxygen concentration on the reaction rate functions. The model can describe the oxidative profiles, whereas equating the aging parameter  $p^{sci}$  and the carbonyl nitrile ratio must be interpreted cautiously.

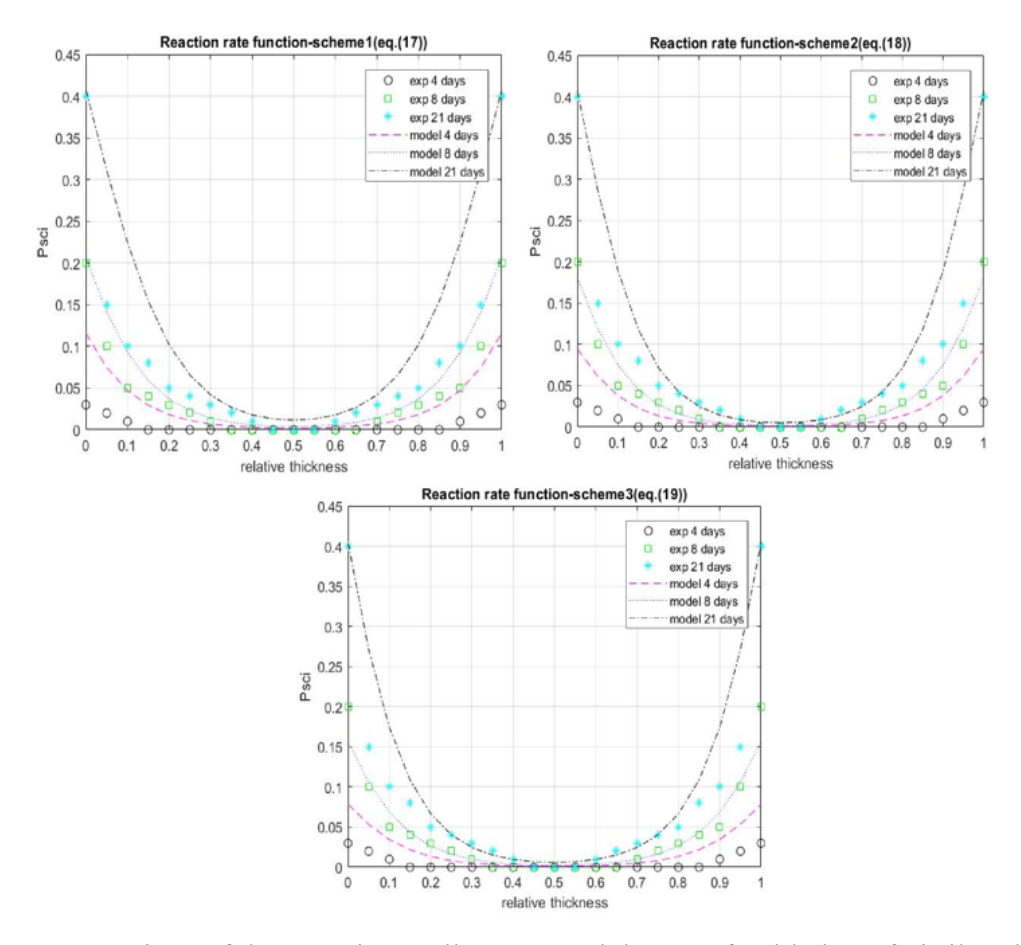


Figure 7.4: Comparison of the experimentally measured degree of oxidation of nitrile rubber aged at 393 K with model predictions using three different reaction rate schemes.

The first scheme of reaction rate functions was proposed by Herzig et al. [57]. Fig. 7.4 illustrates that the proposed functions for reaction rate have a better correlation with experimentally measured degree of oxidation. It is clear that several factors like the type of raw material, oxygen concentration, and presence of antioxidants or temperature influence the degree of heterogeneity. The parameters used for modeling nitrile rubber oxidation shown in Fig. 7.4 are chosen as stated in Table 7.2.

$D_0[m^2/s]$	$1 \times e^{-5}$	$E_D[J/mol]$	$3.5 \times e^4$
$r_0^{sci}[mol/l/s]$	7	$r_0^{ref}[mol/l/s]$	7
$E_r^{sci}[J/mol]$	$2.3 \times e^4$	$E_r^{ref}[J/mol]$	$2.4 \times e^4$
$ u_p^{sci}$	0.5	$ u_p^{ref}$	0.5

Table 7.2: Parameters used for modeling of carbonyl-nitrile-ratio of the NBR.

## 7.4.3: Linkage of oxygen absorption and diffusion-reaction behavior

After oxygen is absorbed, there are four possibilities for subsequent progression: Oxygen is dissolved in the elastomer without any chemical reaction, it reacts with the elastomer (oxidative reactions), it reacts with the antioxidant, or it is adsorbed by the elastomer again. The amount of absorbed oxygen can be calculated by summing up these cases during aging. The currently dissolved oxygen in the elastomer is added to the oxygen consumption in the chain scission reaction, the oxygen production in the network reformation reaction, and binding oxygen molecules by means of antioxidation. Thus, the amount of oxygen absorbed from the beginning of exposure until aging time t can be calculated as an output of the diffusion-reaction model. That allows us to compare the calculated amount of absorbed oxygen with the experimental data obtained in Section 7.3. Therefore, the following relationship can calculate the total amount of absorbed oxygen.

$$m_{ox} = m_{dis} + m_{re} = \iiint\limits_{V} C_{o_2} dv + \int_0^t \iiint\limits_{V} \left( r_{ox}^{sci} - r_{ox}^{ref} + r_{ox}^{ant} \right) dv.$$
 (7.20)

The currently dissolved amount of oxygen is obtained by the summation of the present oxygen at every spatial element of the whole sample. The total amount of oxygen reacted after absorption is calculated by summing up the consumption, production, and reaction of oxygen with antioxidants of every previous time step since the start of exposure. The three reaction rate function schemes for chain scission and network reformation are implemented for calculating the Eqn. 7.20. The amount of absorbed oxygen can be plotted over the aging duration and represents a by-product of the model. The efficacy of the schemes for reaction rate functions is investigated by comparing the model results with oxygen absorption tests, illustrated in Fig. 7.5.

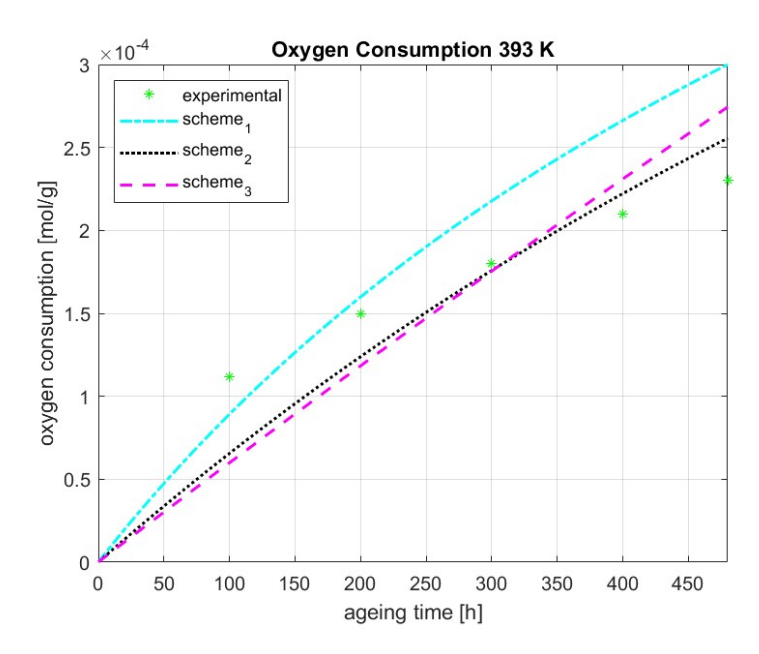


Figure 7.5: Comparison of oxygen absorption profiles over aging time using three reaction rate models.

The primary reason for the disparities between the experimental data and the simulation outcomes is the existence of antioxidants. In the initial stages of exposure, a portion of the oxygen reacts with antioxidants, an effect that is not currently accounted for in the diffusion-reaction model. However, over time, the antioxidants will gradually lose their effectiveness. To improve the alignment between simulation results and experimental data, it is crucial to incorporate the reaction between oxygen and antioxidants into the model, thereby providing a more accurate representation of the real-world conditions.

# 7.5: Constitutive model for stress-coupled oxidation

In this section, the consistent chemo-mechanically coupled theory is developed for polymer oxidation. The developed model will most likely help to reach an advanced level in describing elastomer aging. For example, the effect of mechanical loads on diffusion or the extent of oxidation, chain scission, and network reformation, in general, can be analyzed more deeply.

We identify such a macroscopically homogeneous body B with the region of space it occupies in a fixed reference configuration and denote by X an arbitrary material point of B. A motion

of B is then a smooth one-to-one mapping  $X = \chi(X, t)$  with deformation gradient, velocity, and velocity gradient is given by:

$$\mathbf{F} = \nabla \chi,$$
  $v = \dot{\chi},$   $\mathbf{L} = gradv = \dot{\mathbf{F}}\mathbf{F}^{-1}.$  (7.21)

We use the standard notation of modern continuum mechanics [52]. Specifically:  $\nabla$  and Div denote the gradient and divergence with respect to the material point X in the reference configuration; grad and div denote these operators with respect to the point  $\mathbf{x} = \chi(X, t)$  in the deformed body; a superposed dot denotes the material time-derivative. We consider a multiplicative decomposition of the total deformation gradient based on the large deformation theory of polymers as follows:

$$\mathbf{F} = \mathbf{F}^e \mathbf{F}^p, \tag{7.22}$$

where  $\mathbf{F}^e$  is the elastic component of the deformation gradient and  $\mathbf{F}^p$  is the irreversible plastic component. Referring to Eqn. 7.22, the determinant  $\mathbf{J}$  can be decomposed into,

$$\mathbf{J} = \mathbf{J}^e \mathbf{J}^p$$
, Where,  $\mathbf{J}^e = \det(\mathbf{F}^e)$ ,  $\mathbf{J}^p = \det(\mathbf{F}^p)$ . (7.23)

Further, the velocity gradient is defined as  $\mathbf{L} = \dot{\mathbf{F}}\mathbf{F}^{-1}$ , which can be subdivided into the elastic part and inelastic part as  $\mathbf{L}^e = \dot{\mathbf{F}}^e\mathbf{F}^{-e}$  and  $\mathbf{L}^p = \dot{\mathbf{F}}^p\mathbf{F}^{-p}$ . The elastic and plastic deformation tensor can be further defined from the standard continuum mechanics as symmetric and skew-symmetric. So,  $\mathbf{L}^e = \mathbf{D}^e + \mathbf{W}^e$  and  $\mathbf{L}^p = \mathbf{D}^p + \mathbf{W}^p$ . We also make another kinematic assumption that the plastic stretch  $\mathbf{D}^p$  can be additively decomposed into  $\mathbf{D}^p = \mathbf{D}^s + \mathbf{W}^{vp}$ , where  $\mathbf{D}^s$  represents the inelastic strain rate due to oxidation-induced shrinkage and  $\mathbf{W}^{vp}$  represents the inelastic strain rate due to bulk viscoplastic deformation in the polymer. The readers are suggested to refer to earlier literature for the detailed equations of the kinematics of deformation of polymers, such as [2–4]. Among the set of reactions in elastomers, chain scission reaction plays a major role in oxidative shrinkage [2]. Hence, we have considered the following simple form for  $\mathbf{D}^s$  as Eq.(24), where  $\gamma < 0$  is a material

parameter determining the volume shrinkage amount.

$$\mathbf{D}^{S} = \gamma \cdot r_{ox}^{sci} \cdot I, \qquad with, tr(\mathbf{D}^{S}) = 3\gamma r_{ox}^{sci}. \tag{7.24}$$

Motivated by the free energy representation in [71], a separable form of the free energy is considered as:

$$\psi_R(C^e, C_{ox}, p^{sci}, p^{ref}) = \psi_R^{mech} + \psi_R^{chem} + \psi_R^{diff}. \tag{7.25}$$

In this article, the 8-chain model of Arruda-Boyce [5] is utilized as a free energy function for the mechanical part as,

$$\psi_R^{mech} = n_c \cdot K_B \cdot T \cdot N \cdot \left[ \sqrt{N^{-1}} \Lambda \zeta + \ln(\frac{\zeta}{\sinh(\zeta)}) \right] + \frac{K}{2} \ln(\mathbf{J})^2, \tag{7.26}$$

where  $n_c$  is the chain density in the elastomer,  $K_B$  denotes for Boltzmann's constant, N is the number of segments of length l in a chain,  $\Lambda$  is the chain stretch, and  $\zeta$  abbreviates the inverse Langevin function. In this article, we aim to describe the influence of heterogeneous oxidation on the mechanical properties of elastomers. To do so, it is assumed that the chain density can be affected by both oxidative reactions, chain scission, and network reformation. The chain density in elastomers is reduced by chain scission reactions and is increased by network reformation reactions. Therefore, the following relationship is proposed for considering the effect of oxidation on chain density during aging.

$$n_c = n_{c_0} \left( 1 - p^{sci} + \Gamma p^{ref} \right).$$
 (7.27)

In the equation. (27),  $n_{c_0}$  represents the original chain density at the beginning of the exposure. Both aging parameters can evolve inhomogeneously, thereby leading to inhomogeneous stress. Following the work presented in [47], we consider that the material's bulk modulus does not depend on oxidation. For the reactive part of the free energy, a simple quadratic function of the extent of

the reaction is considered.

$$\psi_R^{chem} = \frac{1}{2} \left[ H^{sci} (1 - p^{sci})^2 + H^{ref} (1 - p^{ref})^2 \right], \tag{7.28}$$

where the parameters  $H^{sci}$  and  $H^{ref}$  are the chemistry modulus for the chain scission and network reformation reactions. Here we have used Flory-Huggins theory to define the free energy for oxygen diffusion [42]. Oxygen is considered the only diffusing species into elastomers, as given by,

$$\psi_R^{diff} = \mu_0^{o_2} C_R^{o_2} + RT C_R^{o_2} \left( ln(\frac{\Omega C_R^{o_2}}{1 + \Omega C_R^{o_2}}) + \chi(\frac{1}{1 + \Omega C_R^{o_2}}) \right), \tag{7.29}$$

where  $\mu_0^{o_2}$  is the reference chemical potential for oxygen,  $\chi$  is the dimensionless Flory-Huggins interaction parameter, and  $\Omega$  is the volume of a mole of oxygen. Thus, the complete free energy expression can now be written as,

$$\psi_{R} = n_{c} \cdot K_{B} \cdot T \cdot N \cdot \left[ \sqrt{N^{-1}} \Lambda \cdot \zeta + \ln(\frac{\zeta}{\sinh(\zeta)}) \right] + \frac{K}{2} \ln(J)^{2} + \frac{1}{2} \left[ H^{sci} (1 - P^{sci})^{2} + H^{ref} (1 - P^{ref})^{2} \right] + \mu_{0}^{o_{2}} C_{R}^{o_{2}} + RT \cdot C_{R}^{o_{2}} \left( \ln(\frac{\Omega C_{R}^{o_{2}}}{1 + \Omega C_{R}^{o_{2}}}) + \chi(\frac{1}{1 + \Omega C_{R}^{o_{2}}}) \right).$$

$$(7.30)$$

From the free energy and using the guidelines for thermodynamic restriction, it is possible to get the specific constitutive equations for the second Piola stress  $S^e$ , chemical potential of oxygen,  $\mu^{o_2}$  and affinity of each reaction. The Second Piola-Kirchoff stress can be expressed in the following form:

$$\mathbf{S}^{e} = 2\frac{\partial \psi_{R}}{\partial \mathbf{C}^{e}} = K \cdot \ln J \cdot \mathbf{C}^{-e} + J^{-\frac{2}{3}} \left[ \bar{\mathbf{S}} - \frac{1}{3} (\bar{\mathbf{C}}^{e} : \bar{\mathbf{S}}) . \bar{\mathbf{C}}^{-e} \right], \tag{7.31}$$

$$\bar{\mathbf{S}} = \frac{n_c \cdot K_B \cdot \theta}{3} \left[ \frac{3.N - \Lambda^2}{N - \Lambda^2} \right] \cdot I. \tag{7.32}$$

Chemical potential can be obtained by taking the partial derivative of the total free energy with

respect to the oxygen concentration as,

$$\mu^{o_2} = \frac{\partial \psi}{\partial C_R} = \mu_0^{o_2} + RT \left( ln(\frac{\Omega \cdot C_R^{o_2}}{1 + \Omega C_R^{o_2}}) + (\frac{1}{1 + \Omega C_R^{o_2}}) + \chi(\frac{1}{1 + \Omega C_R^{o_2}})^2 \right). \tag{7.33}$$

This work considers the effect of oxygen concentration and the extent of reactions in the reaction rate functions for the coupled stress-oxidation scenario. Therefore, the following relationships are proposed to control the influences of oxygen availability, aging parameters, and applied stress on the evolution of reactions in the elastomers in the case of stress-coupled oxidation.

$$r_{ox}^{sci} = \frac{\alpha C}{1 + \beta C} r_0^{sci} \exp\left(\frac{-\mathbf{E}_r^{sci}}{RT}\right) (1 - p^{sci}) \cdot F^{sci}, \tag{7.34}$$

$$r_{ox}^{ref} = \frac{\alpha C}{1 + \beta C} r_0^{ref} \exp\left(\frac{-\mathbf{E}_r^{ref}}{RT}\right) (1 - p^{ref}) \cdot F^{ref}. \tag{7.35}$$

The  $F^{sci}$  and  $F^{ref}$  are reactive forces for chain scission and network reformation reactions, which express the dependency of reaction rate on the mechanical load. We can express the reactive forces for the individual reaction as,

$$F^{sci} = A^{sci} + \gamma tr(C^e \cdot S^e) - \mu^{o_2}, \tag{7.36}$$

$$F^{ref} = A^{ref} + \mu^{o_2}. (7.37)$$

The  $A^{sci}$  and  $A^{ref}$  are defined as the affinity of chain scission and network reformation reactions. Due to the fact that both oxidation reaction effects are considered in chain density during aging, the following relationships can be obtained from the total free energy:

$$A^{sci} = -\frac{\partial \psi_R^{mech}}{\partial p^{sci}} + H^{sci}(1 - p^{sci})$$

$$= n_{c_0} K_B N \left[ \sqrt{N^{-1}} \Lambda \zeta + \ln \left( \frac{\zeta}{\sinh(\zeta)} \right) \right] + H^{sci}(1 - p^{sci}), \tag{7.38}$$

$$A^{ref} = -\frac{\partial \psi_R^{mech}}{\partial p^{ref}} + H^{ref}(1 - p^{ref})$$

$$= -\Gamma n_{c_0} K_B N \left[ \sqrt{N^{-1}} \Lambda \zeta + \ln \left( \frac{\zeta}{\sinh(\zeta)} \right) \right] + H^{ref}(1 - p^{ref}). \tag{7.39}$$

## 7.5.1: Finite element implementation

In the case of stress-coupled oxidation, the balance of momentum's partial differential equation is coupled with the balance of oxygen concentration equation. There are two governing differential equations required to be solved in this case:

$$DivT + b = 0, (7.40)$$

$$\dot{C}_R^{o_2} = Div(D\nabla \cdot C_R^{o_2}) - r_{ox}^{sci} + r_{ox}^{ref}. \tag{7.41}$$

With b a non-inertial body force and Cauchy stress T. For solving the set of coupled equations, we need boundaries and initial conditions to complete the theory. For the local force balance, a pair of boundary conditions are considered, in which the displacement u and the surface traction tensor are specified on sub-surfaces of the boundary  $\partial B$  of the body B in a sense  $\partial B = s_u \cup s_t$  and  $s_u \cap s_t = \emptyset$ . Similarly, a pair of boundary conditions are considered for the oxygen concentration equation, such that oxygen concentration and oxygen flux are known on the sub-surfaces of the boundary. The initial condition data is taken as follows:

$$U(X,0) = U_0(X),$$
  $C_R^{o_2}(X,0) = C_R^{o_2}(X).$  (7.42)

Thus, the coupled set of Eqn.7.41, together with the boundary and initial condition, pose an initial boundary value problem to be solved for the displacement u(X, t) and oxygen concentration  $C^{o_2}$  simultaneously. The finite element method is used for solving the coupled set of equations, in which displacement and oxygen concentration are approximated in each element by:

$$u = \sum u^A N^A, \tag{7.43}$$

$$C_R^{o_2} = \sum (\mathbf{C}_R^{o_2})^A N^A,$$
 (7.44)

with the index  $A=1,2,3,\cdots,M$  denoting the nodes of the element, u, and  $C_R^{o_2}$  denoting nodal displacements, and oxygen concentration, and  $N^A$  the shape functions. We employ a standard Galerkin approach. In the absence of body forces, the corresponding weak forms of the coupled equation are:

$$\int_{B} T \cdot \frac{\partial N^{A}}{\partial x} dv = \int_{\partial B} N^{A} \cdot (T \cdot n) dA, \tag{7.45}$$

$$\int_{B} \dot{\mathbf{C}}_{R}^{o_{2}}.N^{A}.dv = -\int_{B} Div(D.\nabla.C_{R}^{o_{2}}).\frac{\partial N^{A}}{\partial x}.dv + \int_{\partial B} N^{A}.(D.\nabla.\mathbf{C}_{R}^{o_{2}}).n.dv 
-\int_{B} N^{A}.r_{ox,sci}.dv + \int_{B} N^{A}.r_{ox,ref}.dv.$$
(7.46)

This system of coupled equations is solved using a Newton procedure by defining the following element-level residuals for the displacement and oxygen concentration,

$$R_u = -\int_B T \cdot \frac{\partial N^A}{\partial x} dv + \int_{\partial B} N^A \cdot (T \cdot n) dA, \tag{7.47}$$

$$R_{c} = -\int_{B} \dot{C}_{R}^{o_{2}} . N^{A} . dv - \int_{B} Div(D.\nabla.C_{R}^{o_{2}}) . \frac{\partial N^{A}}{\partial x} . dv + \int_{\partial B} N^{A} . (D.\nabla.C_{R}^{o_{2}}) . n. dv - \int_{B} N^{A} . r_{ox,sci} . dv + \int_{B} N^{A} . r_{ox,ref} . dv.$$
(7.48)

In addition to the residuals, the following tangents are also required for the iterative Newton solver:

$$(K_{uu})^{AB} = -\frac{\partial (R_u)^A}{\partial u^B},\tag{7.49}$$

$$(K_{uc})^{AB} = -\frac{\partial (R_u)^A}{\partial c^B},\tag{7.50}$$

$$(K_{cu})^{AB} = -\frac{\partial (R_c)^A}{\partial u^B},\tag{7.51}$$

$$(K_{cc})^{AB} = -\frac{\partial (R_c)^A}{\partial c^B}. (7.52)$$

The residuals and elemental level stiffness matrix integrals are evaluated numerically using Gaussian quadrature. Since this is a standard method in the finite element literature, we do not present details here. In this work, the set of equations is solved numerically for each element by writing a user-element subroutine in FORTRAN language programming. In its notation, ABAQUS / standard (2020) requires certain matrices denoted as RHS and AMATRX to be evaluated and/or updated by the user element subroutine UEL. The work presented by Chester et.al [21] is referred to for more details on the solution method.

## 7.6: Concluding remark

The work presented aims at providing a comprehensive view of the heterogeneous oxidation of elastomers. Knowledge about oxygen uptake and penetration is essential to understand the mechanical property changes of the elastomer during aging. Heterogeneous oxidation is the simultaneous process of oxygen uptake and diffusion into elastomers. The introduced equations have described the absorption of oxygen phenomena. The results of the modified model are in good agreement with the experimentally reported data. Oxygen absorption has been considered as a function of the aging temperature, the progress of aging, and the surface-volume ratio. The diffusion-reaction equation has been extended in 3 dimensions to simulate the oxidation of complex-shaped elastomer components. The ADI numerical solution is utilized for the sake of illustration of heterogeneous oxidation over the thickness of the material. For better correlation with experimental data of the degree of oxidation, some reaction rate functions have been proposed for chain scission and net-

work reformation reactions. The capability of functions for predicting the extent of reactions in elastomers has been investigated by comparing the results with experimental data. In addition, this article presents a modified constitutive model for chemo-mechanically coupled large deformation of polymers. The model incorporates the coupled effect of the diffusion chemical reactions and mechanical loading of the continuum-level constitutive response of the material. The model's capability has been analyzed by implementing it into the Abaqus finite element software using the user element subroutine. The model can predict the oxidation rates in polymers under DLO and general stress-coupled oxidation scenarios.

# **CHAPTER 8: GRAPHIC USER**

# **INTERFACE**

### 8.1: Introduction

The integration of graphical user interfaces (GUIs) into finite element workflows significantly enhances user accessibility and efficiency, particularly for complex simulations. Abaqus, a powerful finite element analysis (FEA) software, provides a Python scripting interface that enables advanced customization and automation. Tkinter, the standard GUI library for Python, can be seamlessly used within the Abaqus environment to create intuitive interfaces for tasks such as model input, material parameter fitting, and postprocessing. This section outlines the core knowledge, procedural steps, and best practices for integrating Tkinter-based GUIs into Abaqus.

This chapter describes the rationale, design, architecture and implementation of the GUI, with a focus on how it integrates with the existing software ecosystem to enhance usability and functionality.

## 8.2: Motivation and Role of the GUI

#### 8.2.1: Limitations of the Commercial Software

While the commercial software provides robust simulation capabilities (e.g., thermomechanical solvers, structural analysis, transient simulations), it lacks support for:

- Advanced data preprocessing or augmentation workflows
- Customized model reduction techniques or post-processing routines
- User-developed features tailored to novel use cases or academic research
- Automation and integration across multiple simulation steps

### 8.2.2: Importance of Using a GUI in FEM Simulation

- **User-Friendly Interaction** A graphical user interface (GUI) provides an intuitive way for users, especially those who are not programming experts, to input complex model parameters, select materials, define boundary conditions, and configure simulation settings without writing code.
- Error reduction GUIs can incorporate input validation, drop-down menus, and predefined templates to reduce user errors in setting up simulations, leading to more reliable and consistent results
- Visual feedback and real-time updates With a GUI, users can visualize geometry, mesh quality, boundary conditions, and intermediate results interactively. This immediate feedback helps in detecting and correcting setup issues early.
- **Streamlined Workflow** GUIs integrate multiple steps of the simulation process, pre-processing, solving, and post-processing, in a single environment, improving productivity and reducing the learning curve.
- Accessibility and Collaboration By abstracting technical complexities, GUIs enable multidisciplinary teams (engineers, designers, analysts) to work collaboratively, sharing simulation setups and results easily.
- Customization and Automation Modern FEM GUIs often allow scripting or batch processing within a user-friendly interface, balancing ease of use with advanced control and automation.
- Improved Decision Making With interactive plots, graphs, and visualization embedded in GUIs, users can better interpret simulation outputs and make informed design or analysis decisions.

### 8.2.3: Purpose of the Custom GUI

The custom-developed GUI serves the following purposes:

• Improved Accessibility Graphical User Interfaces (GUIs) eliminate the need for users to

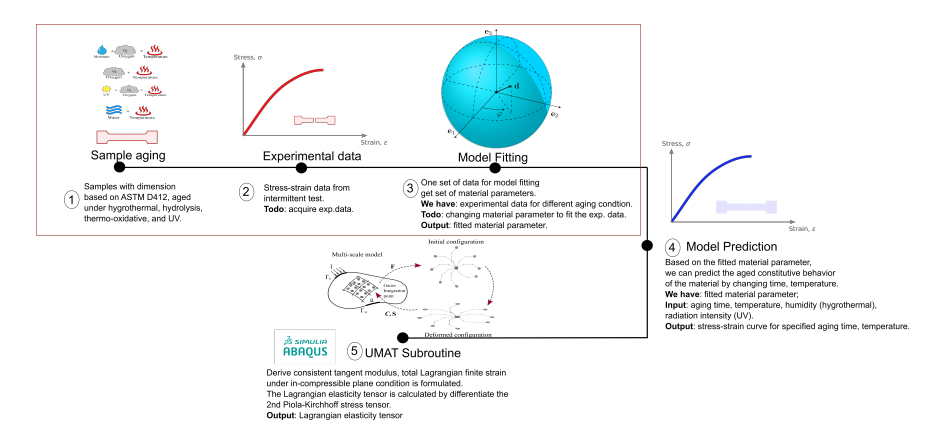


Figure 8.1: Overview of the UMAT Workflow.

interact with complex command line instructions or script syntax. This makes it easier for non-programmers to run simulations using intuitive inputs such as forms, drop-down menus, and buttons, rather than modifying code manually.

- Enhanced Workflow Efficiency GUIs simplify multistep or repetitive tasks by integrating them into single-button operations. This not only speeds up workflow, but also promotes consistency and reduces the likelihood of user error, especially valuable in industrial or teambased environments.
- Improved User ExperienceBy offering visual cues, progress indicators, and clear error messages, GUIs create a more engaging and user-friendly environment. This structured feedback is especially helpful during lengthy or computation-heavy simulations, minimizing confusion and frustration.

### 8.3: UMAT Derivation

#### 8.3.1: UMAT Subroutine Workflow

This section illustrates the workflow for running a UMAT subroutine in Abaqus without utilizing the dedicated graphical user interface (GUI), emphasizing the potential for errors and the complexity often faced by first-time users. The complete process, from initial setup to execution, is depicted in Fig.8.1. Procedures of how to run an Abaqus subroutine without using the GUI is listed in the following:

- 1. **Step 1**: Adjust the variables in .for file (Fortran code)(see Fig.8.2);
- 2. **Step 2**: Open Abaqus and Select *Job* in *Module* list (see Fig.8.3);
- 3. **Step 3**: Choose *Input File* from *Source* drop-down list (see Fig.8.4);
- 4. **Step 4**: Select *Input* file (see Fig.8.5);
- 5. **Step 5**: In *job editor*, use *General*, upload .for file under *User Subroutine file*, select .*ODB* in Result format (see Fig.8.6).

Figure 8.2: Variables in .for file.



Figure 8.3: Select **Job** in Module list.

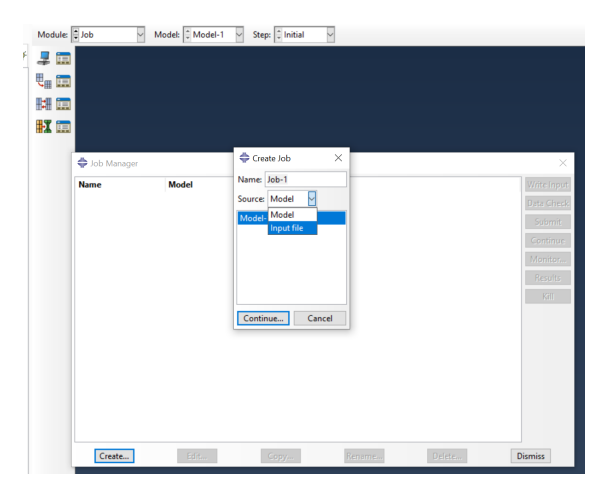


Figure 8.4: Choose **Input file** from **Source** drop-down list.

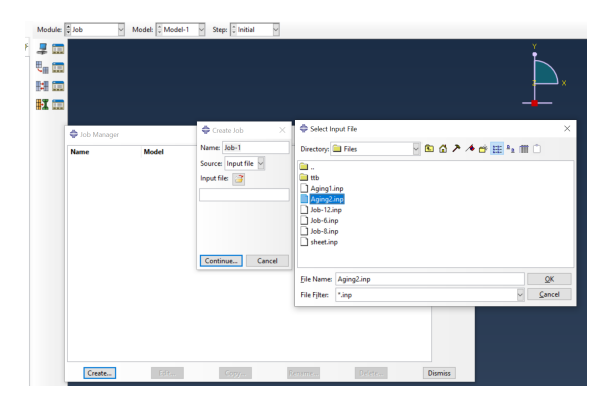


Figure 8.5: Select Input file.

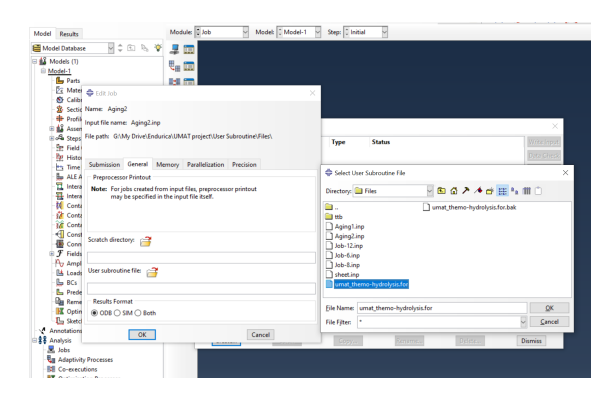


Figure 8.6: In **job editor**, use **General**, upload .for file under **User subroutine file**, select **ODB** in **Result format**.

# 8.4: Objective of Integration

- Provide a custom user interface for input setup, including geometry, boundary conditions, and material data.
- Automate the generation of input files (.inp) for Abaqus simulations.
- Incorporate custom pre-/post-processing routines (e.g., ML-driven preprocessing).
- To trigger and monitor Abaqus simulations from a single interface.
- To parse and visualize output (ODB) results post-simulation.

## 8.5: Background

The Abaqus Scripting Interface is a powerful tool that enables users to programmatically interact with the model database ( mdb ), simulation jobs and result files. However, it traditionally requires knowledge of Python scripting and familiarity with the Abaqus data structures, which may not always be accessible to all users.

Tkinter, being a lightweight and widely available GUI package, can be embedded within Abaqus Python scripts. This combination allows users to interact with Abaqus through buttons, text inputs, and file selectors, thereby reducing the need for direct coding interaction.

## 8.6: Methodology

The methodology involves embedding a Tkinter-based GUI within a Python script that utilizes the Abaqus Scripting Interface. The general flow of the integration process is as follows:

**Tkinter GUI Initialization**: A simple Tkinter window is created with user input fields and buttons.

- 1. **User Input Collection**: Users provide the necessary simulation parameters through the GUI, such as material properties, boundary conditions, or job settings.
- 2. **Simulation Setup via Abaqus Scripting**: Upon user interaction (e.g. clicking a button), the script reads the input values and uses the Abaqus Scripting Interface to generate the model,

- apply loads, mesh, and prepare the job.
- 3. Execution and Feedback: The script either submits the job automatically or allows the user to manually trigger the execution. Feedback or status messages can be displayed within the GUI or console.

## 8.7: Running the GUI Script in Abaqus

To streamline the simulation workflow within the Abaqus environment, a custom GUI was developed using Python's tkinter library. This user interface offers a visual alternative to command-line job submission, improving accessibility for users without scripting experience. The GUI integrates model management, job configuration, and boundary condition setup, all from a centralized interface.

The derived user interface (see Fig.8.7) allows users to specify or browse for an input file (.inp), assign a job name, and choose or create a working model. The model selection dropdown dynamically lists all available models in the current Abaqus database, while the optional model creation entry enables the user to define a new model interactively.

In addition to job submission, the GUI supports the creation of basic static steps and the application of default boundary conditions. Users can enable these features by filling in the **Step Name** field or toggling the "**Add default boundary condition**" checkbox. This boundary condition is applied to a default region named ALL, if it exists within the model's part definitions.

Upon submitting a job, the GUI invokes the Abaqus mdb. Job() constructor, linking the provided input file to the selected or newly created model. The job is then submitted and monitored through Abaqus' internal job manager. Completion status and any issues are reported via message boxes and console logging, allowing users to verify successful execution directly from the GUI.

This extensible tool not only enhances productivity but also serves as a customizable framework for automating simulation setup and execution workflows. With minor extensions, it can be adapted to include additional step types, material definitions, and load conditions - all accessible through a GUI framework consistent with Abaqus' internal data structures. The modular structure of the

code also allows for easy extension and customization based on project needs. The script can be executed within Abaqus by running:

```
abaqus cae script=abaqus_gui.py
```

The full source code is presented in the Appendix, and the layout of the GUI is visualized in the accompanying figure.

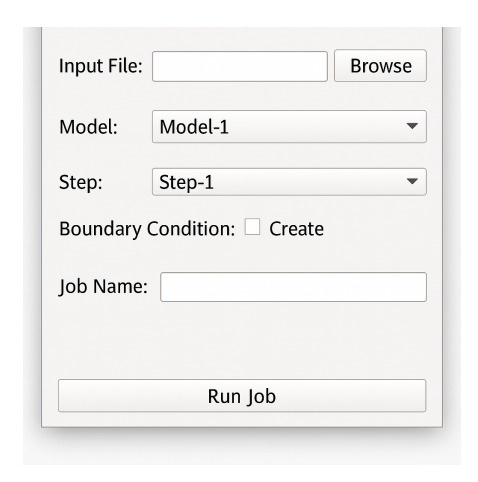


Figure 8.7: Tkinter-based GUI for Abaqus Job Submission.

Fig.8.7 shows the extended version of the Abaqus job submission GUI, which incorporates interactive elements for model-driven simulations. This graphic user interface introduces three major enhancements:

- Model Creation: Users can specify a new model name to be created on the fly. If the name
  does not exist in the current session, a new model object will be added to the Abaqus model
  database (mdb.models).
- **Step Definition:** A dedicated field allows users to enter a static step name, which will be added to the selected model. This enables users to configure basic analysis sequences directly from the GUI, avoiding manual scripting.
- **Boundary Condition Control:** An optional checkbox allows users to automatically assign a fixed displacement boundary condition to a predefined set named ALL. This is useful for running basic simulations without further pre-processing in the CAE interface.

The GUI reflects a modular design where each input field corresponds to a standard Abaqus scripting operation. Once all fields are populated and the user clicks Run Job, the script processes the inputs in sequence: it verifies file paths, creates or selects the model, defines the step and boundary condition (if applicable), then submits and monitors the job. The GUI provides immediate feedback via pop-up message boxes and printed console messages.

This tool is particularly valuable for iterative simulation tasks or instructional environments, where students or engineers can perform simulation runs without needing to understand the underlying scripting syntax. It can also be expanded to support material assignments, meshing operations, or post-processing routines in future iterations.

## 8.8: Implementation Workflow:

Integrating Tkinter with Abaqus Scripting To successfully implement a graphical user interface (GUI) using Tkinter within the Abaqus environment, a structured process must be followed. This section outlines the detailed workflow for integrating Tkinter into Abaqus scripts and describes how to run and use the resulting GUI.

#### 8.8.1: Workflow Overview

The overall workflow for creating and executing a Tkinter-Abaqus integrated application consists of the following steps:

Step	Description					
1	Design the GUI layout using Tkinter widgets (e.g., labels, entry fields,					
	buttons) to capture input parameters such as material properties, geom					
	etry specifications, and analysis settings.					
2	Define callback functions that are triggered by GUI interactions (e.g					
	clicking a "Run" or "Submit" button). These functions will gather inputs					
	from the GUI and use them to execute Abaqus commands.					
3	Import Abaqus scripting modules (from abaqus import *, from					
	abaqusConstants import *) to enable programmatic control of m					
	els, parts, materials, and jobs.					
4	Within the callback functions, use the Abaqus scripting interface to:					
	Create or access an existing model (mdb.Model).					
	<ul> <li>Define geometry, material, and section properties.</li> </ul>					
	<ul> <li>Assign boundary conditions, loads, and mesh controls.</li> </ul>					
	<ul> <li>Generate input files and submit analysis jobs.</li> </ul>					
5	\ \ \ \ \ \ \ \ \ \ \ \ \ \ \ \ \ \ \ \					
	boxes, progress bars) to guide and inform users during model setup and					
6	simulation execution.					
0	Save the script (e.g., GUI_name.py). Test it inside Abaqus by:  • Running it through Abaqus/CAE: File > Run Script.					
	• Or from the terminal (batch mode): abaqus cae					
	noGUI=GUI_name.py.					
	nodor-dor_name.py.					
7	Validate the script by ensuring the GUI inputs correctly translate into					
	Abaqus model features, the job submission runs without error, and the					
	output database (.odb) can be postprocessed as needed.					
8	Optionally extend the GUI to include:					
	File dialog access for user-defined data or geometry files.					
	• Postprocessing routines (e.g., read ODB results via					
	session.openOdb).					
	• Export options for simulation results (e.g., CSV, plots).					

Table 8.1: Workflow for Integrating Tkinter with Abaqus Scripting.

## 8.8.2: Detailed Steps

## **Step 1:** Designing the GUI Layout

• Use Tkinter classes such as Tk(), Label, Entry, Button, and Frame to construct the graphical layout.

• Arrange the widgets logically using .pack(), .grid(), or .place() layout managers.

```
root = tk.Tk()
tk.Label(root, text="Enter Young's Modulus:").pack()
entry_E = tk.Entry(root)
entry_E.pack()
```

#### **Step 2:** Defining Callback Functions

- Define Python functions that will be triggered by user actions (e.g., clicking a button).
- These functions should extract user input from the GUI and use it to drive the generation or manipulation of Abaqus models.

#### **Step 3:** Embedding Abaqus Commands

- Abaqus scripting commands such as mdb.Model, mdb.Job, or session.openOdb can be embedded directly inside the callback functions.
- This allows user inputs from the GUI to dynamically control the simulation parameters.

#### **Step 4:** Initializing and Running the Tkinter Main Loop

- After defining the GUI elements and callback functions, the Tkinter event loop must be started by calling root.mainloop().
- This command will keep the window open and responsive to user inputs.

```
root.mainloop()
```

#### **Step 5:** Executing the Script Inside Abaqus

- The script must be run inside the Abaqus Python interpreter to have access to both Tkinter and Abaqus modules (abaqus, abaqusConstants, etc.).
- There are two common ways to run the script:
  - 1. Inside Abaqus/CAE:
    - Open Abaqus/CAE.
    - Go to File → Run Script, then select and execute the Python file.

#### 2. From the Command Line:

- Use the following command to run the script in no-GUI (batch) mode:

abaqus cae noGUI=GUI name.py

3. **Note:** If complex GUI interactions are required, running within Abaqus/CAE is generally preferred.

### 8.8.3: Visual Summary of the Workflow

The flowchart (Fig. 8.8) illustrates the step-by-step process of integrating a Tkinter-based graphical user interface (GUI) with Abaqus scripting functionalities. Each stage of the workflow plays a crucial role in enabling user-friendly model creation and job submission within Abaqus. The process is as follows.

- 1. Design GUI Layout The first step involves creating the user interface using Tkinter widgets such as labels, entry fields, buttons, and frames. This layout defines how users will input parameters, interact with the script, and visualize the outputs.
- Define Callback Functions Next, callback functions are programmed to respond to user interactions (e.g., button clicks). These functions act as bridges between the GUI and the Abaqus Python scripting environment.
- 3. Abaqus commands embedded within the callback functions are inserted in Abaqus scripting commands (such as part creation, material definition, meshing, and job submission). This ensures that GUI actions directly trigger model-building and analysis operations in Abaqus.
- 4. Run Tkinter Main Loop After setting up the GUI and functions, the Tkinter Main Event Loop (mainloop()) is executed. This keeps the GUI active, allowing users to interact with it dynamically.
- 5. Execute Script Inside Abaqus Finally, the entire Python script is run inside the Abaqus/CAE or Abaqus/Viewer environment. This ensures that all necessary Abaqus modules and libraries are properly loaded and that the GUI can control Abaqus operations seamlessly.

This structured approach enables users to build custom, accessible interfaces for complex simulation workflows, thereby improving efficiency and reducing the likelihood of user errors.



Figure 8.8: Flowchart of Designing Process.

## 8.9: Designed User Interface

This section presents the designed GUI and its core functionalities. The primary purpose of the GUI is to streamline operations by bypassing predefined, lengthy subroutines that are prone to user error.

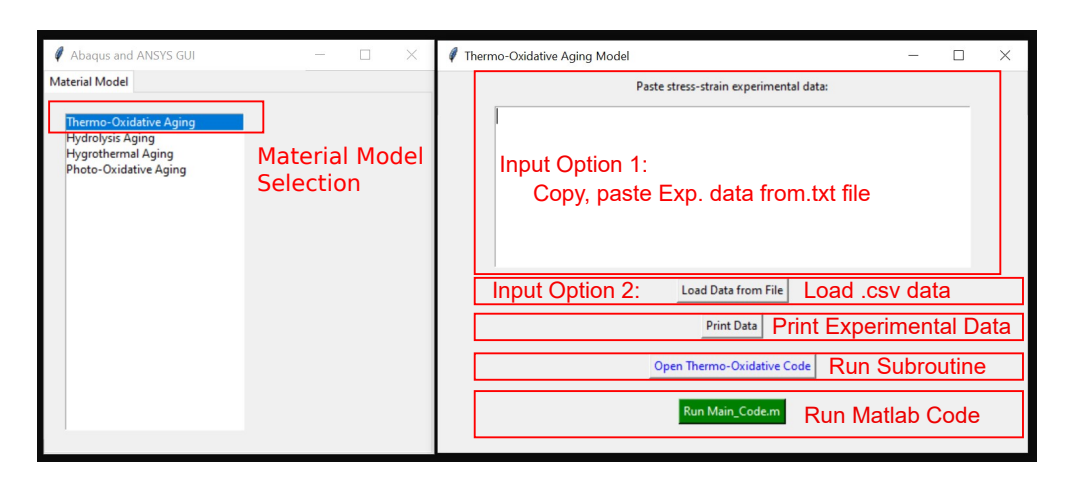


Figure 8.9: Graphical User Interface (GUI) Layout.

In addition to Fig.8.9, a simplified version (shown in Fig.8.10) is also developed. This simplified interface is designed specifically for executing user subroutines, without requiring manual selection or interaction with the full simulation setup. This version bypasses the UMAT selection step described in the previous section, enabling quicker deployment and testing of subroutine behavior in a controlled environment. The original selection interface is intended to provide detailed explanations of each environmental aging concept along with references to the corresponding original research papers.

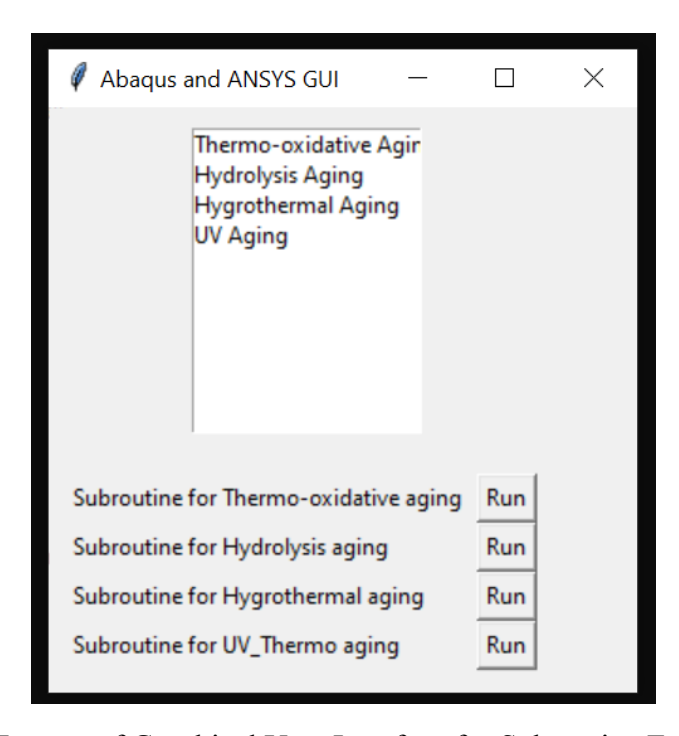


Figure 8.10: Layout of Graphical User Interface for Subroutine Execution Only.

Fig.8.11 shows the interface for selecting a sample material model. It is a click-based selection tool that navigates the user to the interface on the right-hand side. Once the user inputs the experimental stress-strain data into the designated fields and clicks the Material Model button, the tool automatically runs a Genetic Algorithm to identify the best-fit material parameters. These parameters can then be used for further correction or subsequent calculations.

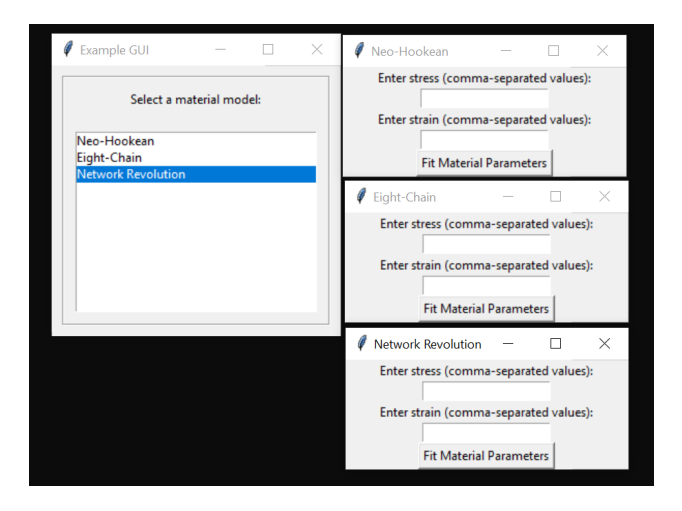


Figure 8.11: Material Model Selection Tool and Parameter Fitting Interface.

The implemented GUI provides two user-friendly methods for inputting stress-strain data: direct copy-paste from a .txt file or loading from a .csv file. As shown in Fig. 8.9, users can paste space-separated stress-strain pairs into a multi-line text box or click the *Load CSV File* button to import a file with two columns—stress and strain. In both cases, clicking the *Plot Data* button parses the input and generates a stress-strain plot, enabling quick visual validation before proceeding to model fitting or optimization. The code is provided in Appendix.

Fig. 8.12 illustrates the interface design options. The first option is a simple selection button, while the second is a drop-down menu that provides a list of predefined choices.

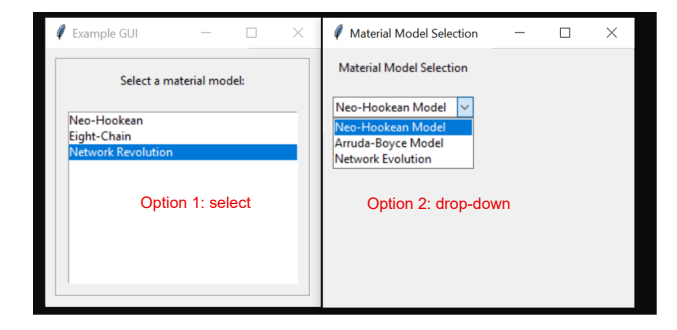


Figure 8.12: Selection options available in the Genetic Algorithm user interface.

The Graphic User Interface (GUI) of the Genetic Algorithm (GA) is illustrated in Fig.8.13. The purpose of this function is to simplify the process of determining the parameters of the best-fit material model. Instead of manually entering the material model code and its parameter range, users only need to enter the experimental stress and strain data. Once the data are provided, users can simply click the "Run Genetic Algorithm" button to obtain the optimized parameters that best fit the provided experimental results.

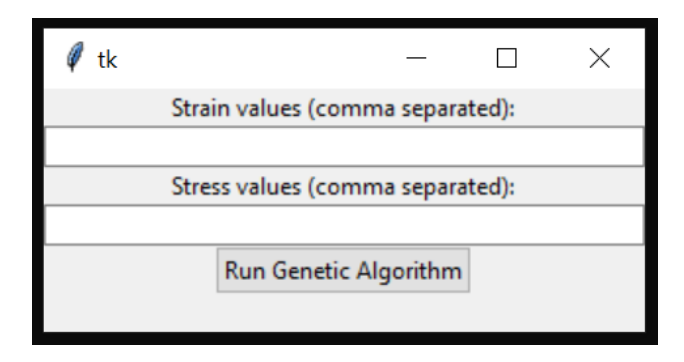


Figure 8.13: Genetic Algorithm User Interface.

# 8.10: Conclusion

Integrating Tkinter-based GUIs with Abaqus scripting offers an accessible and efficient solution for automating simulation setup, reducing the learning curve for users less familiar with scripting. This approach facilitates the development of intuitive interfaces for defining materials, configuring models, submitting jobs, and managing results—thereby streamlining the overall workflow in computational simulations. All Tkinter code implementations referenced in the previous sections are provided in the Appendix.

#### **BIBLIOGRAPHY**

- [1] S Abouzahr, GL Wilkes, and Z Ophir. Structure-property behaviour of segmented polyether-mdi-butanediol based urethanes: effect of composition ratio. *Polymer*, 23(7):1077–1086, 1982.
- [2] Nicoli M Ames, Vikas Srivastava, Shawn A Chester, and Lallit Anand. A thermomechanically coupled theory for large deformations of amorphous polymers. part ii: Applications. *International Journal of Plasticity*, 25(8):1495–1539, 2009.
- [3] L Anand and C Su. A theory for amorphous viscoplastic materials undergoing finite deformations, with application to metallic glasses. *Journal of the Mechanics and Physics of Solids*, 53(6):1362–1396, 2005.
- [4] Lallit Anand, Nicoli M Ames, Vikas Srivastava, and Shawn A Chester. A thermomechanically coupled theory for large deformations of amorphous polymers. part i: Formulation. *International Journal of Plasticity*, 25(8):1474–1494, 2009.
- [5] Ellen M Arruda and Mary C Boyce. A three-dimensional constitutive model for the large stretch behavior of rubber elastic materials. *Journal of the Mechanics and Physics of Solids*, 41(2):389–412, 1993.
- [6] Roger A Assink, Mathew Celina, Julie M Skutnik, and Douglas J Harris. Use of a respirometer to measure oxidation rates of polymeric materials at ambient temperatures. *Polymer*, 46(25):11648–11654, 2005.
- [7] L Audouin, V Gueguen, A Tcharkhtchi, and J Verdu. "close loop" mechanistic schemes for hydrocarbon polymer oxidation. *Journal of Polymer Science Part A: Polymer Chemistry*, 33(6):921–927, 1995.
- [8] Ludmila Audouin, Laurence Achimsky, and Jacques Verdu. Kinetic modeling of low-temperature oxidation of hydrocarbon polymers. In *Handbook of polymer degradation*, pages 753–764. CRC Press, 2000.
- [9] Amir Bahrololoumi, Aref Ghaderi, Mamoon Shaafaey, and Roozbeh Dargazany. A micromechanical constitutive model to predict hygrothermal aging of cross-linked polymers. In *ASME International Mechanical Engineering Congress and Exposition*, volume 85680, page V012T12A039. American Society of Mechanical Engineers, 2021.
- [10] Amir Bahrololoumi, Vahid Morovati, Emad A Poshtan, and Roozbeh Dargazany. A multiphysics constitutive model to predict quasi-static behaviour: Hydrolytic aging in thin cross-linked polymers. *International Journal of Plasticity*, page 102676, 2020.

- [11] Kenneth J Bowles and Gregory Nowak. Thermo-oxidative stability studies of celion 6000/pmr-15 unidirectional composites, pmr-15, and celion 6000 fiber. *Journal of Composite Materials*, 22(10):966–985, 1988.
- [12] P Budrugeac. Accelerated thermal ageing of nitrile-butadiene rubber under air pressure. *Polymer Degradation and stability*, 47(1):129–132, 1995.
- [13] F Bueche. Molecular basis for the mullins effect. *Journal of Applied Polymer Science*, 4(10):107–114, 1960.
- [14] M Celina, J Wise, DK Ottesen, KT Gillen, and RL Clough. Oxidation profiles of thermally aged nitrile rubber. *Polymer degradation and stability*, 60(2-3):493–504, 1998.
- [15] M Celina, J Wise, DK Ottesen, KT Gillen, and RL Clough. Correlation of chemical and mechanical property changes during oxidative degradation of neoprene. *Polymer degradation and Stability*, 68(2):171–184, 2000.
- [16] Mathew C Celina. Review of polymer oxidation and its relationship with materials performance and lifetime prediction. *Polymer Degradation and Stability*, 98(12):2419–2429, 2013.
- [17] J Chen, W Wang, and J Li. Effect of thermal vacuum environment on the performance of adhesive bonding materials, aerosp. *Mater. Technol*, 42(6):92–96, 2012.
- [18] Jun Chen, Nengwen Ding, Zhifeng Li, and Wei Wang. Organic polymer materials in the space environment. *Progress in Aerospace Sciences*, 83:37–56, 2016.
- [19] Shawn A Chester and Lallit Anand. A coupled theory of fluid permeation and large deformations for elastomeric materials. *Journal of the Mechanics and Physics of Solids*, 58(11):1879–1906, 2010.
- [20] Shawn A Chester and Lallit Anand. A thermo-mechanically coupled theory for fluid permeation in elastomeric materials: application to thermally responsive gels. *Journal of the Mechanics and Physics of Solids*, 59(10):1978–2006, 2011.
- [21] Shawn A Chester, Claudio V Di Leo, and Lallit Anand. A finite element implementation of a coupled diffusion-deformation theory for elastomeric gels. *International Journal of Solids and Structures*, 52:1–18, 2015.
- [22] Sung-Seen Choi and Jong-Chul Kim. Lifetime prediction and thermal aging behaviors of sbr and nbr composites using crosslink density changes. *Journal of Industrial and Engineering Chemistry*, 18(3):1166–1170, 2012.
- [23] Hsoung-Wei Chou, Jong-Shin Huang, and Shih-Ting Lin. Effects of thermal aging on fatigue

- of carbon black–reinforced epdm rubber. *Journal of applied polymer science*, 103(2):1244–1251, 2007.
- [24] X Colin, L Audouin, and J Verdu. Kinetic modelling of the thermal oxidation of polyisoprene elastomers. part 3: Oxidation induced changes of elastic properties. *Polymer degradation and stability*, 92(5):906–914, 2007.
- [25] X Colin, C Marais, and J Verdu. A new method for predicting the thermal oxidation of thermoset matrices: application to an amine crosslinked epoxy. *Polymer Testing*, 20(7):795–803, 2001.
- [26] X Colin and J Verdu. Thermal ageing and lifetime prediction for organic matrix composites. *Plastics, rubber and composites*, 32(8-9):349–356, 2003.
- [27] X Colin and J Verdu. Strategy for studying thermal oxidation of organic matrix composites. *Composites Science and technology*, 65(3-4):411–419, 2005.
- [28] Xavier Colin and Jacques Verdu. Mechanisms and kinetics of organic matrix thermal oxidation. In *Long-term durability of polymeric matrix composites*, pages 311–344. Springer, 2011.
- [29] AV Cunliffe and A Davis. Photo-oxidation of thick polymer samples—part ii: The influence of oxygen diffusion on the natural and artificial weathering of polyolefins. *Polymer Degradation and Stability*, 4(1):17–37, 1982.
- [30] Hüsnü Dal, Osman Gültekin, and Kemal Açıkgöz. An extended eight-chain model for hyperelastic and finite viscoelastic response of rubberlike materials: Theory, experiments and numerical aspects. *Journal of the Mechanics and Physics of Solids*, 145:104159, 2020.
- [31] Roozbeh Dargazany, Vu Ngoc Khiêm, Uwe Navrath, and Mikhail Itskov. Network evolution model of anisotropic stress softening in filled rubber-like materials: Parameter identification and finite element implementation. *Journal of Mechanics of Materials and Structures*, 7(8):861–885, 2013.
- [32] J Decelle, N Huet, and V Bellenger. Oxidation induced shrinkage for thermally aged epoxy networks. *Polymer Degradation and Stability*, 81(2):239–248, 2003.
- [33] Mohammad Dehghany, Haohui Zhang, Reza Naghdabadi, and Yuhang Hu. A thermodynamically-consistent large deformation theory coupling photochemical reaction and electrochemistry for light-responsive gels. *Journal of the Mechanics and Physics of Solids*, 116:239–266, 2018.
- [34] Julie Diani, Bruno Fayolle, and Pierre Gilormini. A review on the mullins effect. *European Polymer Journal*, 45(3):601–612, 2009.

- [35] Bradley K Diedrick. Effectsof prior aging at 260° c in argon on inelastic deformation behavior of pmr-15 polymer at 260° c: Experiment and modeling. 2010.
- [36] Jim Douglas. Alternating direction methods for three space variables. *Numerische Mathematik*, 4:41–63, 1962.
- [37] Fernando P Duda, Angela C Souza, and Eliot Fried. A theory for species migration in a finitely strained solid with application to polymer network swelling. *Journal of the Mechanics and Physics of Solids*, 58(4):515–529, 2010.
- [38] AE Ehret, M Itskov, and H Schmid. Numerical integration on the sphere and its effect on the material symmetry of constitutive equations—a comparative study. *International journal for numerical methods in engineering*, 81(2):189–206, 2010.
- [39] Esteve Ernault, Emmanuel Richaud, and Bruno Fayolle. Thermal-oxidation of epoxy/amine followed by glass transition temperature changes. *Polymer Degradation and Stability*, 138:82–90, 2017.
- [40] BCXALVJ Fayolle, X Colin, L Audouin, and J Verdu. Mechanism of degradation induced embrittlement in polyethylene. *Polymer degradation and stability*, 92(2):231–238, 2007.
- [41] Bruno Fayolle, Emmanuel Richaud, Jacques Verdu, and Fabienne Farcas. Embrittlement of polypropylene fibre during thermal oxidation. *Journal of materials science*, 43:1026–1032, 2008.
- [42] Paul J Flory. Principles of polymer chemistry. Cornell university press, 1953.
- [43] Mariacristina Gagliardi, Pietro Lenarda, and Marco Paggi. A reaction-diffusion formulation to simulate eva polymer degradation in environmental and accelerated ageing conditions. *Solar Energy Materials and Solar Cells*, 164:93–106, 2017.
- [44] Aref Ghaderi, Vahid Morovati, Amir Bahrololoumi, and Roozbeh Dargazany. A physics-informed neural network constitutive model for cross-linked polymers. In *ASME International Mechanical Engineering Congress and Exposition*, volume 84607, page V012T12A007. American Society of Mechanical Engineers, 2020.
- [45] Marco Gigliotti and Jean-Claude Grandidier. Chemo-mechanics couplings in polymer matrix materials exposed to thermo-oxidative environments. *Comptes Rendus Mécanique*, 338(3):164–175, 2010.
- [46] Marco Gigliotti, Jean-Claude Grandidier, and Marie Christine Lafarie-Frenot. Assessment of chemo-mechanical couplings in polymer matrix materials exposed to thermo-oxidative environments at high temperatures and under tensile loadings. *Mechanics of Materials*, 43(8):431–443, 2011.

- [47] Marco Gigliotti, Loic Olivier, Dinh Quy Vu, Jean-Claude Grandidier, and Marie Christine Lafarie-Frenot. Local shrinkage and stress induced by thermo-oxidation in composite materials at high temperatures. *Journal of the Mechanics and Physics of Solids*, 59(3):696–712, 2011.
- [48] Pieter Gijsman, Weifu Dong, Adam Quintana, and Mathew Celina. Influence of temperature and stabilization on oxygen diffusion limited oxidation profiles of polyamide 6. *Polymer Degradation and Stability*, 130:83–96, 2016.
- [49] Kenneth T Gillen, Mathias Celina, and Michael R Keenan. Methods for predicting more confident lifetimes of seals in air environments. *Rubber chemistry and technology*, 73(2):265–283, 2000.
- [50] Kenneth T Gillen and Roger L Clough. Rigorous experimental confirmation of a theoretical model for diffusion-limited oxidation. *Polymer*, 33(20):4358–4365, 1992.
- [51] Sanjay Govindjee and Juan C Simo. Coupled stress-diffusion: Case ii. *Journal of the Mechanics and Physics of Solids*, 41(5):863–887, 1993.
- [52] Morton E Gurtin, Eliot Fried, and Lallit Anand. *The mechanics and thermodynamics of continua*. Cambridge University Press, 2010.
- [53] David E Hanson, Marilyn Hawley, Robert Houlton, Kiran Chitanvis, Philip Rae, E Bruce Orler, and Debra A Wrobleski. Stress softening experiments in silica-filled polydimethylsiloxane provide insight into a mechanism for the mullins effect. *Polymer*, 46(24):10989–10995, 2005.
- [54] Leila Haroonabadi, Ali Dashti, and Mahsa Najipour. Investigation of the effect of thermal aging on rapid gas decompression (rgd) resistance of nitrile rubber. *Polymer Testing*, 67:37–45, 2018.
- [55] A Herzig, M Johlitz, and A Lion. Ageing experimental investigation on the consumption of oxygen and its diffusion into elastomers during the process of ageing. In *Constitutive Models for Rubber IX*, pages 39–44. CRC Press, 2015.
- [56] A Herzig, M Johlitz, and A Lion. Consumption and diffusion of oxygen during the thermoxidative ageing process of elastomers: Absorption und diffusion von sauerstoff während der thermooxidativen alterung von elastomeren. *Materialwissenschaft und Werkstofftechnik*, 47(5-6):376–387, 2016.
- [57] A Herzig, M Johlitz, RJ Pazur, I Lopez-Carreon, and CG Porter. Thermal ageing of peroxide-cured nbr, part ii: Diffusion-limited oxidation and constitutive modelling. In *Constitutive Models for Rubber XI*, pages 587–592. CRC Press, 2019.

- [58] A Herzig, L Sekerakova, M Johlitz, and A Lion. A modelling approach for the heterogeneous oxidation of elastomers. *Continuum Mechanics and Thermodynamics*, 29:1149–1161, 2017.
- [59] Alexander Herzig, Michael Johlitz, and Alexander Lion. An experimental set-up to analyse the oxygen consumption of elastomers during ageing by using a differential oxygen analyser. *Continuum Mechanics and Thermodynamics*, 27:1009–1017, 2015.
- [60] E Hoffman, W Daugherty, E Skidmore, K Dunn, and D Fisher. Aging performance of model 9975 package fluoroelastomer o-rings. Technical report, Savannah River Site (SRS), Aiken, SC (United States), 2011.
- [61] Kurt Hornik, Maxwell Stinchcombe, and Halbert White. Multilayer feedforward networks are universal approximators. *Neural networks*, 2(5):359–366, 1989.
- [62] Rubber Houwink. Slipping of molecules during the deformation of reinforced rubber. *Rubber Chemistry and Technology*, 29(3):888–893, 1956.
- [63] Yani Ioannou, Duncan Robertson, Darko Zikic, Peter Kontschieder, Jamie Shotton, Matthew Brown, and Antonio Criminisi. Decision forests, convolutional networks and the models inbetween. *arXiv preprint arXiv:1603.01250*, 2016.
- [64] Michael Johlitz. On the representation of ageing phenomena. *The Journal of Adhesion*, 88(7):620–648, 2012.
- [65] Michael Johlitz, Nico Diercks, and Alexander Lion. Thermo-oxidative ageing of elastomers: A modelling approach based on a finite strain theory. *International Journal of Plasticity*, 63:138–151, 2014.
- [66] Michael Johlitz and Alexander Lion. Chemo-thermomechanical ageing of elastomers based on multiphase continuum mechanics. *Continuum Mechanics and Thermodynamics*, 25:605–624, 2013.
- [67] S Kamarudin, PY Le Gac, Y Marco, and AH Muhr. Formation of crust on natural rubber after ageing. In *Proceedings of the 7th European Conference on Constitutive Models for Rubber, ECCMR*, pages 197–202, 2011.
- [68] Leif Kari. Dynamic stiffness of chemically and physically ageing rubber vibration isolators in the audible frequency range: Part 1: constitutive equations. *Continuum Mechanics and Thermodynamics*, 29(5):1027–1046, 2017.
- [69] Yoichi Kodera and Benjamin J McCoy. Distribution kinetics of radical mechanisms: reversible polymer decomposition. *AIChE journal*, 43(12):3205–3214, 1997.
- [70] Evgenia Kollia, Antonios Vavouliotis, and Vassilios Kostopoulos. Thermal ageing of carbon

- fiber-reinforced cyanate ester composites under inert and oxidative environment. *Polymer Composites*, 40(S2):E1388–E1396, 2019.
- [71] Shabnam Konica and Trisha Sain. A thermodynamically consistent chemo-mechanically coupled large deformation model for polymer oxidation. *Journal of the Mechanics and Physics of Solids*, 137:103858, 2020.
- [72] G Kraus, CW Childers, and KW Rollmann. Stress softening in carbon black-reinforced vulcanizates. strain rate and temperature effects. *Journal of Applied Polymer Science*, 10(2):229–244, 1966.
- [73] Shin-ichi Kuroda, Koichiro Terauchi, Kyohei Nogami, and Itaru Mita. Degradation of aromatic polymers—i. rates of crosslinking and chain scission during thermal degradation of several soluble aromatic polymers. *European polymer journal*, 25(1):1–7, 1989.
- [74] Julie Lambert-Diani and Christian Rey. New phenomenological behavior laws for rubbers and thermoplastic elastomers. *European Journal of Mechanics-A/Solids*, 18(6):1027–1043, 1999.
- [75] Pierre Yves Le Gac, Mathew Celina, Gérard Roux, Jacques Verdu, Peter Davies, and Bruno Fayolle. Predictive ageing of elastomers: Oxidation driven modulus changes for polychloroprene. *Polymer Degradation and Stability*, 130:348–355, 2016.
- [76] Pierre-Yves Le Gac, V Le Saux, M Paris, and Yann Marco. Ageing mechanism and mechanical degradation behaviour of polychloroprene rubber in a marine environment: Comparison of accelerated ageing and long term exposure. *Polymer degradation and stability*, 97(3):288–296, 2012.
- [77] Jichun Li and Yi-Tung Chen. *Computational partial differential equations using MATLAB*®. Crc Press, 2019.
- [78] A Lion and M Johlitz. On the representation of chemical ageing of rubber in continuum mechanics. *International Journal of Solids and Structures*, 49(10):1227–1240, 2012.
- [79] Kaspar Loeffel and Lallit Anand. A chemo-thermo-mechanically coupled theory for elastic–viscoplastic deformation, diffusion, and volumetric swelling due to a chemical reaction. *International Journal of Plasticity*, 27(9):1409–1431, 2011.
- [80] Thanh-Tam Mai, Yoshihiro Morishita, and Kenji Urayama. Novel features of the mullins effect in filled elastomers revealed by stretching measurements in various geometries. *Soft matter*, 13(10):1966–1977, 2017.
- [81] Gilles Marckmann, Erwan Verron, Laurent Gornet, Grégory Chagnon, Pierre Charrier, and Patrice Fort. A theory of network alteration for the mullins effect. *Journal of the Mechanics*

- and Physics of Solids, 50(9):2011–2028, 2002.
- [82] M Minervino, M Gigliotti, MC Lafarie-Frenot, and JC Grandidier. The effect of thermooxidation on the mechanical behaviour of polymer epoxy materials. *Polymer testing*, 32(6):1020–1028, 2013.
- [83] M Minervino, M Gigliotti, MC Lafarie-Frenot, and JC Grandidier. A coupled experimental/numerical approach for the modelling of the local mechanical behaviour of epoxy polymer materials. *Journal of the Mechanics and Physics of Solids*, 67:129–151, 2014.
- [84] A Mousa, US Ishiaku, and ZA Mohd Ishak. Thermo-oxidative aging and fatigue behavior of dynamically vulcanized pvc/enr thermoplastic elastomers. *International Journal of Polymeric Materials*, 51(11):967–980, 2002.
- [85] Leonard Mullins. Softening of rubber by deformation. *Rubber chemistry and technology*, 42(1):339–362, 1969.
- [86] Bruno Musil, Michael Johlitz, and Alexander Lion. On the ageing behaviour of nbr: chemomechanical experiments, modelling and simulation of tension set. *Continuum Mechanics and Thermodynamics*, pages 1–17, 2018.
- [87] Bruno Musil, Michael Johlitz, and Alexander Lion. On the ageing behaviour of nbr: chemomechanical experiments, modelling and simulation of tension set. *Continuum Mechanics and Thermodynamics*, 32:369–385, 2020.
- [88] Pellegrino Musto, Giuseppe Ragosta, Mario Abbate, and Gennaro Scarinzi. Photo-oxidation of high performance epoxy networks: correlation between the molecular mechanisms of degradation and the viscoelastic and mechanical response. *Macromolecules*, 41(15):5729–5743, 2008.
- [89] L Olivier, NQ Ho, JC Grandidier, and MC Lafarie-Frenot. Characterization by ultra-micro indentation of an oxidized epoxy polymer: correlation with the predictions of a kinetic model of oxidation. *Polymer Degradation and Stability*, 93(2):489–497, 2008.
- [90] Ozgur Ozmen. Effects of prior aging at 316 c in argon on inelastic deformation behavior of pmr-15 polymer at 316 c: Experiment and modeling. 2009.
- [91] Abhishek Panigrahi, Abhishek Shetty, and Navin Goyal. Effect of activation functions on the training of overparametrized neural nets. *arXiv* preprint arXiv:1908.05660, 2019.
- [92] Marina Pecora, Yannick Pannier, Marie-Christine Lafarie-Frenot, Marco Gigliotti, and Camille Guigon. Effect of thermo-oxidation on the failure properties of an epoxy resin. *Polymer Testing*, 52:209–217, 2016.

- [93] Vorapong Pimolsiriphol, Pongdhorn Saeoui, and Chakrit Sirisinha. Relationship among thermal ageing degradation, dynamic properties, cure systems, and antioxidants in natural rubber vulcanisates. *Polymer-Plastics Technology and Engineering*, 46(2):113–121, 2007.
- [94] Kishore V Pochiraju. Modeling thermo-oxidative aging and degradation of composites. In *Long-term durability of polymeric matrix composites*, pages 383–425. Springer, 2011.
- [95] KV Pochiraju, GP Tandon, and GA Schoeppner. Evolution of stress and deformations in high-temperature polymer matrix composites during thermo-oxidative aging. *Mechanics of Time-Dependent Materials*, 12:45–68, 2008.
- [96] Adam Quintana and Mathew C Celina. Overview of dlo modeling and approaches to predict heterogeneous oxidative polymer degradation. *Polymer Degradation and Stability*, 149:173–191, 2018.
- [97] N Rabanizada, F Lupberger, M Johlitz, and A Lion. Experimental investigation of the dynamic mechanical behaviour of chemically aged elastomers. *Archive of Applied Mechanics*, 85:1011–1023, 2015.
- [98] Sudip Ray and Ralph P Cooney. Thermal degradation of polymer and polymer composites. In *Handbook of environmental degradation of materials*, pages 185–206. Elsevier, 2018.
- [99] LM Rincon-Rubio, B Fayolle, L Audouin, and J Verdu. A general solution of the closed-loop kinetic scheme for the thermal oxidation of polypropylene. *Polymer Degradation and Stability*, 74(1):177–188, 2001.
- [100] Trisha Sain, Kaspar Loeffel, and Shawn Chester. A thermo-chemo-mechanically coupled constitutive model for curing of glassy polymers. *Journal of the Mechanics and Physics of Solids*, 116:267–289, 2018.
- [101] John Scheirs, Stephen W Bigger, and Norman C Billingham. A review of oxygen uptake techniques for measuring polyolefin oxidation. *Polymer testing*, 14(3):211–241, 1995.
- [102] Lars Steinke. Ein Beitrag zur Simulation der thermo-oxidativen Alterung von Elastomeren. VDI-Verlag, 2013.
- [103] GP Tandon, KV Pochiraju, and GA Schoeppner. Modeling of oxidative development in pmr-15 resin. *Polymer Degradation and Stability*, 91(8):1861–1869, 2006.
- [104] Abbas Tcharkhtchi, Sedigheh Farzaneh, Sofiane Abdallah-Elhirtsi, Bardia Esmaeillou, Fabien Nony, and A Baron. Thermal aging effect on mechanical properties of polyurethane. *International Journal of Polymer Analysis and Characterization*, 19(7):571–584, 2014.
- [105] Namrata Singh Tomer, Florence Delor-Jestin, RP Singh, and Jacques Lacoste. Cross-linking

- assessment after accelerated ageing of ethylene propylene diene monomer rubber. *Polymer Degradation and Stability*, 92(3):457–463, 2007.
- [106] Leslie Ronald George Treloar. *The physics of rubber elasticity*. Oxford University Press, USA, 1975.
- [107] GJ Van Amerongen. Influence of structure of elastomers on their permeability to gases. *Journal of polymer science*, 5(3):307–332, 1950.
- [108] Arnaud Vieyres, Roberto Pérez-Aparicio, Pierre-Antoine Albouy, Olivier Sanseau, Kay Saalwächter, Didier R Long, and Paul Sotta. Sulfur-cured natural rubber elastomer networks: correlating cross-link density, chain orientation, and mechanical response by combined techniques. *Macromolecules*, 46(3):889–899, 2013.
- [109] Haixiao Wan, Ke Gao, Sai Li, Liqun Zhang, Xiaohui Wu, Xiaodong Wang, and Jun Liu. Chemical bond scission and physical slippage in the mullins effect and fatigue behavior of elastomers. *Macromolecules*, 52(11):4209–4221, 2019.
- [110] Elias Wang, Atli Kosson, and Tong Mu. Deep action conditional neural network for frame prediction in atari games. Technical report, Technical Report, Stanford University, 2017.
- [111] J Wise, KT Gillen, and RL Clough. Quantitative model for the time development of diffusion-limited oxidation profiles. *Polymer*, 38(8):1929–1944, 1997.
- [112] Jiangtao Wu, Zeang Zhao, Craig M Hamel, Xiaoming Mu, Xiao Kuang, Zaoyang Guo, and H Jerry Qi. Evolution of material properties during free radical photopolymerization. *Journal of the Mechanics and Physics of Solids*, 112:25–49, 2018.
- [113] Chen Xuan and Lihua Jin. Concurrent reaction and diffusion in photo-responsive hydrogels. *Journal of the Mechanics and Physics of Solids*, 124:599–611, 2019.
- [114] YS Rohana Yahya, AR Azura, and Z Ahmad. Effect of curing systems on thermal degradation behaviour of natural rubber (smr cv 60). *Journal of Physical Science*, 22(2):1–14, 2011.
- [115] Yang. Paper-related code release, 2025. https://github.com/chyg-code/appendix/tree/main.
- [116] C Joshua Yeh, Matt Dowland, Randall G Schmidt, and Kenneth R Shull. Fracture and thermal aging of resin-filled silicone elastomers. *Journal of Polymer Science Part B: Polymer Physics*, 54(2):263–273, 2016.
- [117] Oon H Yeoh. Characterization of elastic properties of carbon-black-filled rubber vulcanizates. *Rubber chemistry and technology*, 63(5):792–805, 1990.

- [118] Oon H Yeoh and PD Fleming. A new attempt to reconcile the statistical and phenomenological theories of rubber elasticity. *Journal of Polymer Science Part B: Polymer Physics*, 35(12):1919–1931, 1997.
- [119] Maha Zaghdoudi, Anja Kömmling, Matthias Jaunich, and Dietmar Wolff. Scission, crosslinking, and physical relaxation during thermal degradation of elastomers. *Polymers*, 11(8):1280, 2019.
- [120] Danming Zhong, Yuhai Xiang, Tenghao Yin, Honghui Yu, Shaoxing Qu, and Wei Yang. A physically-based damage model for soft elastomeric materials with anisotropic mullins effect. *International Journal of Solids and Structures*, 176:121–134, 2019.

#### **APPENDIX**

All Graphic-User Interface source code has been uploaded and can be viewed at [115]. For integration point of micro-sphere approach, the integration points and weighting factors of the unit-sphere is shown in Table 8.2

i	$d_i(1)$	$d_i(2)$	$d_i(3)$	$w_i$
1	0.0	0.0	1.0	0.0265214244093
2	0.0	1.0	0.0	0.0265214244093
3	1.0	0.0	0.0	0.0265214244093
4	0.0	0.707106781187	0.707106781187	0.0199301476312
5	0.0	0.707106781187	0.707106781187	0.0199301476312
6	0.707106781187	0.0	0.707106781187	0.0199301476312
7	0.707106781187	0.0	0.707106781187	0.0199301476312
8	0.707106781187	0.707106781187	0.0	0.0199301476312
9	0.707106781187	0.707106781187	0.0	0.0199301476312
10	0.836095596749	0.387907304067	0.387907304067	0.0250712367487
11	0.836095596749	0.387907304067	0.387907304067	0.0250712367487
12	0.836095596749	0.387907304067	0.387907304067	0.0250712367487
13	0.836095596749	0.387907304067	0.387907304067	0.0250712367487
14	0.387907304067	0.836095596749	0.387907304067	0.0250712367487
15	0.387907304067	0.836095596749	0.387907304067	0.0250712367487
16	0.387907304067	0.836095596749	0.387907304067	0.0250712367487
17	0.387907304067	0.836095596749	0.387907304067	0.0250712367487
18	0.387907304067	0.387907304067	0.836095596749	0.0250712367487
19	0.387907304067	0.387907304067	0.836095596749	0.0250712367487
20	0.387907304067	0.387907304067	0.836095596749	0.0250712367487
21	0.387907304067	-0.387907304067	0.836095596749	0.0250712367487

Table 8.2: Integration points and weighting factors of the unit-sphere